Title: Organic Matter from the Chicxulub Crater Exacerbated the K-Pg Impact Winter

Author Line: Shelby L. Lyons*[1], Allison T. Karp[1], Timothy Bralower[1], Kliti Grice[2], Bettina Schaefer[2], Sean Gulick[3,4], Joanna Morgan[5], Katherine H. Freeman[1]

Author Affiliation:
[1]Department of Geosciences, The Pennsylvania State University, University Park, PA, USA 16802
[2]Western Australia Organic & Isotope Geochemistry Centre, School of Earth and Planetary Sciences, The Institute for Geoscience Research, Curtin University, Perth, WA, Australia
[3]Institute for Geophysics & Department of Geological Sciences, University of Texas at Austin, Austin, TX, USA
[4]Center for Planetary Systems Habitability, University of Texas at Austin, Austin, TX, USA
[5]Department of Earth Science & Engineering, Imperial College London, London, UK

Supplemental Information

1. Site Descriptions

Site M0077A Chicxulub Basin

Sediment and rock from the peak ring of the Chicxulub impact crater were recovered on IODP-ICDP Expedition 364 and divided into four sections (1). Material for this study was collected from the 111.63 m thick "Unit 1" which contains post impact sediments (2). Underlying Unit 1 is a 104.28 m section of suevite ("Unit 2"), below which is a 25.41 m section of melt rock with clasts ("Unit 3"), and a section of shocked granitic target rock ("Unit 4") (2). Unit 1, the sedimentary unit, is split into seven sections (1A – 1G), of which the two lowermost sections (1F & 1G) were of interest in this study, as they contain the first sedimentation of the Cenozoic. Transitional Unit 1G (Section 007 – 40R – 1, 34-108 cm / 616.58 - 617.33 mbsf) is identified as the K-Pg boundary layer and was deposited via seiche waves and settling. Unit 1G contains a thinly laminated, dark gray-brown micritic limestone from the base (Section 007 – 40R – 1, 67-108cm / 616.91 – 617.33 mbsf) with abundant charcoal in the lowermost section (Section 007 – 40R – 1, 103-108 cm / 617.28 – 617.33 mbsf), above which is a unit identified as a slumped interval or homogenized interval (Section 007 – 40R – 1, 54 – 67 cm / 616.78 – 616.91 mbsf) (2). Above the slumped interval is a relatively more homogenized micritic limestone (Section 007 – 40R – 1, 34-54 cm / 616.58 – 616.78 mbsf) that contains distinct trace fossils of *Planolites* and *Chondrites,* which provide evidence for the return of benthic life within the crater The deposition of the transitional unit occurred within months (2) of the impact.

Unit 1F, the first sedimentation of the Paleogene, lies above the transitional unit. Above the transitional unit is a green-gray claystone (Section 007 – 40R – 1, 29-34 cm / 616.53 – 616.58 mbsf) containing the Iridium spike, abundant charcoal, foraminifera, and increasing shell fragments (2–4) and a relative maxima in PAH concentrations. Charcoal in the claystone has been interpreted as either airfall or reworked, washed in, or bioturbated material from the lower charcoal unit (Section 007 –40R – 1, 103-108 cm / 617.28 – 617.33 mbsf) (2). Deposition of the green marl occurred between < 6 years and 30,000 years following the impact (5) (see Lowery *et al.*, 2018 and Gulick *et al.,* 2019 for further discussion of timing).

47
48 Overlying the green marl is a white pelagic carbonate, with less reworked material upsection (5).
49 Samples from the Danian carbonate were obtained between Section 007 – 40R – 1, 10 – 34 cm /
50 616.34 – 616.68 mbsf. For additional discussion of the deposition of the Transitional Unit and
51 the Danian pelagic carbonate, as well as what these units represent, see Gulick *et al.,* 2019,
52 Lowery *et al*., 2018, and Bralower *et al*., 2020 (**Supplemental Figure S1**).
53
54 <u>Site 738, Kerguelen Plateau</u>
55
56 Samples from the Indian Ocean Kerguelen Plateau Site 738 were obtained between 738C-20R-5
57 8 – 98 cm / 376.39 – 377.19 mbsf. Below 97.5 cm in section 738C-20R-5 (377.185 m) is a white,
58 bioturbated limestone, above which is a laminated chalk (738C-20R-5 96.2 – 97 cm / 377.172 –
59 377.18 mbsf), overlain by a 3 mm laminated gray clay containing the Iridium anomoly (738C-
60 20R-5 95.9 – 96.2 cm / 377.169 – 377.172 mbsf) (3, 6). Above the gray clay is a semi-indurated,
61 12 cm sequence of finely laminated white and green clay layers (738C-20R-5 82.5 – 95.9 cm /
62 377.035 – 377.169 mbsf) containing elevated PAH concentrations. Overlying the laminated clays
63 is a bioturbated light brown to white chalk (738C-20R-5 82.5 – 80.5 cm / 377.015 – 377.035
64 mbsf), above (80.5 cm / 377.015 mbsf to top of core) which is a light green, semi indurated chalk
65 with abundant darker burrows from *Zoophycos, Planolites,* and *Chondrites*) (6). Micrite is
66 abundant from the bottom of the core to 738C-20R-5 10 cm / 376.31 mbsf), and charcoal was
67 observed below 738C-20R-5 97 cm (377.18 mbsf) (3). Thierstein *et al*. (1991) propose the
68 sedimentation rate below the gray clay (below 738C-20R-5 96.2 cm / 377.172 mbsf) was 2.88
69 cm/kyr, above the gray clay between 70.9 – 95.9 cm / (376.919 – 377.169 mbsf) dropped to 0.2
70 cm / kyr, above which (738C-20R-5 70.9 cm / 376.919 cm and above) the sedimentation rate
71 increased to 0.9 cm/kyr. The boundary section is described above, and the boundary depth is
72 identified as the gray clay at 95.9 cm, where the Iridium spike occurs. Cretaceous calcareous
73 nannoplankton and planktonic foraminifera are observed above the boundary and are interpreted
74 as winnowing of sediment, as lamination suggests bioturbation was limited (7–10) For additional
75 discussion of the deposition of K-Pg boundary sediments at Site 738, see Bralower *et al*. (2020),
76 and for timing, core description, and images, see Thierstein *et al*., 1991 (**Supplemental Figure
77 S2**).
78
79 <u>Site 1262, Walvis Ridge</u>
80
81 Samples from the South Atlantic Ocean Site 1262 were obtained from Section 1262B-22H-4
82 between 1 and 148 cm (194.18 – 195.64 mbsf). The K-Pg boundary lies within Section 1262B-
83 22H-4 at 137 cm (195.59 mbsf). Below 137 cm (195.59 mbsf) is a tan – light pink clay rich
84 Cretaceous ooze, which is overlain by Paleocene brown clays. The boundary interval is highly
85 bioturbated and should be seen as gradational (3, 11) and is largely determined based on
86 biostratigraphy. There has not been an identified Iridium anomaly at 1262 to date, but an osmium
87 isotope anomaly spanning 115 cm of this core has been identified(11,
88 12)(12)(12)(12)(12)(12)(12). The micrite layer occurs between 1262B-22H-4 75 – 139 cm
89 (194.97 - 195.61 mbsf), and micrite decreases in abundance up to 1262B-22H-4 30 cm (194.52
90 mbsf) (3). Plant material and possibly charcoal were observed between 1262B-22H-4 133 – 136
91 cm (195.55 – 195.58). The records, including the osmium isotope anomaly, are smeared below
92 the boundary, likely as a result of bioturbation (12). For additional information on Site 1262, see

93   Zachos *et al*., 2004, Ravizza & VonderHaar, 2012, and Bralower *et al*., 2020 (**Supplemental**
94   **Figure S3**).
95
96   **2. Global observations of fire markers in K-Pg boundary sections**
97
98   Fire markers have been observed globally in K-Pg boundary records (Figure 1, main text),
99   though their sources may be more complex than previously interpreted. Burn markers from the
100   impact may differ from those observed in modern burns due to high temperatures, thermal
101   radiation (13), potential asteroid-derived hydrocarbons (14), target-rock derived hydrocarbons
102   (15, 16), ejection of material to the upper atmosphere, and re-entry of ejecta to Earth's surface
103   (17).
104
105   PAHs have been identified as burn markers in many K-Pg records, but have multiple sources,
106   atypical formation processes, and are affected by transport, which may complicate previous
107   interpretations. For example, in K-Pg studies, the presence of coronene has separately been used
108   as evidence for to the pyrolysis of organic matter from the target-rock (18, 19) and the
109   occurrence of high temperature wildfires (20) following the Chicxulub impact. In multiple
110   Northern Hemisphere sites including Chicxulub (*Supplemental Figure S5*), Caravaca, Spain (19),
111   Stevns Klint, Denmark (20), Beloc, Haiti (21), and Gubbio, Italy (20), coronene is the most
112   abundant parent PAH. Large, pericondensed PAHs including coronene can be linked to high
113   temperature burns (22), proximity to a point source, biodegradation (23), weathering, and
114   hydrothermal sources (24–26). Although coronene abundance has been the crux of multiple K-
115   Pg burn marker studies (19–21), this compound cannot be definitively linked a fuel source, or to
116   burning at all. Previous studies have also argued for wildfires based on the presence of retene in
117   K-Pg boundary sections (27), though fossil biomass combustion, diagenesis of pimaric and
118   abietic acids (18, 28), and weathering of sediments containing retene are non-negligible potential
119   sources. Many previous K-Pg studies have interpreted non-diagnostic PAHs as evidence for
120   wildfires or target-rock heating.
121
122   Below is a further review of observations made at sites with fire markers (the sites marked in
123   Figure 1, main text). Many sites in which the presence of soot, PAHs, or fullerenes were linked
124   to wildfires present evidence that is not a "smoking gun" for a fuel source, but rather can be
125   related to the combustion or pyrolysis of biomass and/or hydrocarbons.
126
127   <u>Site M0077A, Chicxulub Impact Crater</u>
128
129   The Chicxulub peak ring Site M0077 contains charcoal at the base of the transitional unit and
130   within the green marl capping the transitional unit (2). The lower charcoal layer is interpreted as
131   primarily delivered from coastlines ~800 km away into the crater, and the upper charcoal layer is
132   interpreted as either airfall from atmospheric fallout or from fires years after the impact (2).
133   PAHs observed at Chicxulub reach their highest concentrations at the base of the transitional unit
134   and remain elevated through the entire transitional unit. PAH composition is dominated by
135   alkylated forms of PAHs relative to parent PAHs and dominated by kinetic isomers relative to
136   thermodynamic isomers (see main text). Coronene is the most abundant PAH at Site M0077
137   within the boundary interval (below 616.58 mbsf / Section 007 – 40R – 1 34 cm), and PAH
138   distributions are dominated by larger (>4 rings) species. Retene concentrations are low compared

139 to other PAHs, and do not covary with the major changes in PAH concentration. We suggest
140 retene is likely from background inputs of biomass burning, but not necessarily the main source
141 of PAHs. The PAH composition at Site M0077 is consistent with the burning of petrogenic
142 carbon, which we interpret as target-rock derived. PAH concentrations for Site M0077 can be
143 observed in **Supplemental Dataset 1**, **Supplemental Figure S4,** and **Supplemental Figure S5.**
144
145 <u>Site 738, Kerguelen Plateau</u>
146
147 Charcoal was observed within K-Pg boundary sediments at Site 738 between 738C-20R-5 97 –
148 106 cm (377.18 – 377.27 mbsf) (3), within the section of impact-related sediments (below 738C-
149 20R-5 82.5 cm / 377.035 mbsf). PAH concentrations for most compounds are highest within the
150 post-impact deposits (below 377.035 mbsf) (**Supplemental Figure S6**). The most abundant
151 compounds are Chrysene (C0) and Benzo[ghi]perylene (GHI). The PAH spike at 87 cm (377.08
152 mbsf) within the laminated part of the boundary unit coincides with a major increase in most of
153 the larger individual PAHs, including perylene (PER). Coronene is below detection limits in all
154 samples. We attribute the lack of coronene to the distance from the crater itself or transport phase
155 of coronene (i.e. not a major PAH component in the plume), as it is the least prone species to
156 transport (see Supplemental Dataset 5). PAHs within the boundary interval are dominated by the
157 kinetically favored relative to the thermodynamically favored isomer (**Supplemental Figure S7**)
158 indicating a quick, high temperature formation process. Alkylation ratios at the PAH spike and
159 above shift towards more petrogenic, alkylated signatures (main text Figure 2). We take the
160 lowermost three samples (94 – 98 cm / 377.15 - 377.19 mbsf) with parent-dominated, pyrogenic
161 signatures to indicate a pre-existing, dominant fire regime that has previously been identified on
162 the Indian subcontinent leading up to the boundary (29). The samples between 94 – 98 cm /
163 377.15 - 377.19 mbsf have lower concentrations of PAHs than the K-Pg boundary spike.
164 Volcanic activity and a fire regime relating to the Deccan Traps is hypothesized as a driving
165 mechanism for the wildfire-derived PAHs on nearest landmass. We postulate that Site 738
166 contains both a pre-existing record of a fire regime related to wildfires, possibly driven by
167 volcanism, at Site 738, overprinted by the signature of fossil carbon burning at the impact site
168 from the Chicxulub impact, which we tie to the PAH spike around 377.08 mbsf. Retene
169 concentrations do not covary with the PAH spike, and we tie retene abundance to a background
170 fire regime, not deposition of material related to the impact itself.
171
172 <u>Site 1262, Walvis Ridge</u>
173
174 Bralower *et al*. (2020) recently documented the presence of disperse charcoal at Site 1262 (3).
175 PAH concentrations at Site 1262 reach their highest values within impact sediments (main text,
176 Figure 1) and reach maximums for most compounds within the bioturbated boundary sequence
177 (**Supplemental Figure S8**). Most PAHs reach maximum values coincident with the PAH spike
178 associated with the K-Pg boundary at 142 – 148 cm (195.58 – 195.64 mbsf). Chrysene (C0) is
179 the most abundant PAH associated with the boundary, closely followed by Fluoranthene (FL0),
180 Benz[a]anthracene (BaA), Pyrene (PY0), and Phenanthrene (P0). Perylene and retene both spike
181 concordantly with all other PAHs. While PAH alkylation patterns at the K-Pg boundary PAH
182 spike are consistent with a petrogenic source (see main text Figure 1), the dominant parent PAHs
183 are the kinetically favored over thermodynamically favored forms (**Supplemental Figure S9**),
184 indicating a quick, high temperature process such as combustion or pyrolysis. We link the PAH

185 signatures within the PAH spike at the K-Pg boundary to material from the target rock released
186 and heated upon impact. We suggest a background fire regime contributed to the fire marker
187 makeup at Site 1262.
188
189 MEG: Meghalaya, India
190
191 Pal *et al*. (2015) detailed the PAH spike below and coincident with the K-Pg boundary at the Um
192 Sohryngkew River section of the K-Pg boundary. For site descriptions and an in-depth analysis
193 of PAHs from the Indian subcontinent across the K-Pg boundary, refer to Pal *et al*., 2015. In the
194 Meghalaya section, associated with biozone CF3 (66.83 – 65.45 Ma) is a 2 mm thick clay layer
195 with which hosts an increase in PAH concentration. The most abundant PAHs observed at this
196 site include the 4-ringed species: fluoranthene, pyrene, chrysene, and benz[a]anthracene. Above
197 the initial PAH spike in biozone CF2 is an abundance of alkylated phenanthrenes. Pal *et al*. link
198 the abundance of 4-ringed PAHs in biozone CF3 to either fire following the K-Pg impact, or fire
199 associated with the Deccan volcanic activity (29). Kinetically favored isomers dominate within
200 the PAH spike, leading the authors to associate the PAH spike with fires following either the
201 impact itself or Deccan activity. Interestingly, biozone CF2 includes spherules typical of K-Pg
202 boundary sediments, and has petrogenic methylphenanthrene / phenanthrene signatures, but
203 mixed to kinetically favored fluoranthene / pyrene and phenanthrene / anthracene ratios (29). We
204 assert that the kinetically favored PAH isomer ratios and pyrogenic alkylation signatures at this
205 site represent the pre-impact fires. We suggest the above lying spherule layer with kinetically
206 favored isomers and abundance of alkylated PAHs is more consistent with a heated petrogenic
207 source (29) in biozone CF2. We suggest the layer with elevated PAH concentrations represents
208 fallout or reworked K-Pg impact material on top of a background fire record.
209
210 CAR: Caravaca, Spain
211
212 The Caravaca, Spain K-Pg section has been analyzed in multiple prior studies, which cite a PAH
213 spike associated with the boundary (19) and elevated concentrations of soot/charcoal (27, 30,
214 31). At Caravaca, Arinobu *et al*. (1999) documented a PAH spike and negative carbon isotope
215 excursion associated with the K-Pg boundary interval. The boundary clay is enriched 112 – 154
216 fold in PAHs, notably coronene, benzo[ghi]perylene, and benzo[e]pyrene, which the authors
217 associate with a pyrogenic origin (19). The carbon isotope excursion and spike in PAHs, notably
218 the large, pericondensed forms mentioned above, led the authors to cite global wildfires
219 combusting 18-24% of the terrestrial biosphere as the source of the isotopic excursion and PAHs
220 (19). Because large, pericondensed species, such as coronene, can be formed can be linked to
221 high temperature burns (22), proximity to a point source, biodegradation (23), weathering, and
222 hydrothermal sources (24–26), we suggest Arinobu *et al*. (1999) present PAH data that cannot be
223 tied to a fuel source, contrary to their interpretations. Gilmour *et al*. note 14% of carbon in the K-
224 Pg boundary sediments was in the form of soot (27). Additionally, K-Pg boundary sediments
225 were analyzed by Wolbach *et al*., (1985 & 1988), in which the authors identify an increase in
226 elemental carbon to 0.010 g/cm_3 with an $\delta_{13}C$ value of -25.00‰. From the abundance of soot at
227 global sites, the authors cite $7 \times 10_{16}$ g of soot released from wildfires following the impact (31).
228
229 KLI: Stevns Klint, Denmark
230

Stevns Klint, Denmark K-Pg boundary sediments have previously been worked on by Venkatesan & Dahl (1989), Wolbach *et al.* (1985, 1988), Gilmour *et al.* (1990), and Harvey *et al.* (2008). Venkatesan & Dahl (1989) noted a PAH spike coincident with the K-Pg boundary interval (30 ppb) coincident with the iridium anomaly. Coronene is the most abundant PAH at Stevns Klint. Due to the decreasing concentration of phenanthrenes (and anthracenes) and fluoranthenes (and pyrenes), with increasing alkylation, the authors link the PAH spike to wildfires following the K-Pg impact (20). Wolbach *et al.* (1988) identified 0.011 g/cm$_3$ of elemental carbon (soot) with a δ_{13}C value of -25.81‰ at the K-Pg boundary. Stevns Klint was used by Wolbach *et al.* (1988) to calculate 7 x 10$_{16}$ g of soot released by wildfires following the impact (31). Based on the isotopic similarity to other sites, Wolbach *et al.* (1988) link the soot observed in Stevns Klint to wildfires. Gilmour *et al.*, note that soot accounts for 21% of carbon observed at Stevns Klint (27). While the earlier studies suggest PAHs and soot are derived from wildfires, Harvey *et al.* (2008) described the presence of carbon cenospheres, material derived from the burning of oils or concentrated petrogenic carbon, and linked their abundance with the burning of the target rock at Chicxulub (16). At Stevns Klint, 646 cenospheres of 5.1 µm diameter per gram of rock and 150 cenospheres of 8.5 µm diameter were observed in the fireball layer and other K-Pg sediments respectively (16). To produce the global abundances of cenospheres, which Harvey *et al.* (2008) predicted the global inventory of 2.3 x 10$_{12}$ g would require the combustion of 9.2 x 10$_{16}$ g of carbon (16). Harvey *et al* (2008) link the carbon-related anomalies at Stevns Klint to the combustion of the Chicxulub target rock upon impact, whereas Venkatesan & Dahl (1989), Wolbach *et al.* (1985, 1988), and Gilmour *et al.* (1990) link K-Pg carbon anomalies at Stevns Klint to wildfires. None of the evidence presented is conclusive for a single source, but rather, seems to imply the input of both burned petrogenic and wildfire-derived carbon.

GUB: Gubbio, Italy

The debate over whether wildfires or burning of a target rock following the Chicxulub impact has previously been invoked at Gubbio, Italy by Venkatesan & Dahl (1989), Wolbach *et al.* (1988), and Gilmour *et al.* (1990). Venkatesan & Dahl (1989) noted a PAH spike over 75 times background levels associated with the iridium anomaly at Gubbio. Coronene, a pericondensed, 7 ring PAH, is the most abundant PAH at the K-Pg boundary at Gubbio. The set of selected PAHs was most abundant in the non-alkylated parent form, leading the authors to link K-Pg PAHs to wildfires. There is no background (pre- or post- boundary) data presented within this study to compare with the boundary interval (20). Wolbach *et al* (1988) reported 0.013 g/cm$_3$ of elemental carbon with a δ_{13}C value of -25.48‰ at Gubbio, which is similar to the concentrations and isotopic values of elemental carbon observed at other sites, leading the authors to link the presence of soot to wildfires (31). Gilmour *et al.* report that soot makes up for 17% of the carbon in K-Pg boundary sediments, which they relate to wildfires (27). Venkatesan & Dahl (1989), Wolbach *et al.* (1988), and Gilmour *et al.* (1990) made a case for wildfires based on carbon anomalies at the K-Pg boundary. The data presented suggests a wildfire regime but is inconclusive in ruling in or out additional sources.

WOO: Woodside Creek; New Zealand

276　The debate over the source of anomalous K-Pg boundary carbon at Woodside Creek, New
277　Zealand has previously been discussed by Venkatesan & Dahl (1989), Wolbach *et al*. (1985,
278　1988), Gilmour *et al*. (1990), Heymann *et al*. (1994), and Harvey *et al*. (2008). Venkatesan &
279　Dahl noted a PAH spike 11 times above background levels dominated by low molecular weight
280　PAHs and relatively devoid of high molecular weight, pericondensed forms such as coronene
281　(20). We hypothesize the PAH size distribution is related to transport, as this site is one of the
282　furthest from the impact crater itself, similar to the PAH composition at Site 738. Woodside
283　Creek demonstrates a dominance of the di-methylated PAHs, and presents a signature similar to
284　petroleum (20), which the authors relate to a combustion source from moderate to high
285　temperature fires (400 – 800 ℃) (20). The interpretation of di-methylated PAHs being sourced
286　from fires is likely a misinterpretation, and rather suggests a petrogenic source of carbon (32).
287　Wolbach *et al*. (1985, 1988) noted a heightened abundance of soot (black carbon) at Woodside
288　Creek, amounting to 0.0048 g/cm_3 with a $\delta_{13}C$ value of -25.42‰ (30, 31). Gilmour *et al*. (1990)
289　report that 69% of carbon at Woodside Creek is soot, linking the abundance of soot to wildfires
290　following the Chicxulub impact (27). Heymann *et al*. (1994) reported the presence of fullerenes
291　in the K-Pg boundary sediments at Woodside Creek. The C_{60} fullerene was 0.1 – 0.2 ppm of the
292　associated soot, which the authors associate with temperature fires (> 1000 ℃). The
293　concentration of fullerenes was two to three orders of magnitude above background
294　concentrations. Fullerenes, including a C_{70} fullerene, were also observed at the nearby
295　Flaxbourne River site (33). The authors hypothesize fullerenes were derived from wildfires set
296　off by the Chicxulub impact (33), though these temperatures were likely not sustained in regional
297　fires outside of the impact site (34). Fullerenes can also be produced by the burning of petrogenic
298　carbon, and temperatures upon impact exceeded the temperature of fullerene generation (35).
299　Harvey *et al*. (2008) observed carbon cenospheres at Woodside Creek (4994 cenospheres with
300　6.1 µm diameter per gram sediment), which they take as evidence for the dispersal and heating
301　of crustal material from the Chicxulub target rock (16). There is a lack of consensus about the
302　source of anomalous carbon (fullerenes, PAHs, carbon cenospheres, and soot) at Woodside
303　Creek, NZ.
304
305　HOK: Kawaruppu, Hokkaido, Japan
306
307　Mita & Shimoyama (1999) documented a PAH spike associated with a K-Pg boundary claystone
308　section in Hokkaido, Japan. Specifically, concentrations of 4 ringed and larger PAHs are
309　elevated within the claystone (specifically within the bottom two thirds of the claystone) than
310　above or below sediments. Parent PAH dominance over alkylated PAHs was assumed from the
311　dominance of phenanthrene to alkylated homologues. Mono and dimethyl PAHs demonstrate a β
312　over α isomer dominance. Phenanthrene abundance was greater than anthracene, and pyrene
313　abundance was greater than chrysene, which the authors linked to the enhanced stability of
314　pericondensed over linear PAHs, but not necessarily fires. The authors did not find sufficient
315　evidence to link the PAH distributions to wildfires, but noted that a PAH spike at Kawaruppu
316　was present (36).
317
318　SAS: Saskatchewan, Canada (Rock Creek East & Wood Mountain Creek)
319
320　In Figure 1 (main text), we use SAS to represent both the Rock Creek East and Wood Mountain
321　Creek sites from Saskatchewan, Canada. Harvey *et al*. (2008) documented the presence of

carbon cenospheres at Rock Creek East, and Belcher *et al*. (2005) documented a decrease in charcoal abundance relative to Cretaceous and Paleogene rocks. Both studies cite heating of material from the Chicxulub target rock but not wildfires as the source of the carbon anomaly at the K-Pg boundary. Harvey *et al*. (2008) documented 83 carbon cenospheres with a 25.2 µm diameter per gram of rock within the ejecta layer and 875 carbon cenospheres with a 26.6 µm diameter in the fireball layer at Rock Creek East, Saskatchewan, Canada (16). The authors link the presence of carbon cenospheres to the heating of $9.4 \times 10_{17}$ g crustal carbon at Chicxulub during the impact, positing that the carbon anomaly in K-Pg boundary sites can only be explained by high temperature alteration and dispersion of the thermally mature target rock, and not wildfires (16). Additionally, Belcher *et al*. (2005) performed charcoal analyses and reported that 99% of the K-Pg organic material is non-charred, whereas 94% of Cretaceous and 68% of Tertiary organic matter was non-charred (18). Because this site (and others used within Belcher *et* al. (2005)'s analyses) are near the Chicxulub crater, these should be the sites where wildfires occurred (34). Belcher *et al*. (2005)'s work demonstrates a decrease in the amount of charred material or an increase in the amount of unburned material within K-Pg boundary sediments, which contrasts the wildfire hypothesis (18). Taken together, Harvey *et al*. (2008) and Belcher *et al*. (2005)'s work demonstrates evidence for the heating and dispersion of crustal organic matter but do not support global wildfires.

ADM: Arroyo de Mimbral, Mexico

Kruge *et al*. (1994) document a PAH spike and an elevated amount of fossil charcoal at the Arroyo de Mimbral, Mexico K-Pg section. Kruge *et al*. (1994) report that 70% of the organic material is semi charred plant material (semifusinite), 20% is charred plant tissue (pyrofusinite), and 10% is vitrinite. The reflectance of all three pools of macerals (average > 1.3% R_o) is much higher than expected for the in situ thermal maturation expected for the low heat gradient and sample burial depth of <1 km (37). The high thermal maturity interpreted from the reflectance of macerals, the absence of liptinite, and the abundance of aromatic compounds led Kruge *et al*. (1994) to interpret the Arroyo de Mimbral deposit proximal to Chicxulub as the aftermath of a thermal pulse following the impact (37). The authors hypothesize that the "fossil charcoal," or organic macerals with greater interpreted thermal maturity from vitrinite reflectance than possible in the basin, was sourced from shock heating of nearby coastal vegetation, quenching, and transport to the 600 m deep ocean basin (37). We suggest an alternative explanation may be the burning of more thermally mature material from the target rock itself, or reworking of fossil charcoal on land during resurge. The presence of fossil charcoal alone cannot be definitively linked to source or generation process.

ND: Mud Buttes, North Dakota, USA

Belcher *et al*. (2009) present an analysis of charred and non-charred plant remains as well as PAHs from K-Pg boundary sections from the Western Interior Seaway Mud Buttes site in North Dakota, USA. A spike in parent PAHs is observed, and is dominated by small, 3-4 ringed compounds. Belcher *et al*. (2009) argue that the appearance of a PAH spike lower (earlier in the record) in K-Pg boundary sequences in sites more proximal to the Chicxulub impact crater and, the appearance of a PAH spike higher (later in the record) in more northern, more distal K-Pg boundary sites (including ND) is evidence for Chicxulub as the source of hydrocarbons. Based

368 on a cluster analysis of K-Pg impact deposits and possible sources, Belcher *et al.* (2009) argue
369 that the clustering of K-Pg boundary PAH compositions with combusted fossil fuels, and not
370 with combusted biomass, links the PAHs at the boundary to the combustion of fossil
371 hydrocarbons from the Chicxulub target rock (38). The fireball layer at ND, but not the ejecta
372 layer, contains concentrations of parent PAHs exceeding background levels, and charcoal
373 abundances 20 times lower than background levels (38). Ultimately, Belcher *et al.* (2009) link
374 the low charcoal abundances and elevated, petrogenic PAH signature at ND to the combustion of
375 hydrocarbons at the impact site, and not to wildfires.
376
377 CO: Colorado, USA (Madrid East South, Clear Creek North, & Berwind Canyon)
378
379 Belcher *et al.* (2009) present an analysis of charred and non-charred plant remains and parent
380 PAHs from K-Pg boundary sections from the Western Interior Seaway sites in Colorado, USA:
381 Madrid East South, Clear Creek North, and Berwind Canyon. These are the three most proximal
382 sites to the Chicxulub impact crater used in Belcher *et al.*'s 2009 study. Belcher *et al.* identify a
383 PAH spike at each site in the lower portion of the boundary impact sediments, which they relate
384 to the proximity to the impact site. The ejecta and fireball layers at all 3 CO sites are above
385 background levels, and all display a "hydrocarbon" signature. PAHs that dominate the
386 composition in CO sites include 3 and 4 ringed species. Cluster analysis of PAH compositions at
387 each site and possible sources demonstrate a clustering of boundary PAH compositions with
388 those of combusted hydrocarbons, leading the authors to conclude that hydrocarbon combustion
389 at the impact site was the source of parent PAHs in western interior seaway sites, and not
390 wildfires. The CO sites are >2,300 km from the impact site, and would possibly have been
391 affected by the thermal pulse, but show a decrease in charred plant remains by a factor of 20
392 coincident with the K-Pg boundary layer (38). Belcher *et al.* (2009) link the low charcoal
393 abundances and the elevated, petrogenic PAH signatures at CO sites to the combustion of
394 hydrocarbons at the impact site, not wildfires.
395
396 CR: Chancet Rocks, New Zealand
397
398 The Chancet Rocks, New Zealand K-Pg record was analyzed by Gilmour *et al.* (1990) and
399 Wolbach *et al.* (1988), in which the authors cite the abundance of elemental carbon (soot) with a
400 globally identical carbon isotopic signature to global wildfires following the impact at
401 Chicxulub. At Chancet Rocks, black carbon is elevated (0.025 g / cm3), and has a δ_{13}C value of -
402 25.42‰. 23% of the carbon is in the form of soot, and soot is 600 times more concentrated than
403 in Cretaceous sediments (27, 31). Both Wolbach *et al.* (1988) and Gilmour *et al.* (1990) cite
404 wildfires as the source of elevated soot concentrations in K-Pg boundary intervals at Chancet
405 Rocks, NZ due to its nearly identical values to PAHs at other globally dispersed sites. We
406 suggest that the presence of identical soot could be from a single source (the target rock) and not
407 only wildfires, though cannot distinguish the two sources based on the information presented for
408 the Chancet Rocks site.
409
410 BEL: Beloc, Haiti
411
412 Kaiho *et al.* (2016) demonstrate an elevated abundance of PAHs, notably, coronene, at the Beloc,
413 Haiti site proximal to the Chicxulub impact crater. PAH concentrations and coronene

concentrations peaked coincidently with the iridium layers within the K-Pg boundary deposit at Beloc (39) . Kaiho *et al.* (2016) suggest the elevated coronene / (coronene + benzo[e]pyrene + benzo[ghi]perylene) ratios are from petroleum combustion, whereas low values are more representative of biomass combustion. The low carbon preference index values in the K-Pg boundary interval were used to argue that the fuel source was older than the plants at the time of the impact, and further cite the Jurassic source rocks of the Cantarell oil field as a potential source (39). At Beloc, the $\delta_{13}C$ values of *n*-alkanes decreased by 3-4‰. Kaiho *et al.* (2016) conclude that the "burned material" observed in the K-Pg deposit at Beloc is sourced from fossil organic matter from the ejected crust at Chicxulub, and not wildfires. Further, we suggest the larger carbon isotope excursion at the proximal Beloc, Haiti site compared to the smaller carbon isotope excursion at the more distal Caravaca, Spain site (19) may be due to proximity to the impact site and amount of impact related material delivered to sediments at Beloc. Kaiho *et al.* (2016) estimated the total amount of soot ejected to the stratosphere using the concentrations of coronene, benzo[e]pyrene, and benzo[ghi]perylene, which they cite as components of soot (39). The authors estimated between 500 – 2600 Tg of black carbon was ejected to the stratosphere, which could have remained on the order of years, blocking out sunlight, inhibiting photosynthesis, and causing rapid cooling (39). Again, we note that the presence of pericondensed PAHs, such as coronene, cannot be linked to a fuel source.

BRZ: Brazos, Texas, USA

Heymann *et al.* (1998) detailed the anomalous carbon associated with the K-Pg boundary deposit at Brazos, Texas, USA and linked the presence of soot and fullerenes to wildfires. Soot in Brazos River sections increased to $1.4 \times 10_4$ ppm and carbon concentrations increased to $2.2 \times 10_4$ ppm in K-Pg boundary sections. The concentration of soot is 22 times higher than the global average reported at that time, which Heymann *et al.* (1998) link to Brazos's proximity to the impact site. Fullerenes were also detected in the K-Pg sections at Brazos. Heymann *et al.* (1998) link the abundance of soot and the presence of fullerenes to high temperature wildfires in this proximal site following the K-Pg impact (40). Coupled with the reported increase in sulfur content at Brazos, which is likely from the target rock itself (40), we suggest the presence of fullerenes and soot may also have resulted from the release and burning of fossil hydrocarbons in the target rock at Chicxulub. With the data presented, the possible sources cannot actually be disentangled.

KEF: El Kef, Tunisia

Wolbach (1990) details the presence of soot at many K-Pg boundary sites, including the highly studied El Kef, Tunisia section. The El Kef section presents an elevated concentration of elemental carbon, similar to other sites, which is linked to the presence of wildfires (41). We note that soot itself is not capable of determining source.

AGO: Agost, Spain

Gilmour *et al.* (1990) and Wolbach (1990) report on the presence of elevated carbon and soot in the Agost, Spain K-Pg boundary section. At Agost, carbon concentrations reach 3.8 mg/g, of which about 2% is in the form of soot. No isotopic composition is reported for the soot, likely due to the relatively low concentrations compared to other sites. Gilmour *et al.* (1990)

460 hypothesize that the variable soot concentrations at boundary sites (i.e. the nearly 20 times higher
461 concentration of soot at the nearby Caravaca, Spain site) as a function of the localized fallout of
462 soot from the atmosphere controlled by rainfall (27, 41). While Gilmour *et al.* (1990) link the
463 presence of localized soot to wildfires, the mechanism they cite (global fallout controlled by
464 precipitation) is not wildfire specific, making the presence of soot not specifically related to
465 wildfires, but rather, the combustion and transport processes, irrespective of carbon source.

467 SUM: Sumbar, Turkmenistan

469 Wolbach *et al.* (1990) report an increase in soot associated with the K-Pg boundary. Soot
470 abundance increased 7 cm into the section, which was above the iridium anomaly at 0-1 cm into
471 the boundary section (42). Soot may be linked to a heating process, but not a fuel source.

473 FLA: Flaxbourne River, New Zealand

475 Heymann *et al*. (1994) document the presence of fullerenes in K-Pg boundary sediments. The
476 C_{60} fullerene was $0.1 - 0.2$ ppm of the associated soot, which the authors associate with
477 temperatures above 1000 ºC. The concentration of fullerenes was two to three orders of
478 magnitude above background concentrations. C_{70} fullerene was observed at Flaxbourne River
479 (33). The authors hypothesize fullerenes were derived from wildfires set off by the Chicxulub
480 impact (33), though temperatures over 1000 ºC were not likely to have been sustained in regional
481 fires outside of the impact site (34), making Heymann *et al*. (1994)'s interpretation of high
482 temperature wildfires in one of the most distal sites from the crater questionable. We suggest the
483 presence of fullerenes could have also been linked to high temperature reactions of fossil
484 hydrocarbons in the target rock upon impact (T > 1465 ºC) (35), ejection to the upper
485 atmosphere, global dispersion within the dust cloud, and delivery via fallout or rainout.

487 **3. Assessing sources of carbon at the K-Pg boundary: target rock, biomass, or bolide?**

489 The fuel source that lead to the global abundance of soot, PAHs, and carbon cenospheres has
490 previously been assessed using mass balance calculations. Below, we present additional mass
491 balance calculations using the PAH abundance observed to assess whether the target rock,
492 biomass, or a bolide could have delivered the PAH signature observed at the boundary. We offer
493 no additional insight, as all sources present a sufficiently massive amount of material, making all
494 sources possible from a mass balance perspective. From a mass balance perspective, none of the
495 proposed sources are unreasonable explanations for the PAH concentrations observed at the K-
496 Pg boundary.

498 Harvey *et al.* (2008) assessed whether organic matter in the target rock would have been
499 sufficient to drive the carbon cenosphere abundances in K-Pg boundary sediments. Based on the
500 concentration of cenospheres at the example Woodside Creek, New Zealand (WOO) section,
501 with a sediment density of 4.5 g/cm3, a cenosphere layer thickness of 0.6 cm, and a cenosphere
502 concentration of 4994 cenospheres / g, Harvey *et al*. (2008) concluded the target rock at
503 Chicxulub would have been a sufficient source of fuel to result in the observed cenosphere
504 abundance (16), even if the target rock had an average crustal organic carbon composition. Using
505 the mean cenosphere diameter (6.1 µm), and the mean carbon cenosphere density (0.28 g/cm3)

506 (43), Harvey *et al.* (2008) calculated a global cenosphere inventory of 2.3 x 10^{12} g in K-Pg
507 boundary sediments. Harvey *et al.* (2008) calculated that 7.6 x 10^{16} g of dispersed organic
508 material would be required to drive the cenosphere abundance if 0.003% of the burned organics
509 would be transformed into cenospheres (44), which is less than the expected 10^{17} g of C expected
510 in the volume of Cretaceous rocks ejected (15). While Harvey *et al.* (2008)'s assessment of
511 impact crater volume is incorrect (45) their assessment of carbon in the target rock is likely the
512 correct order of magnitude (15).
513
514 Gilmour *et al.* (1990) argue that biomass in a typical fire alone would not have produced
515 sufficient elemental carbon unless the fraction of biomass converted to soot was elevated in post-
516 impact fires, or if there was an additional fossil carbon source from the crater (27). Gilmour *et al.*
517 (1990) attempted to explain the 0.012 g/cm^2 of soot at the K-Pg boundary through the
518 combustion of the 0.2 g/cm^2 of above ground biomass (46) or the possible cretaceous maximum
519 value of 0.6 g/cm^2 using a soot yield calculation. The fraction of organic matter converted to soot
520 is equal to the product of the fraction of biomass carbon burned, the fraction of burned biomass
521 that is converted to smoke, the fraction of elemental carbon in smoke, and the above ground
522 biomass concentration (27). Gilmour *et al.* (1990) determined that the concentration of soot in K-
523 Pg boundary records was 12-18 times higher than the amount produced from a high intensity
524 wildfire, which lead the authors to conclude that either multiple carbon sources need to be
525 invoked or that soot production from post impact fires was greater than modern observations
526 (27).
527
528 Arinobu *et al.* (1999) used the presence of pericondensed PAHs and the negative carbon isotope
529 excursion observed in K-Pg boundary sediments to argue for a burning of 18 – 24 % of
530 aboveground biomass following the impact. Using the -1.4 to -1.8‰ shift in C_{29} alkane $\delta^{13}C$
531 records as an indication of a -1.4 to -1.8‰ shift in atmospheric $\delta^{13}C$, ~10^{18} g of above ground
532 cretaceous biomass, the end Cretaceous biomass value of -25.66‰ (47), a burning efficiency of
533 ~50%, and the end Cretaceous atmospheric $d^{13}C$ value of -7.5‰, Arinobu *et al.* (1999)
534 calculated that between18 and 24% of above ground biomass would be needed to drive the
535 observed carbon isotope excursion. Based on isotopic shifts across the K-Pg boundary, Arinobu
536 *et al.* (1999) argue that biomass is more than sufficient to drive the geochemical shifts observed
537 across the K-Pg boundary (19).
538
539 Robertson *et al.* (2013) calculated that 1.8 – 6.0 x 10^{16} g of carbon would have been burned at
540 the Chicxulub impact crater based crater area the global average concentration of organic carbon
541 per area (45). Robertson *et al.* (2013) argue this amount of carbon would not have been enough
542 to drive the observed soot abundance in boundary layers (Wolbach *et al.*, 1988; Robertson *et al.*,
543 2013), whereas Kaiho *et al.* (2016) used this estimate to argue for enough soot to drive global
544 darkness on the order of years (39). Alternately, Kenkmann *et al.* (2004) suggest that ~10^{17} g of
545 organic carbon was present in the evacuated crater based on crater volume and the concentration
546 of organic matter in nearby analogous Cretaceous sections from the Yax-1 corehole (15). The
547 estimate of ~10^{17} g of organic carbon is discounted from the concentration of carbon in
548 Cretaceous rocks at Yax-1, assuming 60% of the carbon in the Yax-1 core migrated into
549 carbonates post-impact (15).
550

551   To assess whether PAHs at the K/Pg boundary are from wildfires (biomass), the bolide itself
552   (meteoritic material), or the impact target rock (petrogenic / pyrolyzed petrogenic), we assessed
553   whether there would be enough carbon in each reservoir to drive a PAH anomaly observed in
554   this study (Sites M0077, 738, 1262).
555
556   We first assessed whether the PAHs delivered by the bolide would be enough to drive a PAH
557   anomaly either globally or within the Chicxulub impact deposits. First, in order to deliver an
558   adequate amount of carbon to Earth, the bolide would need to have been a carbonaceous
559   chondrite. The average concentration of total PAHs in a carbonaceous chondrite is between 15 –
560   28 µg PAH / g rock (48, 49). For a 5 km radius meteorite (estimates of the Chicxulub impactor
561   are up to 6 km radius) with a PAH composition on the high end for carbonaceous chondrites (28
562   µg/g), the meteorite would carry 3.8×10^{12} g of aromatic compounds. If the aromatics were
563   dispersed globally and evenly in a 1 cm thick clay layer, we would expect 2.9×10^{-7} g aromatics
564   / g rock, which is two orders of magnitude less than what was measured at Chicxulub and Site
565   1262, and three orders of magnitude less than observed at Site 738. While the observed
566   concentration of PAHs is 1-3 orders of magnitude greater than the predicted PAH concentration,
567   this is not strong enough evidence to refute the bolide as the initial source of PAHs.
568
569   To determine whether the excavation, and likely ignition or release to the atmosphere of $\sim 10^{17}$ g
570   carbon (15) would be enough to drive the observed PAH excursion, we calculated the amount of
571   PAHs that would be released from unburned petrogenic material (directly excavated, remaining
572   in atmosphere) and if the target rock had burned. From an oil burning experiment, $\sim 30\%$ of the
573   initial extractable organic matter was in the form of PAHs, and $\sim 22\%$ of burned organic matter
574   residue was comprised of PAHs. If we conservatively assume that 1% of the organics are in the
575   form of oils, the direct release of target rock organics would have led to 10^{14} g of aromatic
576   material dispersed globally, or if it was burned, and 5-15% of the initial weight of organic matter
577   remained unreacted (50), 10^{13} g of organic matter would remain, and thus 10^{12} g of PAHs would
578   be globally dispersed. If this material was dispersed globally, it would lead to a global 1-cm thick
579   boundary deposit of 2.8×10^{-7} g PAH / cm^3 layer if all organics were combusted, which is the
580   same order of that we observe in this study. This calculation demonstrates that the target rock is a
581   possible source of the PAH spike, but we note that mass balance calculations are ineffective as
582   evidence for or against carbon sources in K-Pg studies, as they incorporate assumptions on
583   carbon concentrations, burning efficiencies, and temperature, which all affect burn product
584   production.
585
586   Using the assumption of $\sim 10^{18}$ g of aboveground biomass (19, 47), this is an order of magnitude
587   greater than the carbon hosted in the target rock (15) ,making the biomass combustion a
588   sufficient driver of the PAH spike. We note that different sources of fuel, different burning
589   parameters, and different temperatures and times of a burn will affect the generation of burn
590   products. Because we cannot constrain the specifics of burning following the Chicxulub impact,
591   it is not possible to predict the specific fractions of fuel that would have been converted to each
592   burn product. Using mass balance calculations is not a viable way to rule out possible fuel
593   sources for the carbon anomalies in K-Pg boundary layers due to the similarities in carbon
594   reservoir size and unknowns surrounding the burning efficiencies and parameters. In addition,
595   ruling in or out carbon sources is likely an inefficient assessment, as both biomass burning and
596   release of carbon from the target rock occurred following the Chicxulub impact.

597
4. Alkylation patterns of homologous series of PAHs

599
Chicxulub Site M0077 demonstrates a pyrogenic PAH pattern in all samples. PAH patterns for the homologous series of phenanthrenes (**Supplemental Figure S10**), fluorenes (**Supplemental Figure S11**), chrysenes (**Supplemental Figure S12**), pyrenes (**Supplemental Figure J**), and dibenzothiophenes (**Supplemental Figure K**) demonstrate petrogenic and weathered profiles, as evidenced by the convex patterns peaking at di-methylated form and the increasing concentration with increasing alkylation respectively. Fluorene and dibenzothiophene homologous series present profiles that are relatively too weathered to interpret.

Alkylated PAH Distribution Index (APDI) values presented in the main text came from pyrene, but can also be computed for other homologous series, namely chrysene and phenanthrene. Pyrene APDI values for Site M0077 are consistently negative, indicating a petrogenic source (51) (**Supplemental Figure S15**). Pyrene was selected for the main text because it was the most consistently present and had the least weathered profile across all sites. APDI from Chrysene (**Supplemental Figure S16**) also presents consistently negative values which can be linked to petrogenic sources, while APDI values from phenanthrene are more random and less reliable because it was lower in concentration and had a more weathered profile, which can overshadow source patterns (**Supplemental Figure S17**).

Kerguelen Plateau Site 738 demonstrates PAH alkylation patterns both pyrogenic and petrogenic signatures at various depths. PAH patterns for the homologous series of phenanthrenes (**Supplemental Figure S18**), fluorenes (**Supplemental Figure S19**), chrysenes (**Supplemental Figure S20**), pyrenes (**Supplemental Figure S21**), and dibenzothiophenes (**Supplemental Figure S22**) that likely are related to multiple sources of PAHs. APDI values for pyrene (**Supplemental Figure S23**), chrysene (**Supplemental Figure S24**), and phenanthrene (**Supplemental Figure S25**) demonstrate a shift towards more negative values (pyrene and chrysene) at and above the K-Pg boundary.

Walvis Ridge Site 1262 demonstrates PAH alkylation patterns which we attribute to mixed signatures due to multiple input sources. Homologous series of phenanthrenes (**Supplemental Figure S26**), fluorenes (**Supplemental Figure S27**), chrysenes (**Supplemental Figure S28**), pyrenes (**Supplemental Figure S29**), and dibenzothiophenes (**Supplemental Figure S30**) demonstrate mixed signatures, but more petrogenic signatures associated with the PAH spike (see main text Figure 1). APDI values for pyrene (**Supplemental Figure S31**), chrysene (**Supplemental Figure S32**), and phenanthrene (**Supplemental Figure S33**) demonstrate more petrogenic signatures (negative values) associated with the two samples within the K-Pg PAH spike, followed by a shift toward positive, pyrogenic values that may represent a background fire regime, and ultimately a shift towards more negative, petrogenic values further into the Paleogene.

5. Nonmetric Multidimensional Scaling

640
Nonmetric Multidimensional Scaling (NMDS) was chosen as the ordination method due to excessive clustering (referred to as a "dust bunny effect") present when the traditionally used

643 Principal Components Analysis (PCA) and Detrended Correspondence Analysis (DCA) were
644 initially tested with the dataset. NMDS works better for non-normal or non-gaussian
645 distributions, as it does not carry inherent assumptions of linear relationships between variables
646 (52). The initial dataset consisted of all PAHs excluding the naphthalene homologues,
647 acenaphthene, and acenaphthylene due to their low concentrations. The initial dataset consisted
648 of all samples from Sites M0077, 738, and 1262. Zeros were replaced by values of 0.01. PAH
649 integrations were replaced by fractional abundance, $(b_{ij} = \frac{x_{ij}}{\sum_{j=1}^{n} x_{ij}})$, where, rows (i) are samples and

650 columns (j) are variables (PAHs), where all compounds in a sample had a value between 0 and 1,
651 and the sum of all PAHs in a sample was 1. The dataset contained one outlier from Site 738
652 (738C-20R-5 8-10 cm) that was removed.
653
654 Nonmetric Multidimensional Scaling (NMDS) is an indirect gradient analysis method through
655 which rank distances among objects is preserved, and no assumptions (i.e. no linearity,
656 unimodal, or gaussian relationships assumed) are made within the algorithm. Due to the lack of
657 assumptions, NMDS works well with data that are not normally distributed or whose scales do
658 not necessarily have meaning. NMDS employs an iterative algorithm to find the best rank
659 positions of samples based on variable attributes in a new, reduced number of dimensions in
660 order to make sample gradients and data structure apparent.
661
662 Starting with the n x p matrix, **A**, where n is the 41 samples and p is the 39 variables (PAHs), a n
663 x n (41 x 41) distance matrix of dissimilarities between samples is calculated using Bray-Curtis
664 distance measures. The Bray Curtis (Sørensen) distance measures, δ_{ij}, where $\delta_{ij} =$
665 $(\sum_{j=1}^{p} |a_{i,j} - a_{n,j}|) / (\sum_{j=1}^{p} a_{i,j} + a_{n,j})$, where $a_{i,j}$ represents each element (i=row, j=column). Δ
666 is the matrix of all distance measures (δ) which we aim to preserve using NMDS. Next, an initial
667 starting configuration is randomly assigned as the matrix **X**, an n x k matrix where k is the
668 number of dimensions included in the ordination. In this study, k values of 1 through 6 were
669 used, for which **X** with the smallest k value explaining the greatest amount of structure in the
670 data was chosen. Each entry (x_{il}) in **X** was normalized so that $x_{il} = \frac{x_{il} - \overline{x_{il}}}{\sum_{l=1}^{k} \sum_{i=1}^{n} \frac{(x_{il} - \overline{x_{il}})^2}{n*k}}$, where $\overline{x_{il}}$ is

671 the mean value of each entity. Following the standardization of **X**, the n x n matrix of Euclidian
672 distances between samples in k space, **D**, is calculated. Following the calculation of both Δ and
673 **D**, the elements of Δ were ranked in ascending order, after which the elements of **D** were placed
674 in the same order as Δ, after which $\widehat{D}$ is calculated. $\widehat{D}$ contains elements $\hat{d}_{ij}$, the replacement
675 values for d_{ij} from the **D** matrix that improve monotonicity when Δ ranks and **D** ranks are plotted
676 against each other. Using the sum of squares of the difference between each d_{ij} and $\hat{d}_{ij}$, stress,
677 **S*** is calculated, where $S^* = \sum_{i=1}^{n-1} \sum_{j=i+1}^{n} (d_{ij} - \widehat{d_{ij}})^2$. Stress was standardized using Kruskal's
678 stress formulation, where $S = S^* | \sum_{i=1}^{n-1} \sum_{j=i+1}^{n} d_{ij}^2$, after which the square root of scaled stress,
679 S, is taken to calculate S_R, which is analogous to the standard deviation, where $S_R = \sqrt{S}$. Next,
680 the stress was minimized by changing the configuration of sample units in k space using the
681 steepest-descent minimization algorithm. For each point i, the negative gradient of stress was
682 calculated, from which the k- length gradient vector is calculated, where $g_{hl} =$
683 $S \sum_{i=1}^{n} \sum_{j=1}^{n} (\Delta^{hi} - \Delta^{hj}) [\frac{d_{ij} - \widehat{d_{ij}}}{S^*} - \frac{d_{ij}}{\sum_{i,j} d_{ij}^2}] \frac{(x_{il} - x_{jl})}{d_{ij}}$, where i and j are indexes of the n points, l is
684 the index of each dimension, , where g_{hl} indicates a shift of a third point h in the lth dimension. Δ_{hi}

685 and Δ_{ij} are Kroekner delta values, which are always equal to 0, unless i=h or j=h, for which they
686 are replaced by l. Next, the amount of movement is set by the step length, starting at step lengths
687 of 0.2, and decreases as stress decreases. Finally, starting at the step where **X** is normalized, this
688 process was repeated 20 times (but in other circumstances may be completed once the stability
689 criterion for stress is met). Stress values for k values of 1 through 6 were plotted against k for
690 both Q and R mode analyses. The number of dimensions chosen for analysis was determined
691 based on the point at which adding another dimension doesn't drastically change the stress (here,
692 2 dimensions) (McCune & Grace, 2005). The Q mode (analysis of samples by PAH
693 composition) NMDS ordinations were overlain with additional external variables relating to both
694 the variables themselves (PAHs) and samples.
695
696 Results from the Q mode NMDS (**Supplemental Figure S34**) demonstrate a separation of
697 samples from the Chicxulub impact crater (Site M0077) from distal sites (Sites 738 and 1262)
698 (**Supplemental Figure S35**). In the main text, we explain the separation between the three sites
699 as a function of transport processes (main text Figure 4) due to the distribution of PAHs along
700 NMDS1 by molecular weight and Site M0077's transport efficiency ratio values (51) and Site
701 1262 and 738's high transport ratio values. The dominant control on the data is transport, but not
702 timing (pre- syn- or post- boundary) (**Supplemental Figure S36**). Ring number, which is related
703 to size and thus transport, displays a control on NMDS1 (**Supplemental Figure S37**). The
704 number of alkylations of PAHs does not control the distribution on NMDS1, and has a minor
705 control on NMDS2 (**Supplemental Figure S38**). Similar to other transport-related variables, the
706 number of carbons controls the distribution on NMDS1, where the composition of PAHs at
707 Chicxulub is more dominated by compounds with more carbons (i.e. heavier and larger
708 molecules) than at distal sites (**Supplemental Figure S39**). The boiling point of specific
709 molecules had a control on their distribution along NMDS1 (**Supplemental Figure S40**), which
710 is a size and transport related parameter. NMDS1 is controlled by transport (solubility), as
711 observed in the log K_{ow} plot (**Supplemental Figure 41**), where higher logK_{ow} indicates less
712 soluble compounds, and lower logK_{ow} indicates more soluble compounds. Similar patterns are
713 observed for volatility using logK_{oa} (**Supplemental Figure S42**) and logK_{aw} (**Supplemental
714 Figure S43**), where more volatile PAH load positively on NMDS1 and are more associated with
715 the composition of distal sites, whereas less volatile PAHs load negatively on NMDS1 and are
716 associated with Chicxulub samples.
717
718 While these size and transport related differences can also be explained by biodegradation (i.e.
719 see the probability of linear degradation in **Supplemental Figure S44**), there is no correlation
720 with other markers of biodegradation that would be expected in the samples. For example, if
721 PAHs show biodegradation, biodegradation should also be witnessed in n-alkanes. One of the
722 ways to assess n-alkane biodegradation in a sample is the isoprenoid to alkane ratios pristane / n-
723 C_{17} and phytane / n-C_{18}. Linear alkanes biodegrade quicker than branched isoprenoids, meaning
724 that isoprenoid to n-alkane ratios would be higher in more biodegraded and lower in less
725 weathered or biodegraded samples. We observe no relationship between isoprenoid to alkane
726 biodegradation indices and sample spread on NMDS1 (**Supplemental Figure S45,
727 Supplemental Figure S46**). Thus, we conclude that transport, not biodegradation of PAHs,
728 which both would drive size-related effects on PAH distributions, is the major control on the
729 difference between PAH distributions at Chicxulub and distal sites.
730

6. Thermal maturity records of Sites M0077, 738, and 1262

Hopanoid measures of thermal maturity were recorded for Sites M0077 (**Supplemental Figure S47**), 1262 (**Supplemental Figure S48**), and 738 (**Supplemental Figure S49**). At all sites, Moretane / Moretane + Hopane ratios were assessed for C_{29} and C_{30} hopanoids. Moretane / Moretane + Hopane decreases as thermal maturity proceeds, as moretane is less thermally stable than the hopane form (53–55). The C_{29} Moretane / Moretane + Hopane value at the Chicxulub impact crater is 0.29 ± 0.12, at Site 1262 is 0.07 ± 0.04, and at Site 738 is 0.02 ± 0.03. The C_{30} Moretane / Moretane + Hopane value at Chicxulub is 0.31 ± 0.13, at Site 1262 is 0.06 ± 0.04, and at Site 738 is 0.03 ± 0.04. Based on Moretane / Moretane + Hopane ratios, it is evident that all sites are not past the oil window, as Moretane is still present, and the impact crater site is less thermally mature than the distal sites. Thermal maturity within the slumped interval at Chicxulub Site M0077 (2, 5) is less thermally mature than the surrounding sediments, indicating that the slumped interval may represent more modern or terrigenous input from outside of the crater. Additionally, this observation negates the hypothesis that hydrothermal fluid circulation within the crater sediments drove the observed "petrogenic" PAH signals.

S/R hopanoid isomerization is also a measure of thermal maturity, where the homohopane $S / S + R$ ratios increase with increasing thermal maturation, until full isomerization occurs, at which homohopane $S / S + R$ values reach 0.6, which occurs at temperatures of ~ 50 ºC. Even complete isomerization of the hopanoid $S / S + R$ values would indicate relatively low thermal maturity (53). The C_{31} homohopane $S / S + R$ ratio at Chicxulub is 0.48 ± 0.07, at Site 1262 is 0.55 ± 0.03, but was not calculated at Site 738 due to the low concentration of hopanoids. The C_{32} homohopane $S / S + R$ ratio at Chicxulub is 0.70 ± 0.14, at Site 1262 is 0.55 ± 0.09, but was not measured at Site 738 due to low hopanoid concentrations. At Chicxulub Site M0077, lower thermal maturity based on the C_{31} homohopane $S / S + R$ ratio is observed within the slumped unit (2, 5).

In addition, we measured the C_{35} homohopane index for Sites M0077 and 1262. The C_{35} homohopane index is a thermal maturity index, but it can also be interpreted as a redox indicator (53). The C_{35} homohopane index is determined by the sum of *S* and *R* isomers of the C_{35} homohopane divided by all (C_{31-35}) homohopanes. The C_{35} homohopane index reaches values of 0.01 ± 0.02 at Chicxulub and 0.05 ± 0.04 at Site 1262. If interpreted as a maturity marker, the C_{35} homohopane index represents relatively low maturity at both sites. The C_{35} homohopane index was not measured at Site 738 due to the low concentration of hopanoids.

Additionally, the Norhopane / Norhopane + Hopane and $T_s / T_s + T_m$ ratios were calculated. Both ratios increase with increasing thermal maturity. The Norhopane / Norhopane + Hopane ratio reached values of 0.78 ± 0.19 at Chicxulub, 0.91 ± 0.10 at Site 1262, and 0.77 ± 0.16 at Site 738. The $T_s / T_s + T_m$ ratio reached values of 0.47 ± 0.17 at Chicxulub, 0.57 ± 0.16 at Site 1262, and 0.79 ± 0.22 at Site 738. Based on all of the thermal maturity parameters, Site M0077 at the Chicxulub impact crater is less thermally mature than the distal K-Pg sites. Interestingly, lower thermal maturity according to the $T_s / T_s + T_m$ and Norhopane / Norhopane + Hopane indices is not observed in the slumped interval at Chicxulub. We interpret this discrepancy as the influence of environmental factors on both the $T_s / T_s + T_m$ and Norhopane / Norhopane + Hopane ratio,

776   including depositional environment, terrigenous influence, and redox conditions that may have
777   overprinted or altered the otherwise thermal maturity signals.
778
779   Finally, we demonstrate low Hydrogen Index values at Site M0077 measured via Weatherford
780   Source Rock Analyzer (**Supplemental Figure S50**). Low hydrogen index values can represent
781   thermally mature organic matter, or coupled with high Oxygen Index values, can indicate
782   terrigenous or inert organics. We suggest presence of low Hydrogen Indices at Site M0077
783   suggest a thermally altered source of organics.
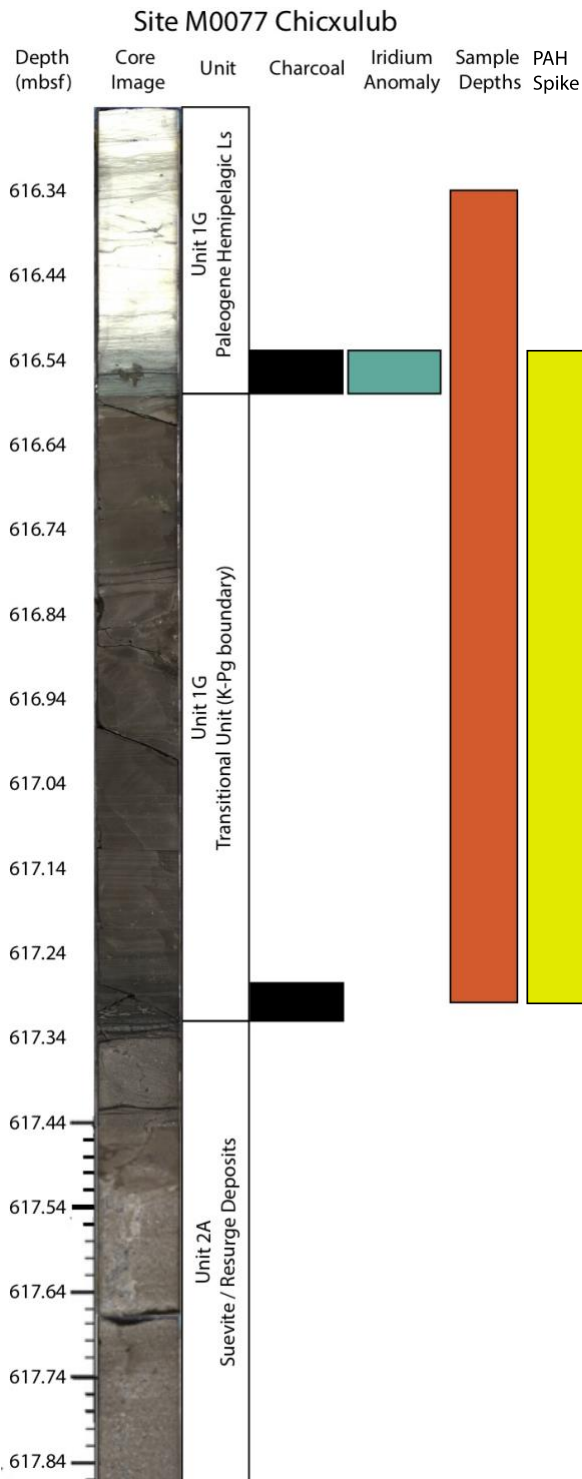
784
785 **Supplemental Figure S1.** Stratigraphy and samples evaluated for PAH composition at Site
786 M0077 (Chicxulub). The core image (Gulick *et al*., 2019), depths, and depositional unit (Lowery
787 *et* al., 2018) are displayed, demonstrating the K-Pg boundary clay. Depths with abundant
788 charcoal are shown in black (Gulick *et al*., 2019), the iridium anomaly is displayed in teal,
789 sample depths analyzed for PAHs are displayed in orange, and the elevated PAH interval is
790 displayed in yellow.
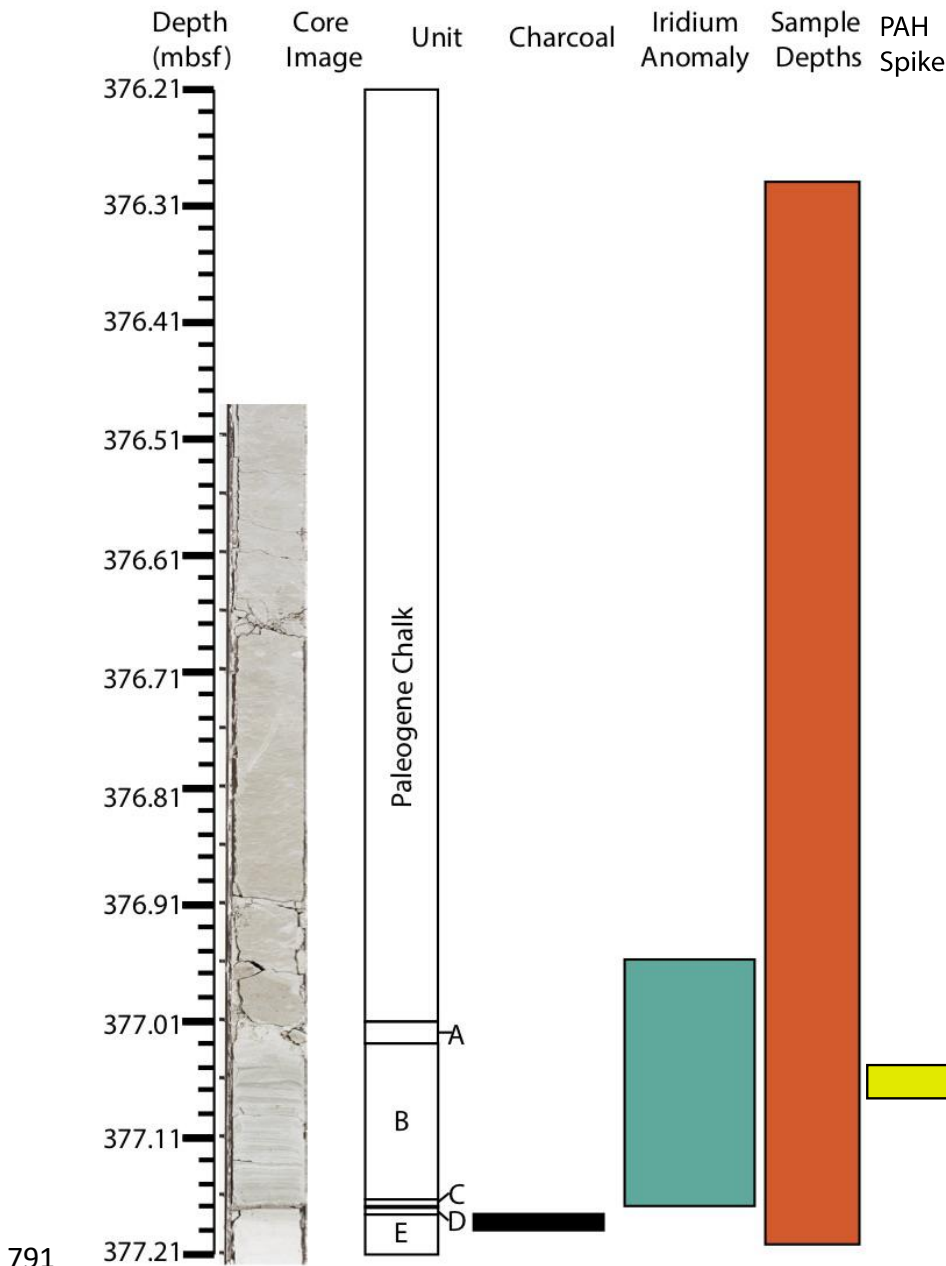
791
792
793 **Supplemental Figure S2.** Stratigraphy and samples evaluated for PAH composition at Site 738
794 (Kerguelen Plateau). The core image, depths, and depositional unit (6) are displayed,
795 demonstrating the K-Pg boundary clay. Depths with abundant charcoal are shown in black (4),
796 the iridium anomaly is displayed in teal, sample depths analyzed for PAHs are displayed in
797 orange, and the elevated PAH interval is displayed in yellow. Units A through E represent the K-
798 Pg boundary unit, including the bioturbated light brown to white chalk (unit A), thesemi-
799 indurated, finely laminated white and green clay layers (unit B), the 3 mm thick K-Pg boundary
800 green clay layer (unit C), the laminated chalk (unit D), and the white, bioturbated limestone (unit
801 E).
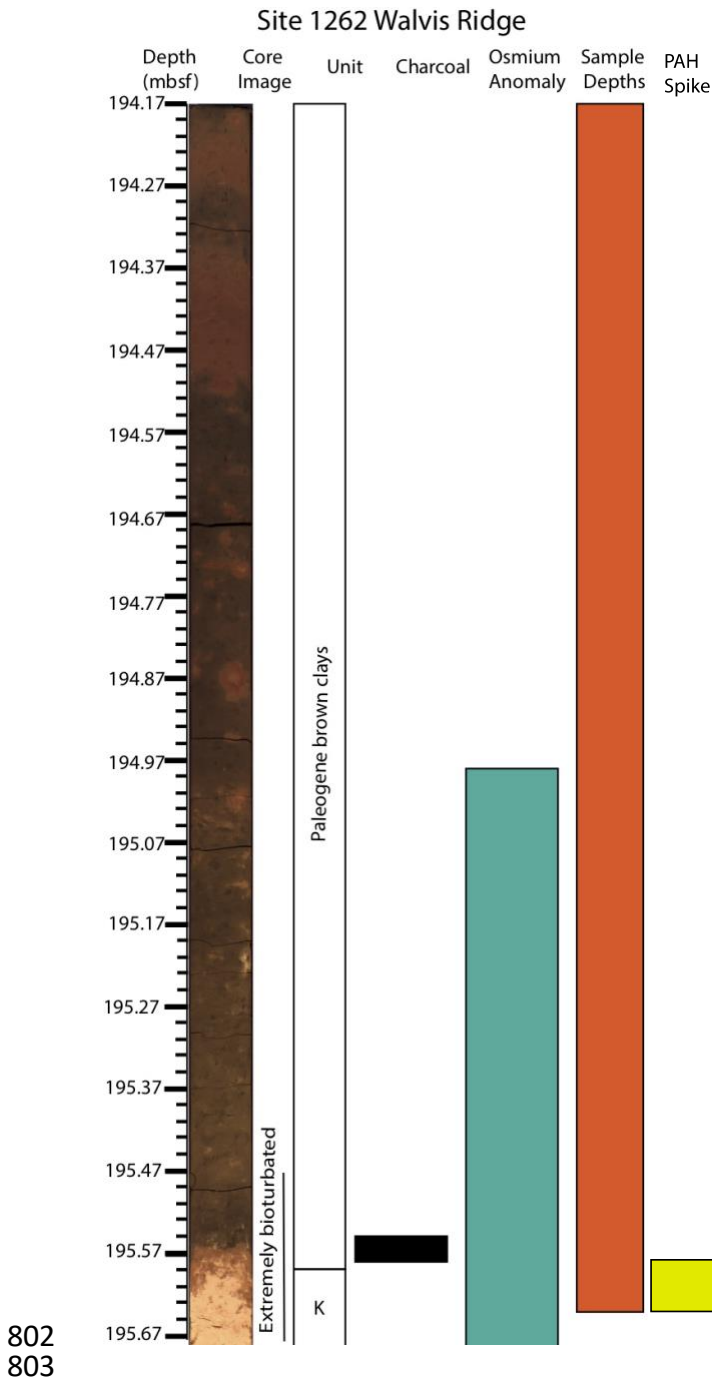
Supplemental Figure S3. Stratigraphy and samples evaluated for PAH composition at Site 1262 (Walvis Ridge). The core depths and depositional unit (7) are displayed, demonstrating the K-Pg boundary clay. Depths with abundant charcoal are shown in black (4), the Osmium isotope anomaly is displayed in teal, sample depths analyzed for PAHs are displayed in orange, and the elevated PAH interval is displayed in yellow.. The iridium anomaly has not been measured for this site. The K-Pg boundary interval is extremely bioturbated (7) and grades from the tan – light pink clay rich Cretaceous ooze (unit K) to the brown Paleocene clays (7). The boundary layer is identified as 195.59 mbsf, though the true K-Pg record is smeared for ~10's of cm due to bioturbation.
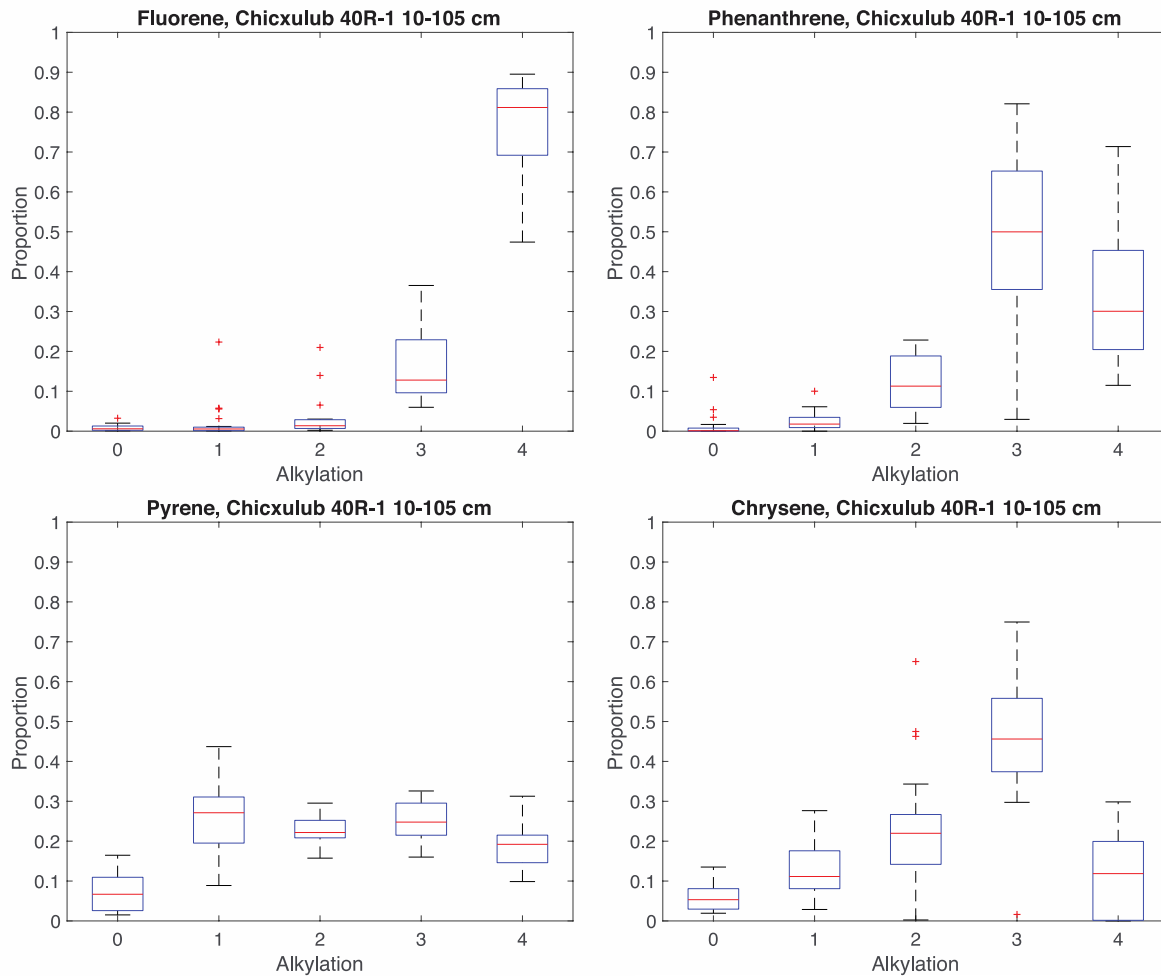
813
814 **Supplemental Figure S4.** Alkylation patterns of homologous series of PAHs from Chicxulub
815 Site M0077demonstrate a propensity for more alkylated over parent forms. Box and whisker
816 plots show the spread of data for the proportion of 0-4 alkylated PAHs relative to the sum of 0-4
817 alkylated PAHs for each homologous series. Red lines mark the median, the blue box groups the
818 25_{th} and 75_{th} percentiles, Black lines extend to the full range of the data, outliers are marked by
819 red + symbols. Fluorene pattern is consistent with a weathering signal (56), whereas
820 phenanthrene, pyrene, and chrysene patterns are more consistent with a petrogenic source. No
821 PAH alkylation patterns are indicative of a strictly biomass burning source.
822

Chicxulub Site M0077 PAH Concentrations
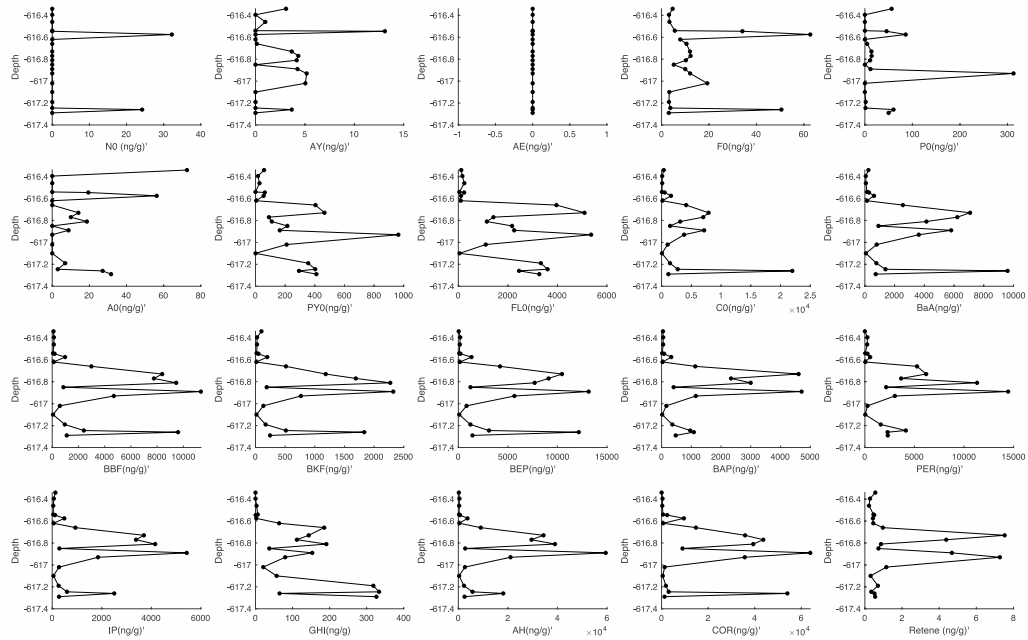
Supplemental Figure S5. Concentration of parent PAHs relative to dry rock versus depth (mbsf) at Chicxulub. All PAH concentrations were calculated relative to a 5 point standard curve. Curves are shown for Naphthalene (N0), Acenaphthylene (AY), Acenaphthene (AE), Fluorene (F0), Phenanthrene (P0), Anthracene (A0), Pyrene (PY0), Fluoranthene (FL0), Chrysene (C0), Benz[a]anthracene (BaA), Benzo[b]fluoranthene (BBF), Benzo[k]fluoranthene (BKF), Benzo[e]pyrene (BEP), Benzo[a]pyrene (BAP), Perylene (PER), Indeno[1,2,3-cd]pyrene (IP), Benzo[ghi]perylene (GHI), Dibenz[ah]anthracene (AH), Coronene (COR), and Retene (RET). PAH concentrations relative to rock are highest within the boundary layer (below 616.58 mbsf) and concentrations of larger PAHs are typically greater than smaller PAHs.

Site 738 Kerguelen Plateau PAH Concentrations
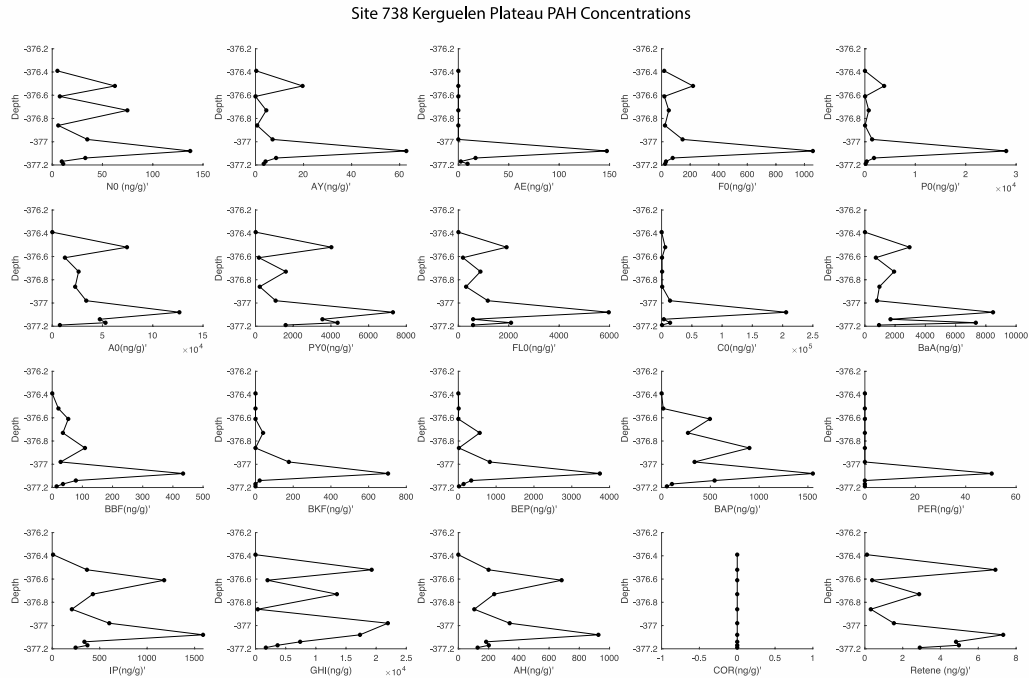
Supplemental Figure S6. Concentration of parent PAHs relative to dry rock versus depth (mbsf) at Kerguelen Plateau Site 738. All PAH concentrations were calculated relative to a 5 point standard curve. Curves are shown for Naphthalene (N0), Acenaphthylene (AY), Acenaphthene (AE), Fluorene (F0), Phenanthrene (P0), Anthracene (A0), Pyrene (PY0), Fluoranthene (FL0), Chrysene (C0), Benz[a]anthracene (BaA), Benzo[b]fluoranthene (BBF), Benzo[k]fluoranthene (BKF), Benzo[e]pyrene (BEP), Benzo[a]pyrene (BAP), Perylene (PER), Indeno[1,2,3-cd]pyrene (IP), Benzo[ghi]perylene (GHI), Dibenz[ah]anthracene (AH), Coronene (COR), and Retene (RET). PAH concentrations for most species are highest at 377.08 mbsf, within the K-Pg impact-related deposit.

Site 738 Kerguelen Plateau
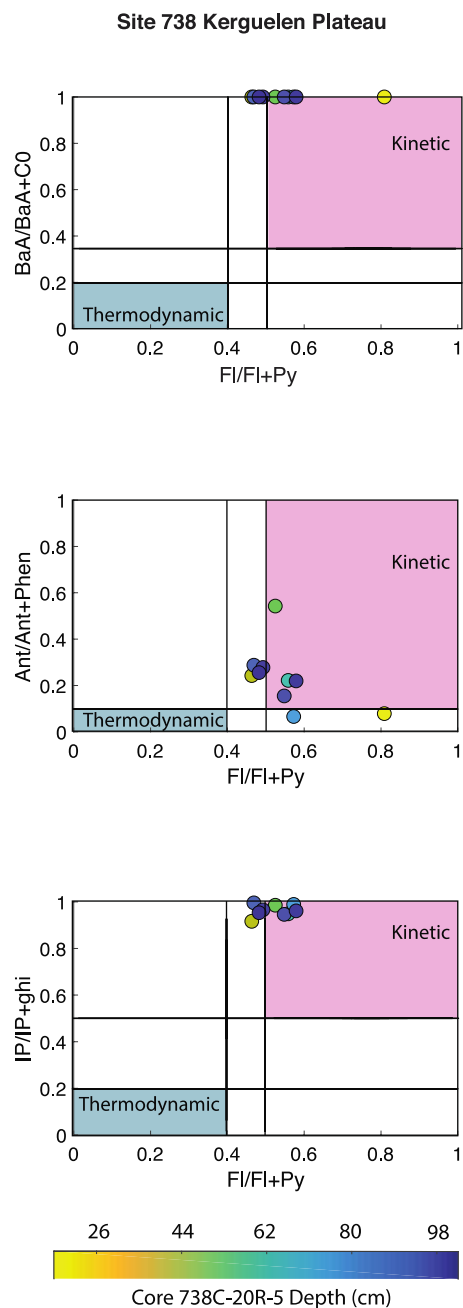
846 **Supplemental Figure S7**. PAH ratios at Site 738 are dominated by kinetic isomers. Three
847 kinetic / (kinetic + thermodynamic) isomer ratio biplots with kinetic-source and thermodynamic
848 source cutoffs indicated by solid black lines. Pink quadrants represent kinetically favored PAH
849 ratios, blue quadrants represent thermodynamically favored PAH ratios, and white space
850 indicates mixed kinetic and thermodynamic sources. Samples from Site 738 are colored by depth
851 in Core 738C-20R-5. Observational cutoff values from Rocha & Palma (2019): Fl/Fl+Py:
852 thermodynamic < 0.4, kinetic > 0.5; BaA/BaA+C0: thermodynamic < 0.2, kinetic > 0.35;
853 Ant/Ant+Phen: thermodynamic < 0.1, kinetic >0.1; IP/IP+ghi: thermodynamic < 0.2, kinetic >
854 0.5. PAH abbreviations: Fl: Fluoranthene, Py : Pyrene; BaA: Benz[a]anthrance; C0 : Chrysene;
855 Ant: Anthracene; Phen: Phenanthrene; IP: Indeno[1,2,3-c,d]pyrene; ghi: Benzo[ghi]perylene
856 (56). Plot modified from Rocha & Palma, 2019.

857

Site 1262 Walvis Ridge PAH Concentrations
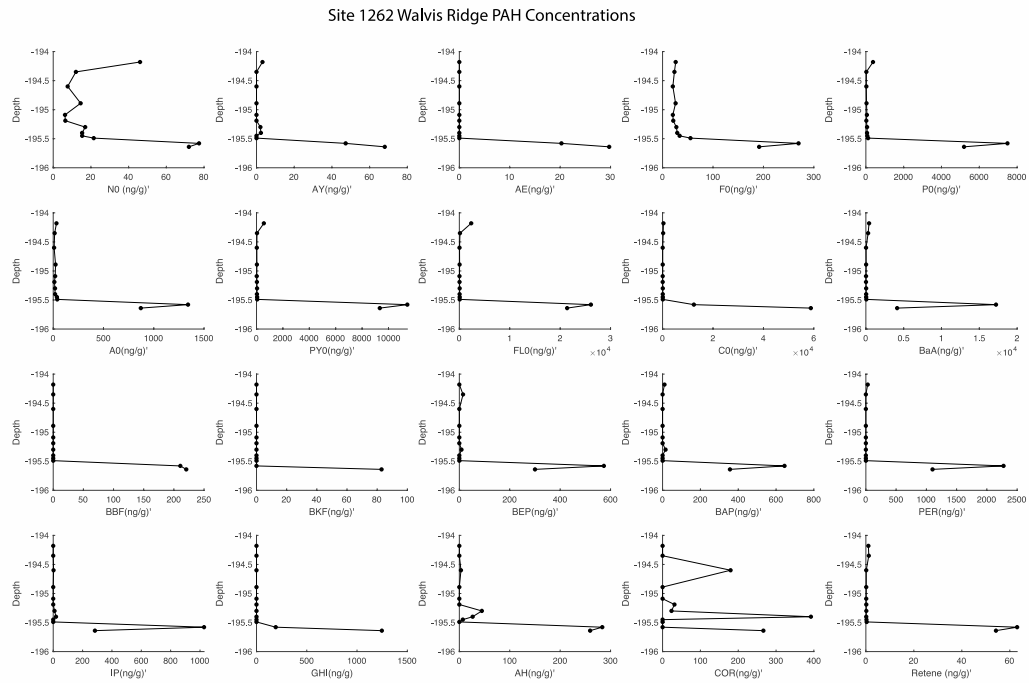
858
859 **Supplemental Figure S8.** Concentration of parent PAHs relative to dry rock versus depth (mbsf)
860 at Walvis Ridge Site 1262. All PAH concentrations were calculated relative to a 5 point standard
861 curve. Curves are shown for Naphthalene (N0), Acenaphthylene (AY), Acenaphthene (AE),
862 Fluorene (F0), Phenanthrene (P0), Anthracene (A0), Pyrene (PY0), Fluoranthene (FL0),
863 Chrysene (C0), Benz[a]anthracene (BaA), Benzo[b]fluoranthene (BBF), Benzo[k]fluoranthene
864 (BKF), Benzo[e]pyrene (BEP), Benzo[a]pyrene (BAP), Perylene (PER), Indeno[1,2,3-cd]pyrene
865 (IP), Benzo[ghi]perylene (GHI), Dibenz[ah]anthracene (AH), Coronene (COR), and Retene
866 (RET). PAH concentrations are highest between 195.58 – 195.64 mbsf, within the K-Pg impact-
867 related deposit.
868

Site 1262 Walvis Ridge

Core 1262B-22H-4 Depth (cm)
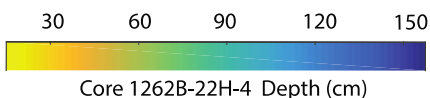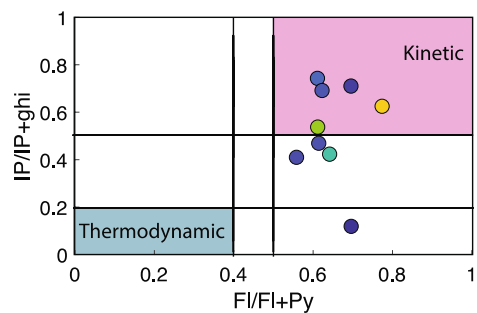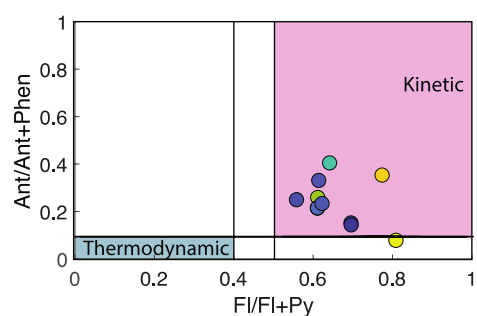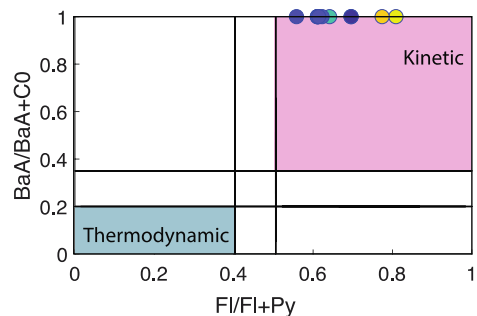
Supplemental Figure S9. PAH ratios at Site 1262 are dominated by kinetic isomers. Three kinetic / (kinetic + thermodynamic) isomer ratio biplots with kinetic-source and thermodynamic source cutoffs indicated by solid black lines. Pink quadrants represent kinetically favored PAH ratios, blue quadrants represent thermodynamically favored PAH ratios, and white space indicates mixed kinetic and thermodynamic sources. Samples from Site 1262 are colored by depth in Core 1262B-22H-5. Observational cutoff values from Rocha & Palma (2019): Fl/Fl+Py: thermodynamic < 0.4, kinetic > 0.5; BaA/BaA+C0: thermodynamic < 0.2, kinetic > 0.35; Ant/Ant+Phen: thermodynamic < 0.1, kinetic >0.1; IP/IP+ghi: thermodynamic < 0.2, kinetic > 0.5. PAH abbreviations: Fl: Fluoranthene, Py : Pyrene; BaA: Benz[a]anthrance; C0 : Chrysene; Ant: Anthracene; Phen: Phenanthrene; IP: Indeno[1,2,3-c,d]pyrene; ghi: Benzo[ghi]perylene (56). Plot modified from Rocha & Palma, 2019.
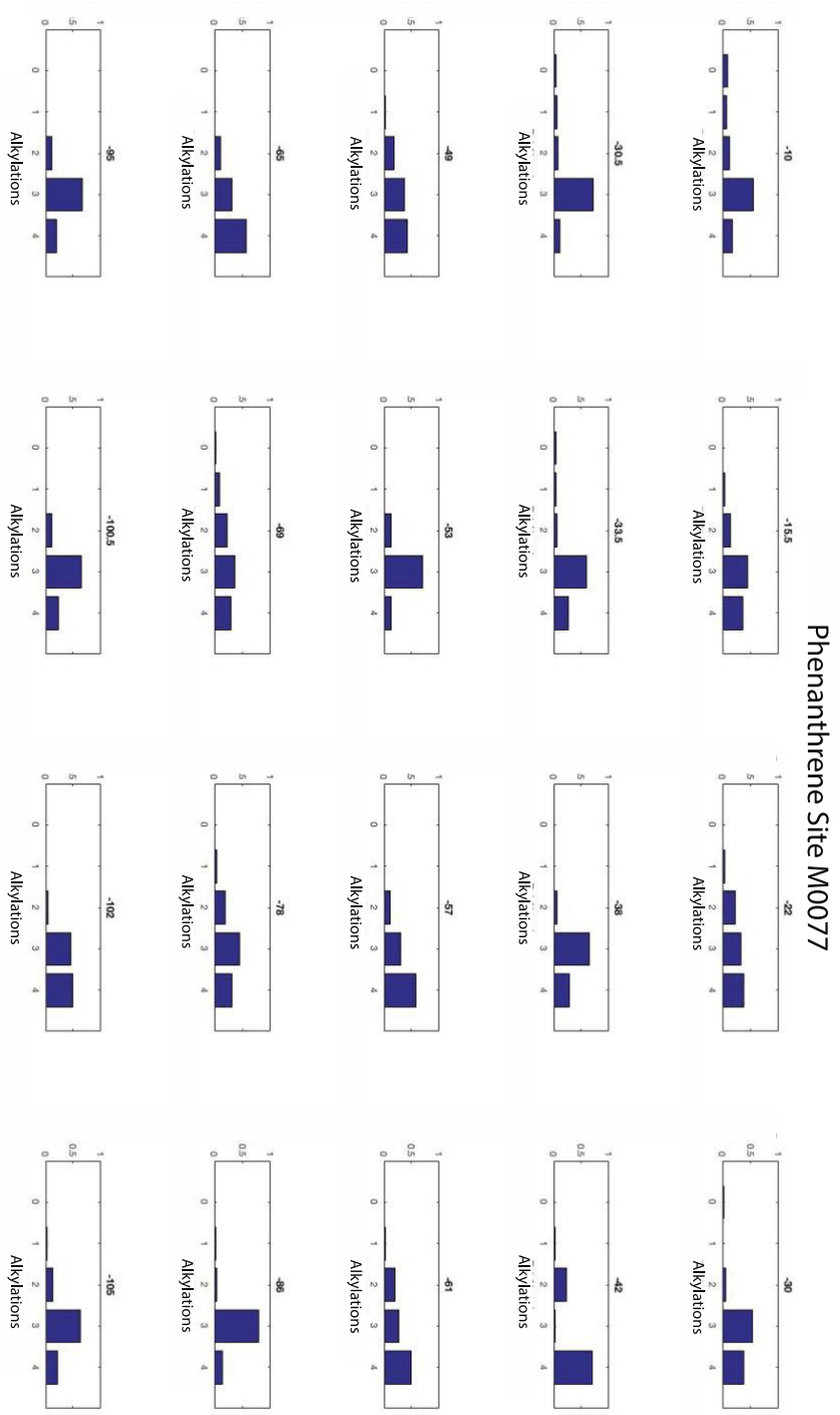
881
882
883 **Supplemental Figure S10.** Relative abundances of alkylated phenanthrenes from Site M0077
884 within the Chicxulub impact crater demonstrate a heightened abundance of alkylated
885 phenanthrenes relative to the non-alkylated parent form. Most profiles are consistent with a
886 petrogenic or weathered source. Numbers on the x-axis represent the number of methylations,
887 and the y-axis is the relative abundance of each compound relative to the sum of 0-4 alkylated
888 isomers. Numbers at the top of each plot represent the depth in Section 0077-40R-1.
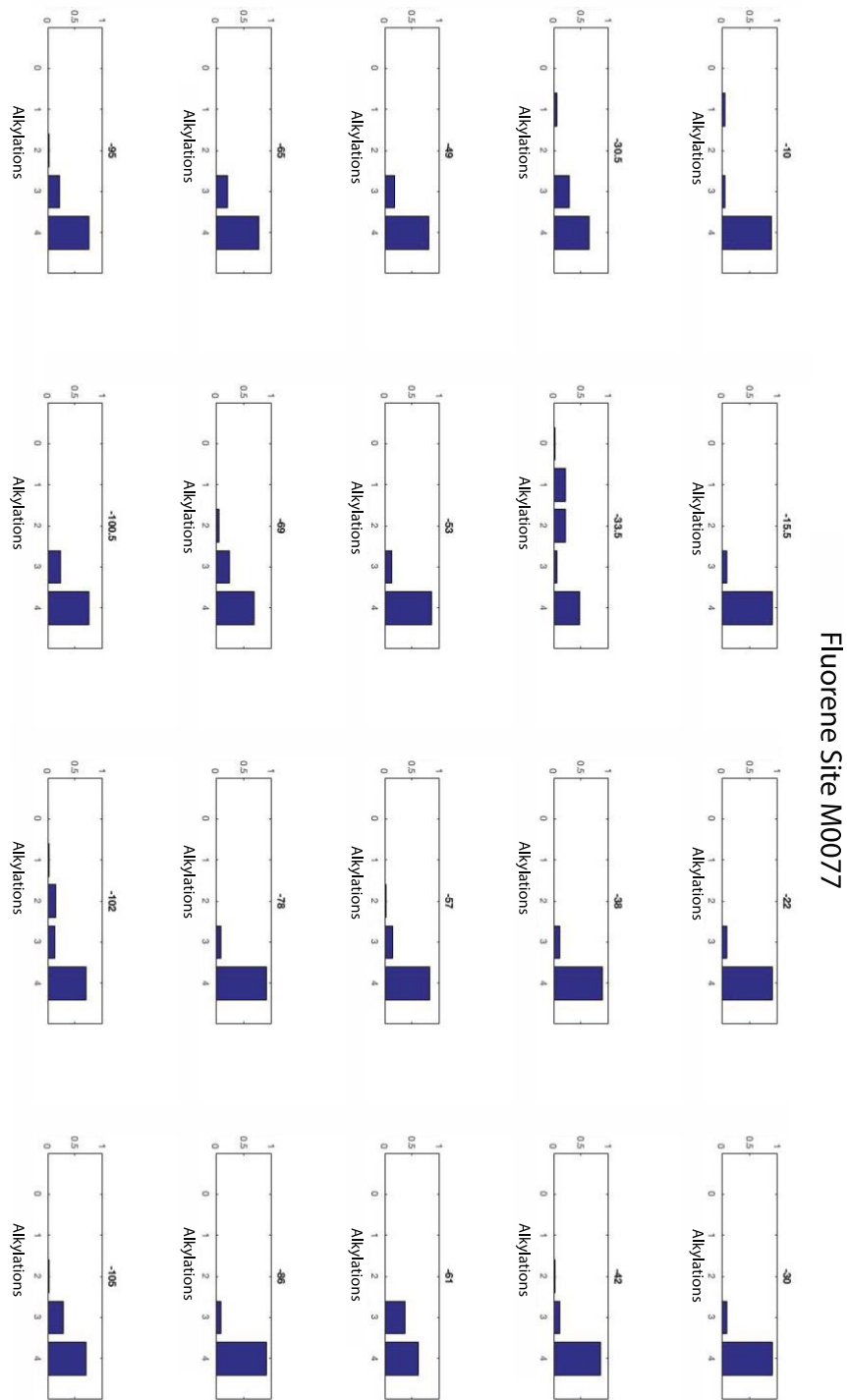
Fluorene Site M0077

889
Supplemental Figure S11. Relative abundances of alkylated fluorenes from Site M0077 within
the Chicxulub impact crater demonstrate a heightened abundance of alkylated fluorenes relative
to the non-alkylated parent form. All profiles are consistent with a weathered source. Numbers
on the x-axis represent the number of methylations, and the y-axis is the relative abundance of
each compound relative to the sum of 0-4 alkylated isomers. Numbers at the top of each plot
represent the depth in Section 0077-40R-1.
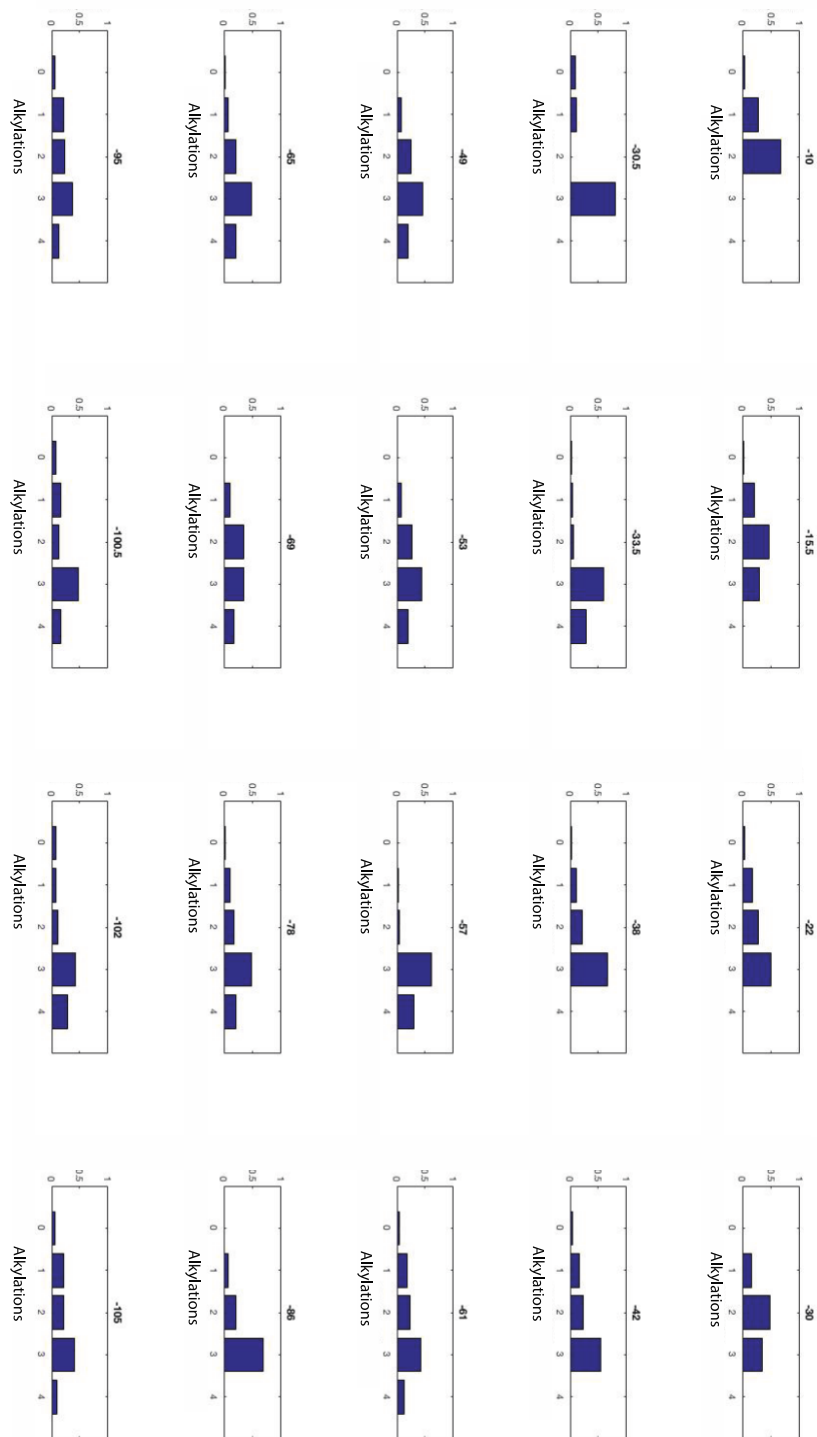
896
897 **Supplemental Figure S12.** Relative abundances of alkylated chrysenes from Site M0077 within
898 the Chicxulub impact crater demonstrate a heightened abundance of alkylated chrysenes relative
899 to the non-alkylated parent form. Most profiles are consistent with a petrogenic source. Numbers
900 on the x-axis represent the number of methylations, and the y-axis is the relative abundance of
901 each compound relative to the sum of 0-4 alkylated isomers. Numbers at the top of each plot
902 represent the depth in Section 0077-40R-1.
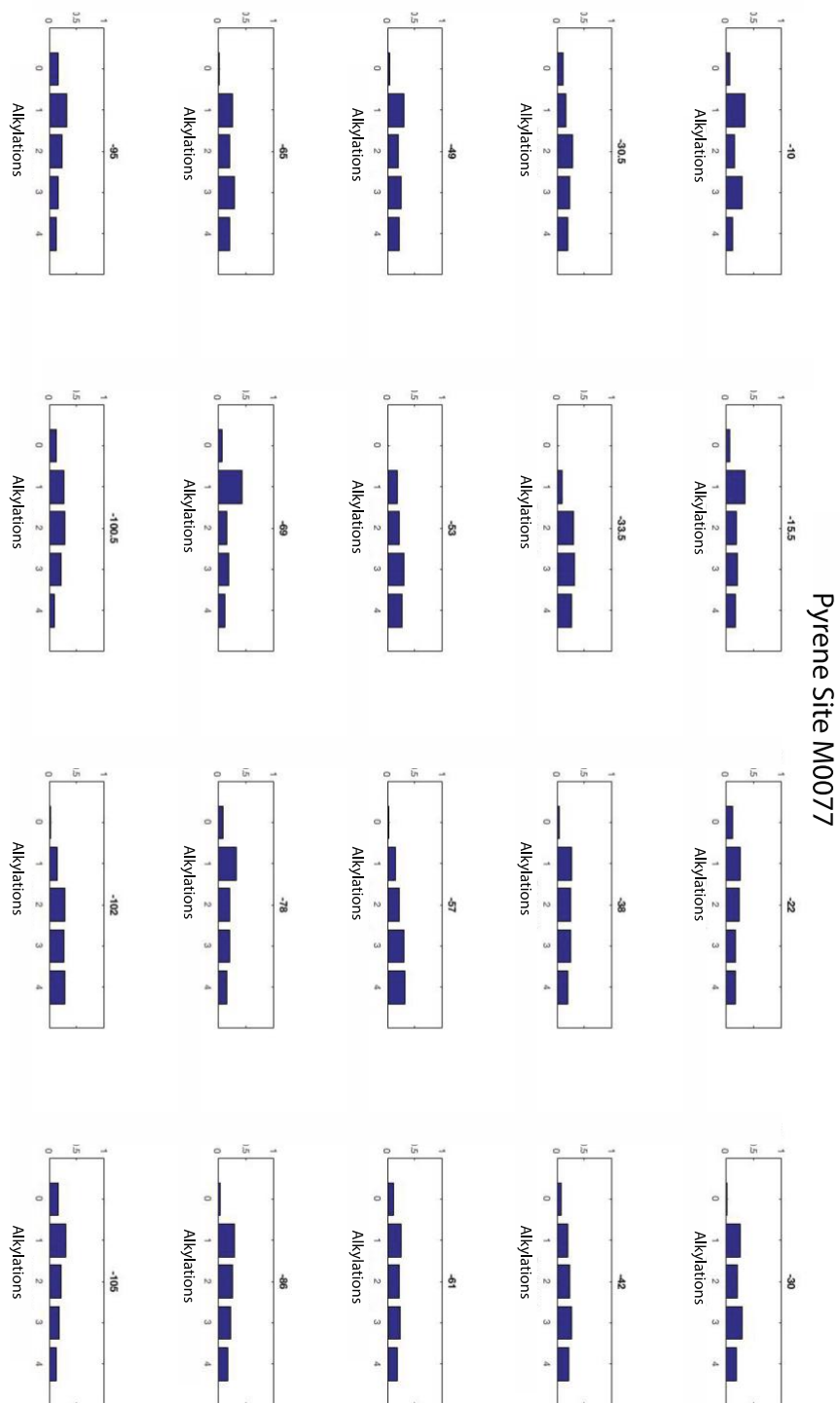
Pyrene Site M0077

903
Supplemental Figure S13. Relative abundances of alkylated pyrenes from Site M0077 within
the Chicxulub impact crater demonstrate a heightened abundance of alkylated pyrenes relative to
the non-alkylated parent form. Most signatures are consistent with a petrogenic, and likely
weathered, source. Numbers on the x-axis represent the number of methylations, and the y-axis
is the relative abundance of each compound relative to the sum of 0-4 alkylated isomers.
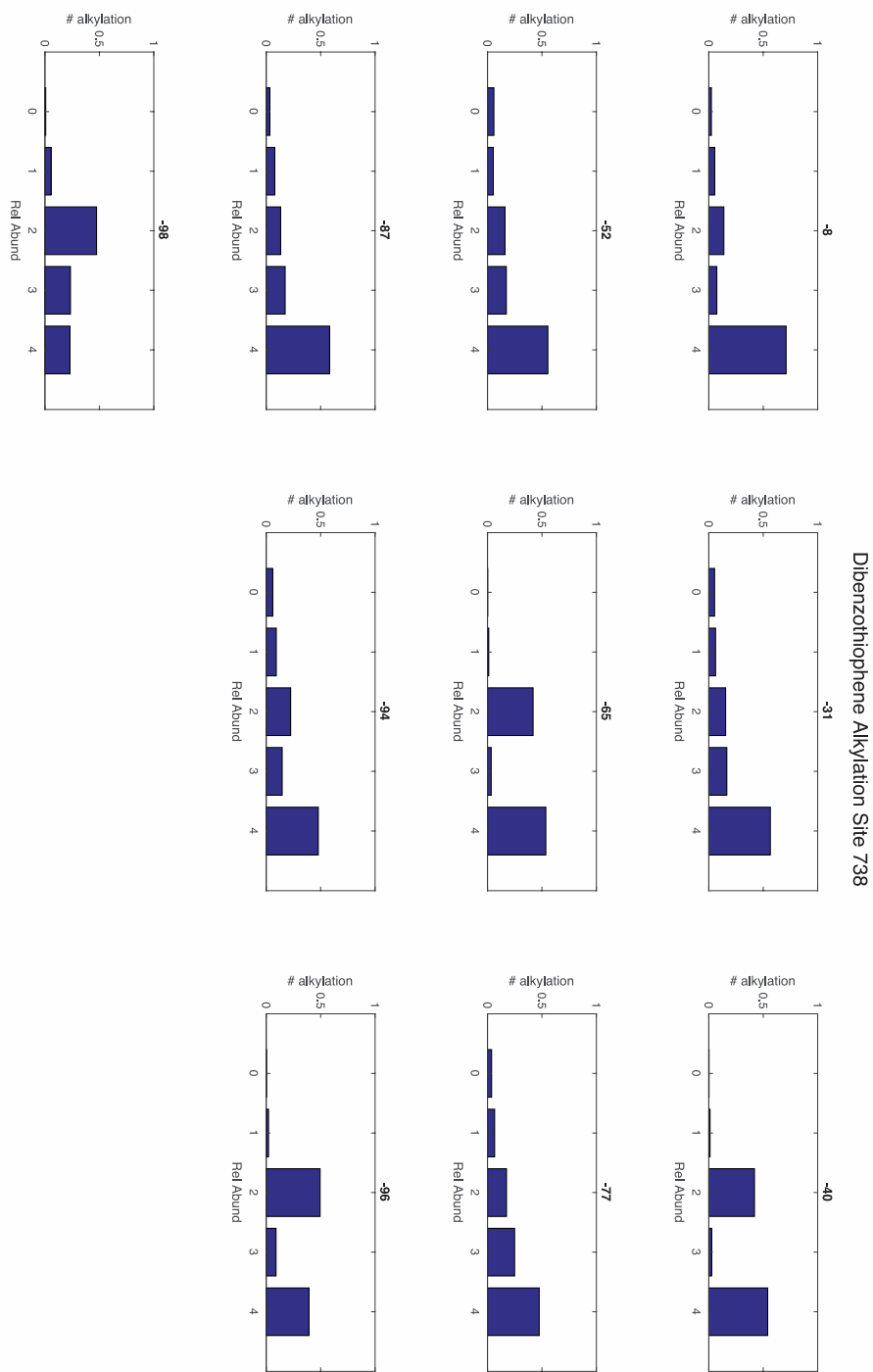Numbers at the top of each plot represent the depth in Section 0077-40R-1.
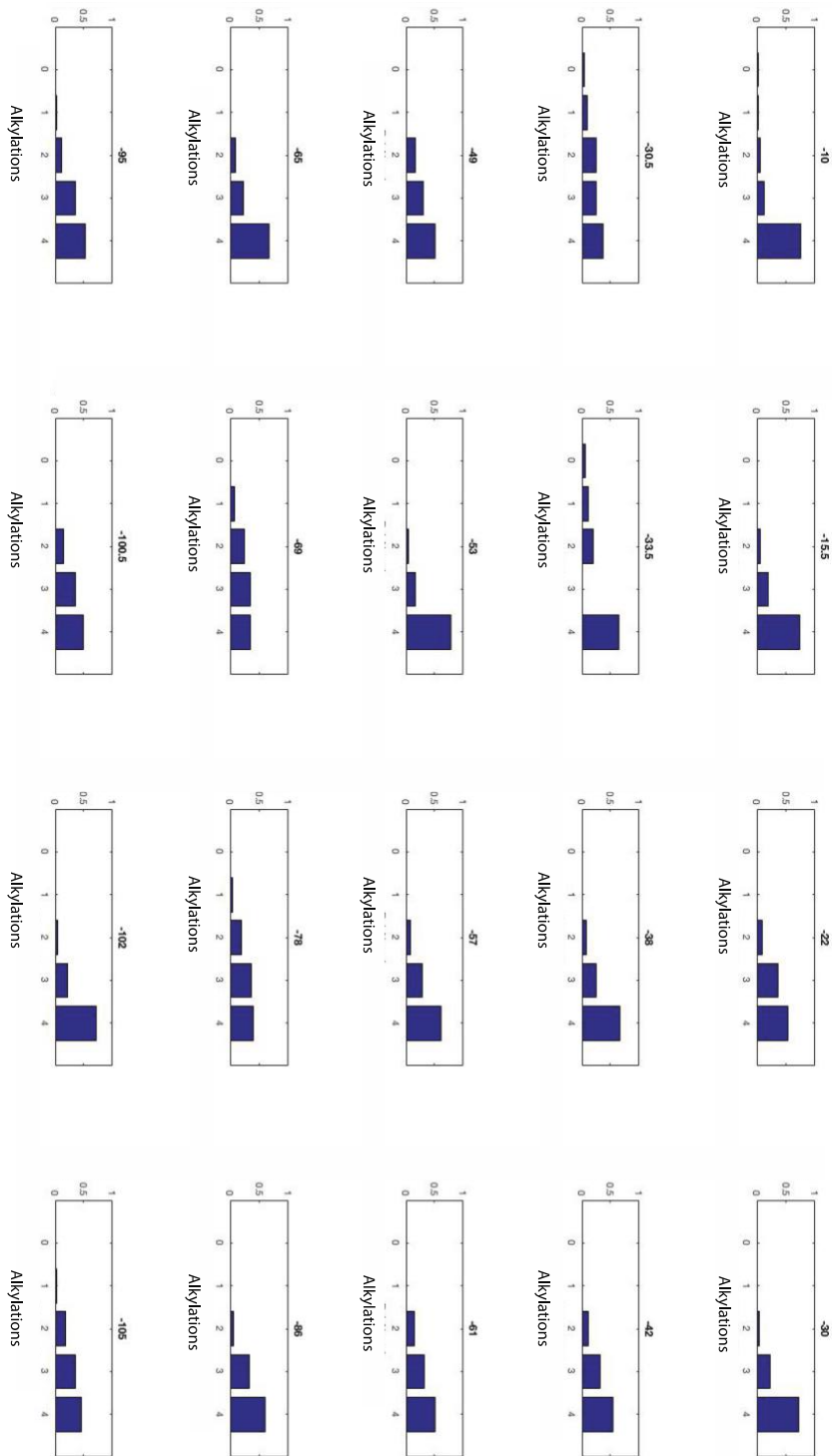
910
Supplemental Figure S14. Relative abundances of alkylated dibenzothiophenes from Site
M0077 within the Chicxulub impact crater demonstrate a heightened abundance of alkylated
dibenzothiophenes relative to the non-alkylated parent form. Profiles represent a weathered
signature. Numbers on the x-axis represent the number of methylations, and the y-axis is the
relative abundance of each compound relative to the sum of 0-4 alkylated isomers. Numbers at
the top of each plot represent the depth in Section 0077-40R-1.

Site M0077 APDI Pyrene
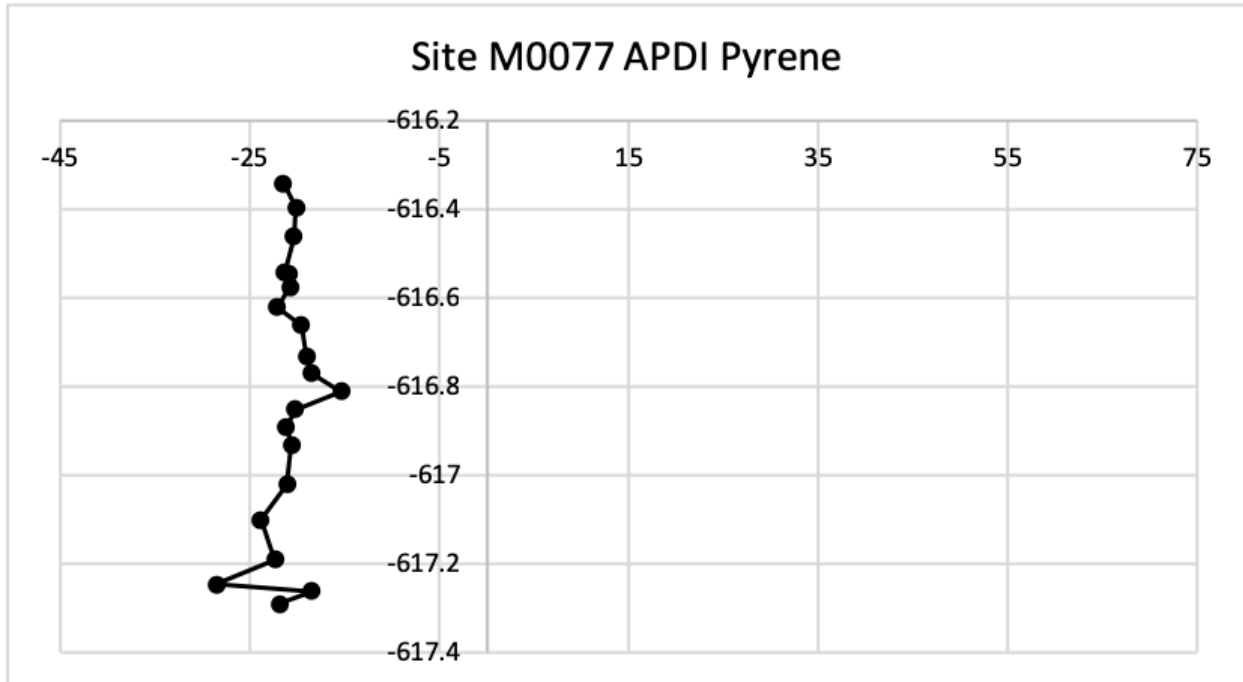
917
918
919 **Supplemental Figure S15.** The Alkylated PAH Distribution Index (51) based on the
920 homologous series of pyrenes presents negative, "petrogenic" source values at Chicxulub. The y-
921 axis represents depth (mbsf) at Site M0077, and the y-axis is the Pyrene APDI. Negative values
922 indicate a petrogenic source, positive values indicate a pyrogenic source, and values near 0
923 represent mixed or undiscernible sources.
924
925
926
927

Site M0077 APDI Chrysene

928
929
930 **Supplemental Figure S16.** The Alkylated PAH Distribution Index (51) based on the
931 homologous series of chrysenes presents negative, "petrogenic" source values at Chicxulub. The
932 y-axis represents depth (mbsf) at Site M0077, and the y-axis is the Chrysene APDI. Negative
933 values indicate a petrogenic source, positive values indicate a pyrogenic source, and values near
934 0 represent mixed or undiscernible sources.
935
936
937
938
939

Site M0077 APDI Phenanthrene
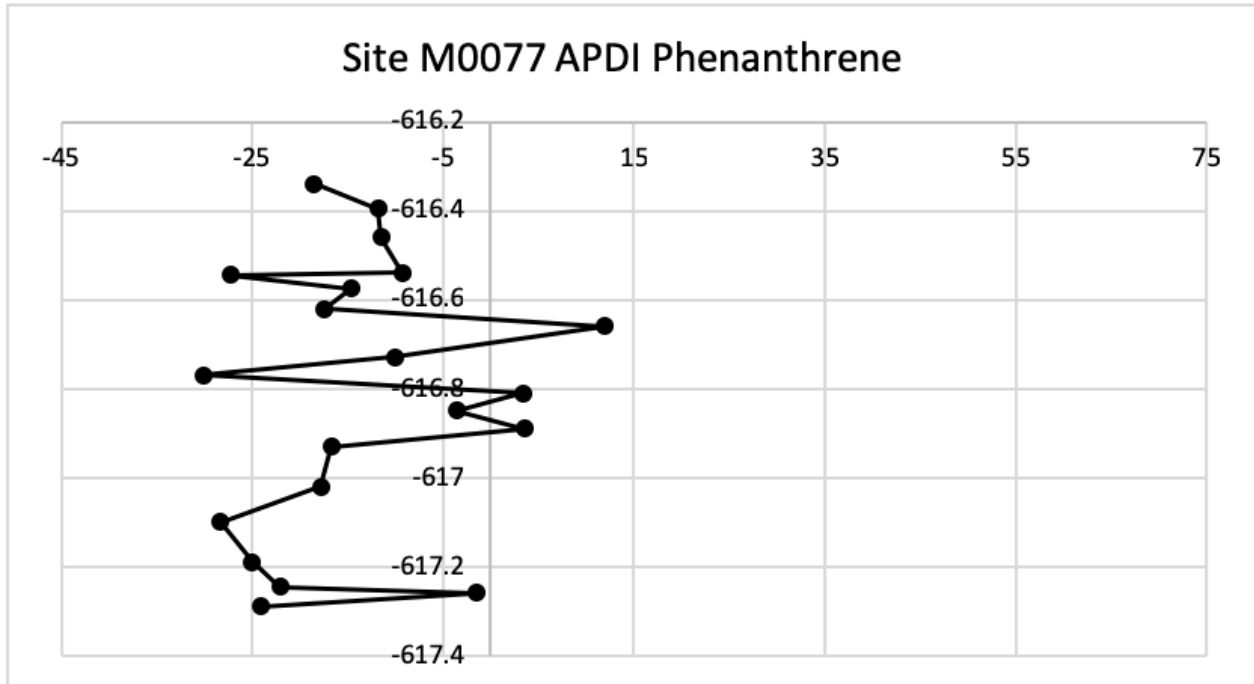
940
941
942   **Supplemental Figure S17.** The Alkylated PAH Distribution Index (51) based on the
943   homologous series of phenanthrenes presents negative, "petrogenic" source values to near-zero,
944   mixed source values at Chicxulub. The y-axis represents depth (mbsf) at Site M0077, and the y-
945   axis is the Phenanthrene APDI. Negative values indicate a petrogenic source, positive values
946   indicate a pyrogenic source, and values near 0 represent mixed or undiscernible sources. We
947   suggest the highly variable data is a result of the low concentration of phenanthrenes at Site
948   M0077.
949
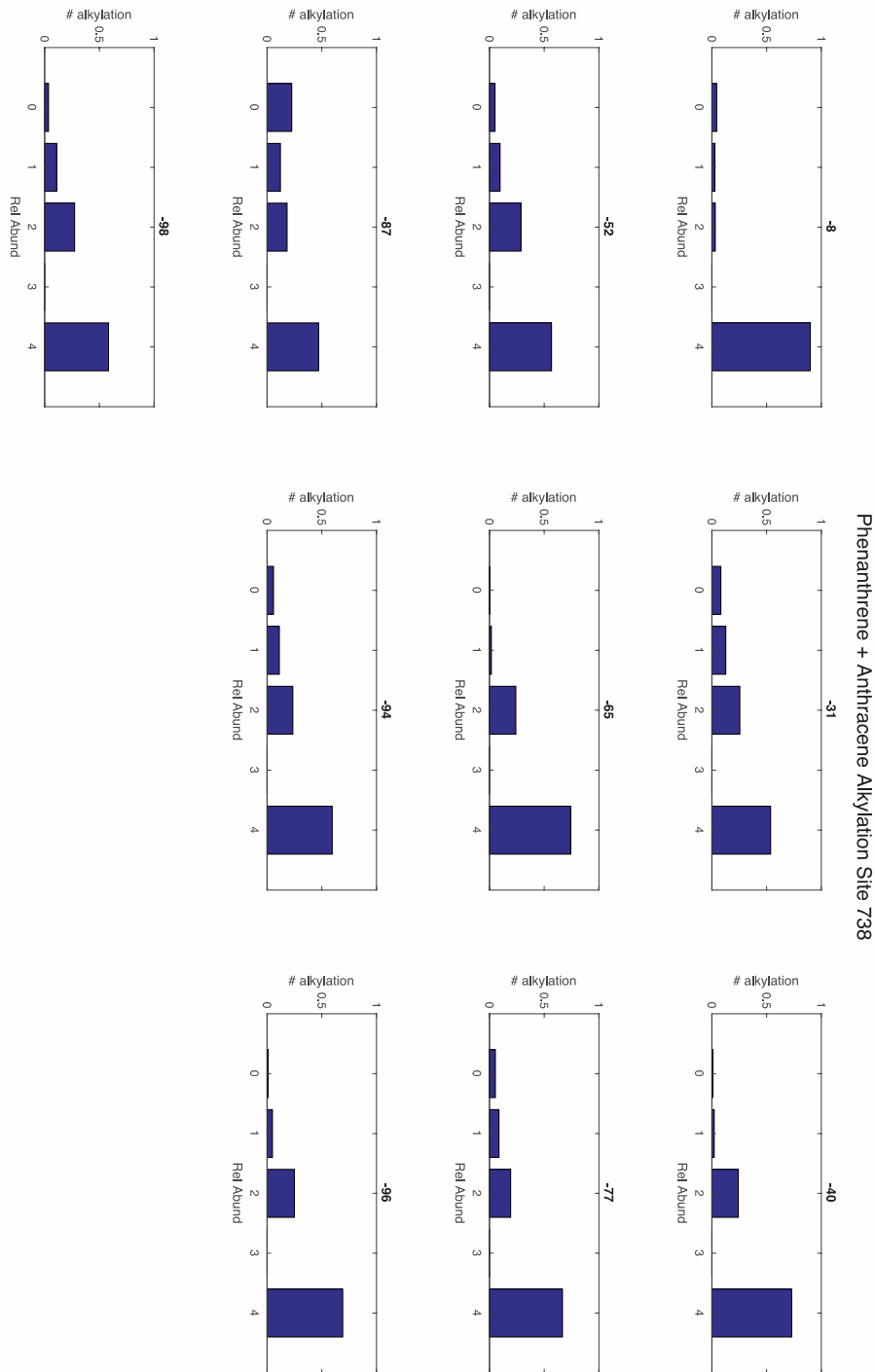
950
951 **Supplemental Figure S18.** Relative abundances of alkylated phenanthrenes from Site 738 at
952 Kerguelen Plateau demonstrate a heightened abundance of alkylated phenanthrenes relative to
953 the non-alkylated parent form. Most signatures are consistent with a weathered, source. Numbers
954 on the x-axis represent the number of methylations, and the y-axis is the relative abundance of
955 each compound relative to the sum of 0-4 alkylated isomers. Numbers at the top of each plot
956 represent the depth in Section 738C-20R-5.

957
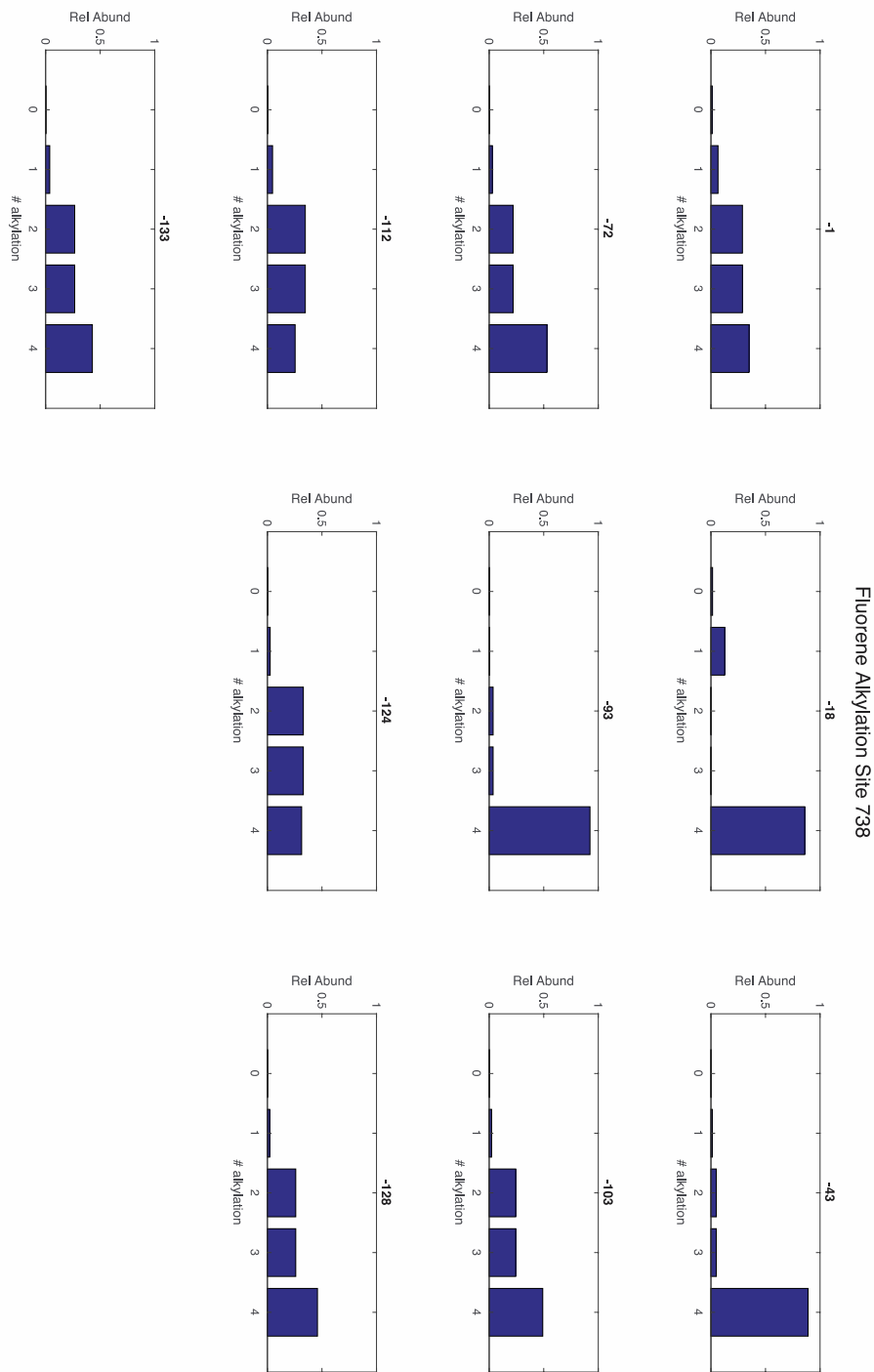
Supplemental Figure S19. Relative abundances of alkylated fluorenes from Site 738 at
Kerguelen Plateau demonstrate a heightened abundance of alkylated fluorenes relative to the
non-alkylated parent form. Most signatures are consistent with a weathered petrogenic, source.
Numbers on the x-axis represent the number of methylations, and the y-axis is the relative
abundance of each compound relative to the sum of 0-4 alkylated isomers. Numbers at the top of
each plot represent the depth in Section 738C-20R-5.
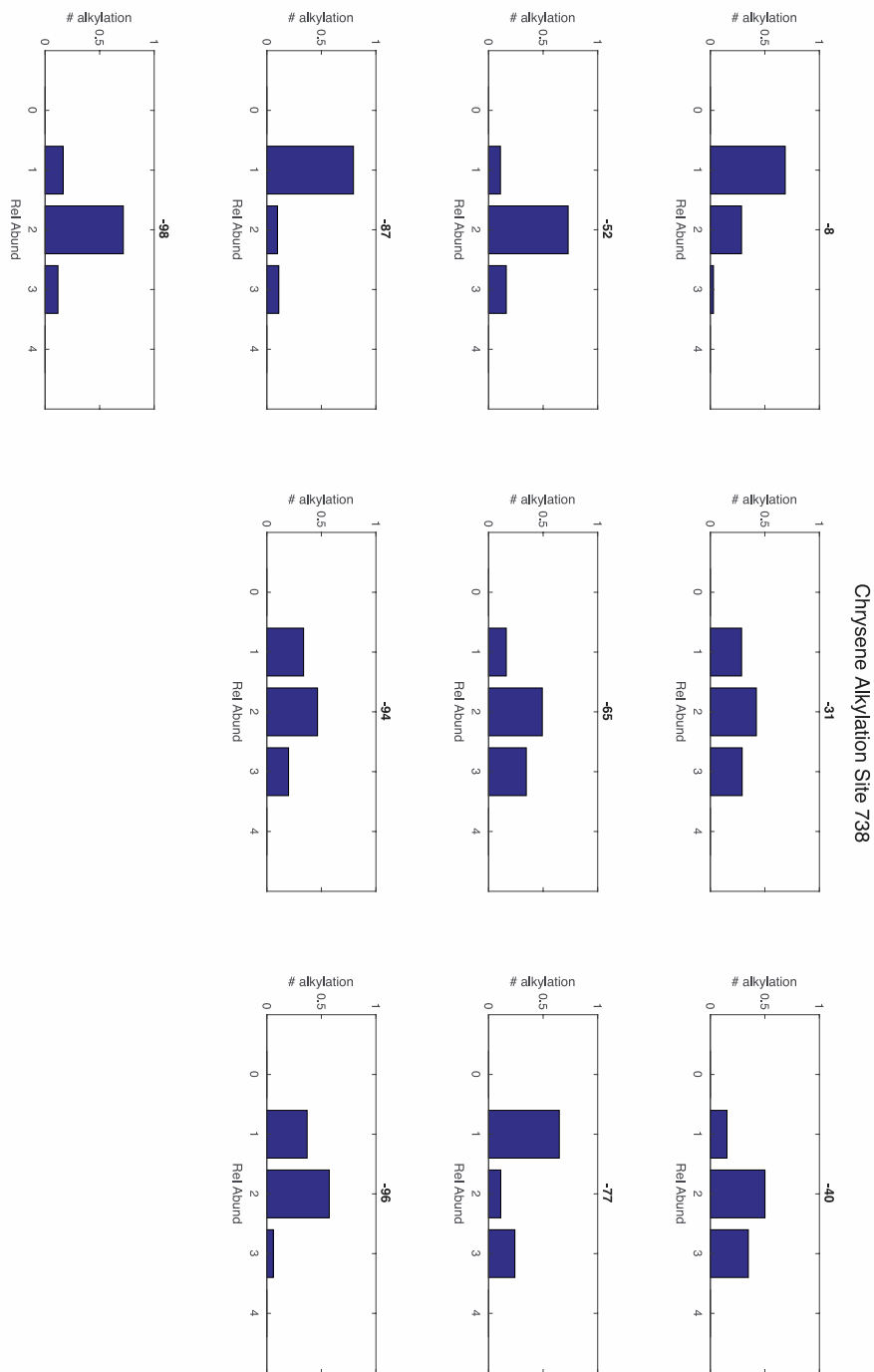
964
Supplemental Figure S20. Relative abundances of alkylated chrysenes from Site 738 at
Kerguelen Plateau demonstrate a heightened abundance of alkylated chrysenes relative to the
non-alkylated parent form. Signatures present various sources (weathered, mixed, pyrogenic, and
petrogenic). Numbers on the x-axis represent the number of methylations, and the y-axis is the
relative abundance of each compound relative to the sum of 0-4 alkylated isomers. Numbers at
the top of each plot represent the depth in Section 738C-20R-5. Numbers at the top of each plot
represent the depth in Section 738C-20R-5.
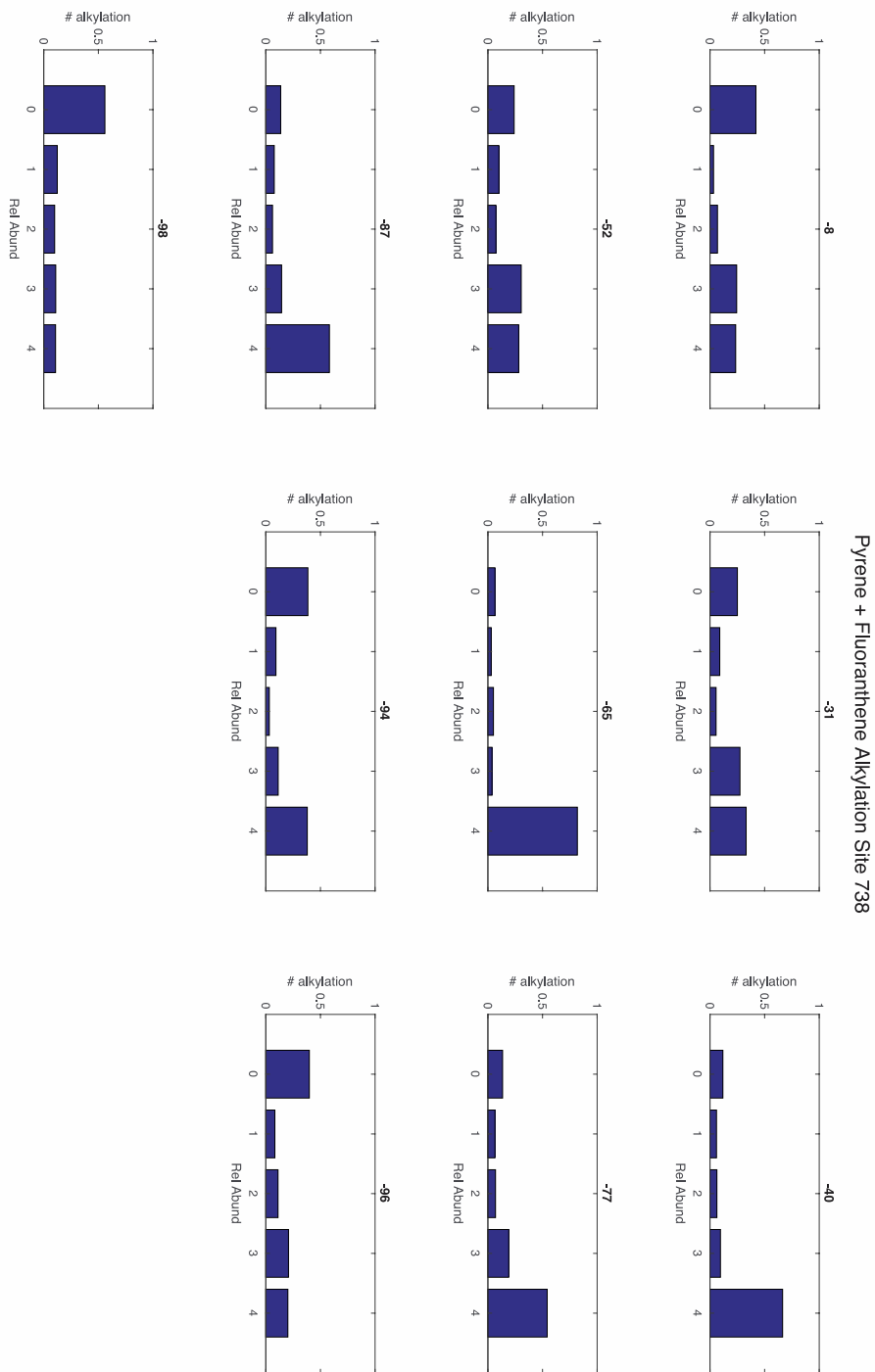
Supplemental Figure S21. Relative abundances of alkylated pyrenes from Site 738 at Kerguelen Plateau demonstrate a heightened abundance of alkylated pyrenes relative to the non-alkylated parent form in sampels at 87 cm and above. Most signatures are consistent with a weathered, source. Numbers on the x-axis represent the number of methylations, and the y-axis is the relative abundance of each compound relative to the sum of 0-4 alkylated isomers. Numbers at the top of each plot represent the depth in Section 738C-20R-5.

979
980 **Supplemental Figure S22.** Relative abundances of alkylated dibenzothiophenes from Site 738 at
981 Kerguelen Plateau demonstrate a heightened abundance of alkylated dibenzothiophenes relative
982 to the non-alkylated parent form. Most signatures are consistent with a weathered, source.
983 Numbers on the x-axis represent the number of methylations, and the y-axis is the relative
984 abundance of each compound relative to the sum of 0-4 alkylated isomers. Numbers at the top of
985 each plot represent the depth in Section 738C-20R-5.
986

Site 738 APDI Pyrene
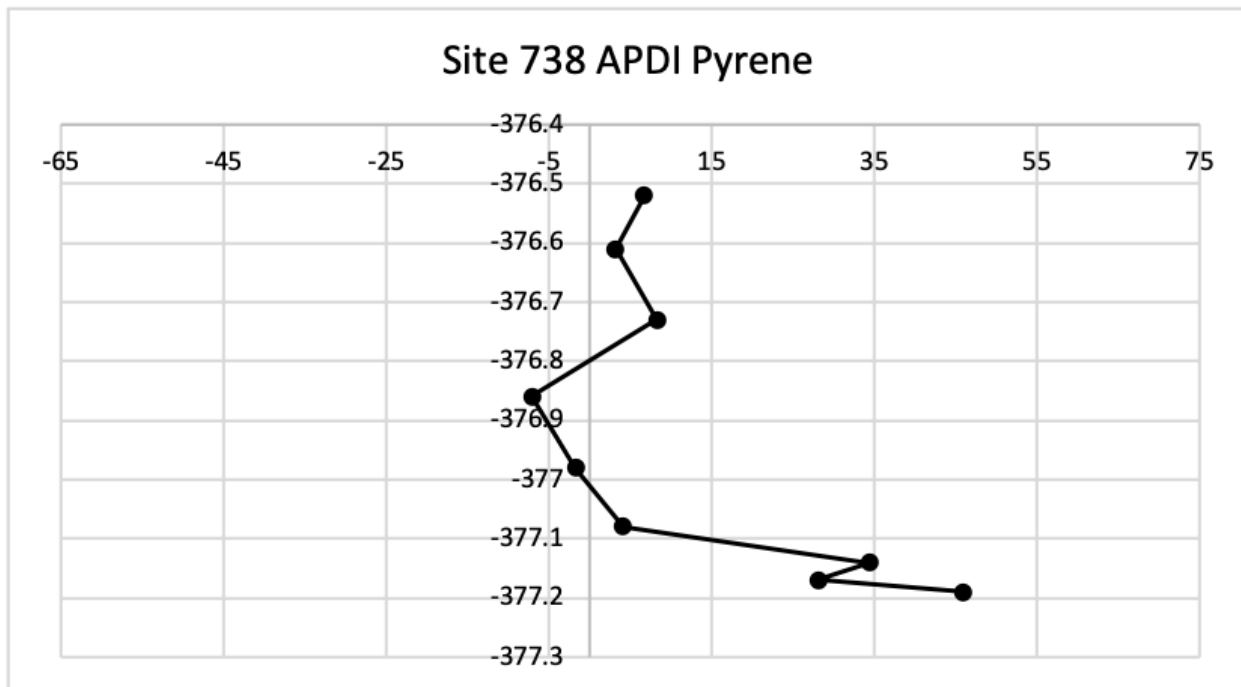
987
988
989 **Supplemental Figure S23.** The Alkylated PAH Distribution Index (51) based on the
990 homologous series of pyrenes presents a shift from positive, "pyrogenic" values to mixed source
991 values at Site 738. The y-axis represents depth (mbsf) at Site 738, and the y-axis is the Pyrene
992 APDI. Negative values indicate a petrogenic source, positive values indicate a pyrogenic source,
993 and values near 0 represent mixed or undiscernible sources.
994
995
996
997

Site 738 APDI Chrysene
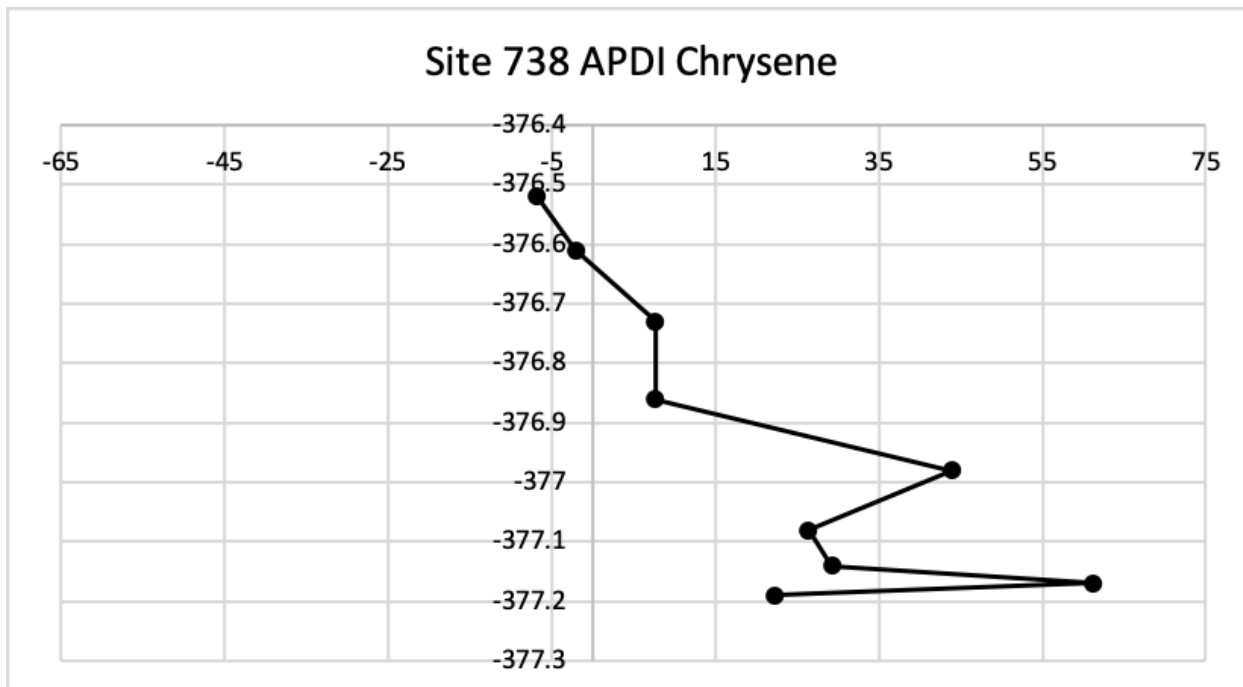
998
999
1000 **Supplemental Figure S24.** The Alkylated PAH Distribution Index (51) based on the
1001 homologous series of chrysenes presents a shift from positive, "pyrogenic" values to mixed
1002 source values at Site 738. The y-axis represents depth (mbsf) at Site 738, and the y-axis is the
1003 Chrysene APDI. Negative values indicate a petrogenic source, positive values indicate a
1004 pyrogenic source, and values near 0 represent mixed or undiscernible sources.
1005
1006
1007
1008
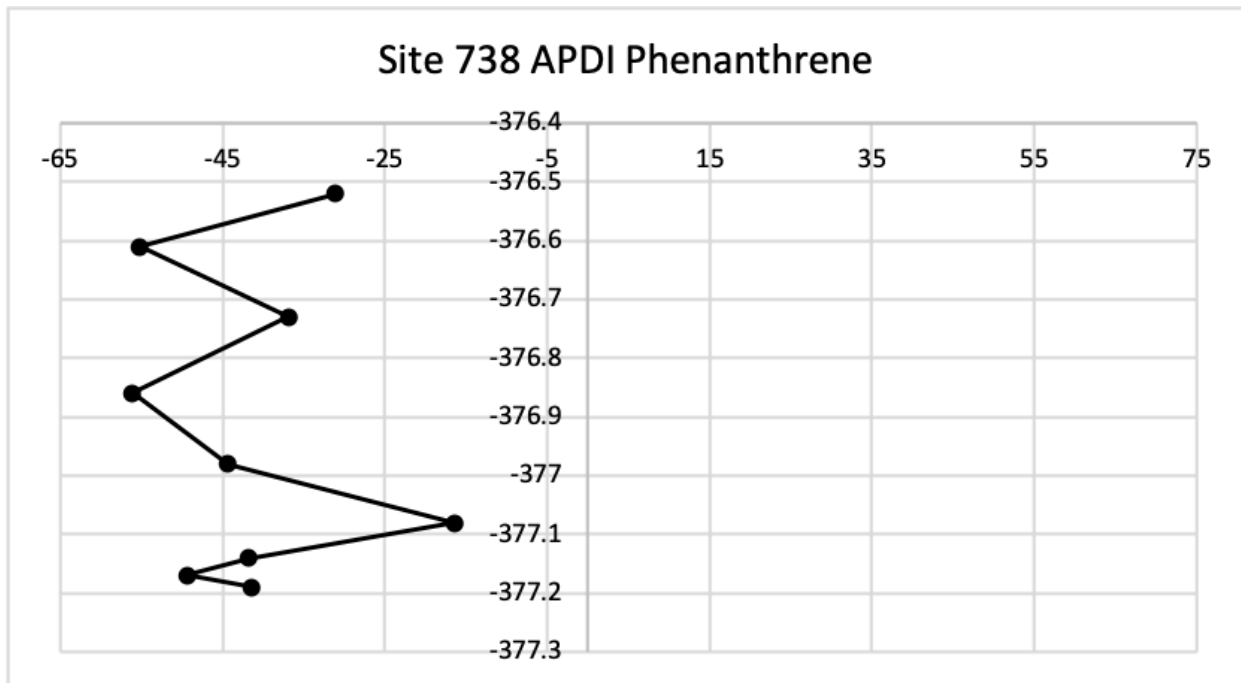
Site 738 APDI Phenanthrene

1009
1010
1011 **Supplemetnal Figure S25.** The Alkylated PAH Distribution Index (51) based on the
1012 homologous series of phenanthrenes presents negative, "petrogenic" source values at Site 738.
1013 The y-axis represents depth (mbsf) at Site 738, and the y-axis is the Phenanthrene APDI.
1014 Negative values indicate a petrogenic source, positive values indicate a pyrogenic source, and
1015 values near 0 represent mixed or undiscernible sources.
1016
1017
1018
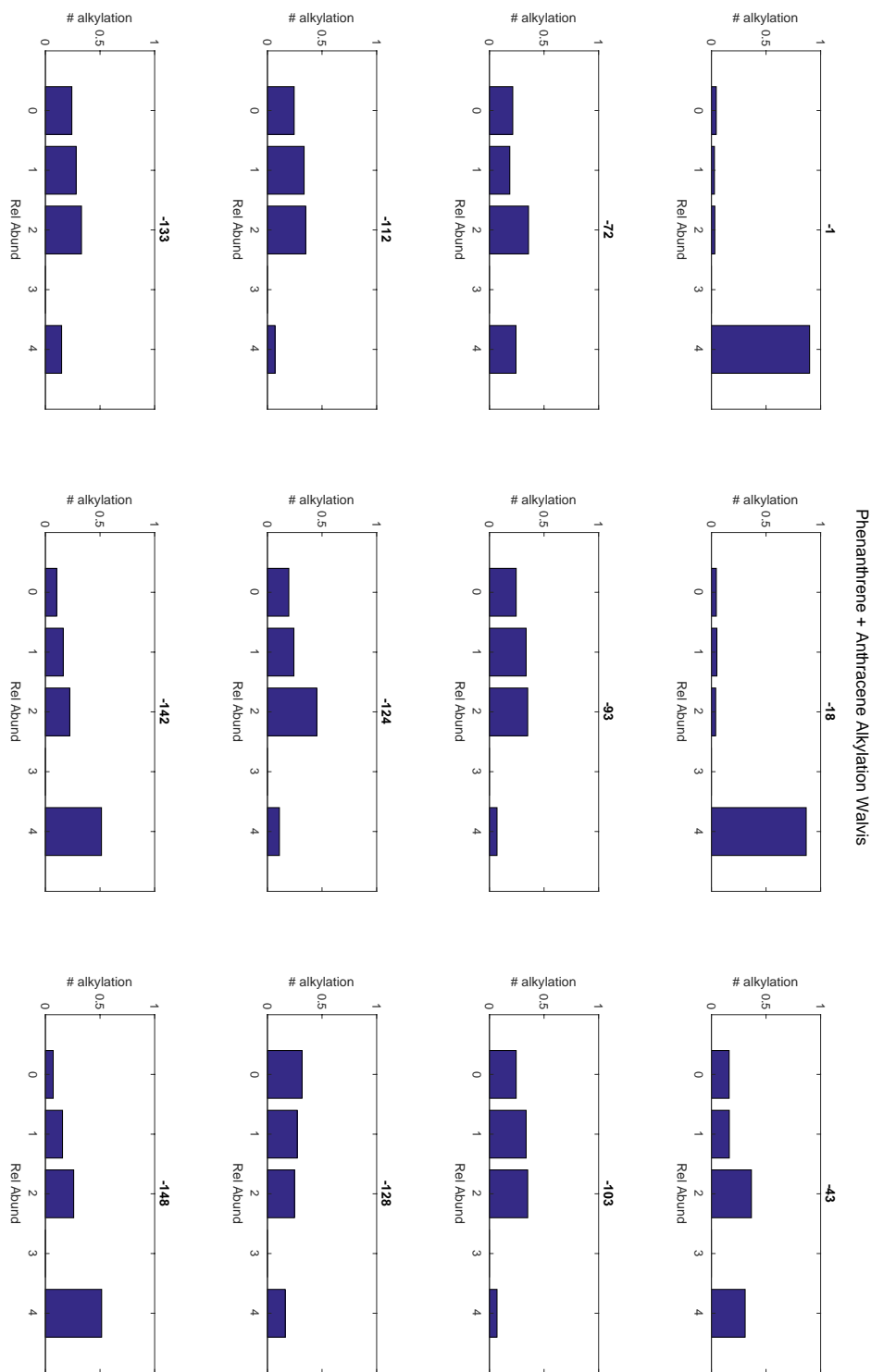
1019
Supplemental Figure S26. Relative abundances of alkylated phenanthrenes from Site 1262 at
Walvis Ridge demonstrate a heightened to equal abundances of alkylated phenanthrenes relative
to the non-alkylated parent form. Most signatures are consistent with a weathered or petrogenic
source. Numbers on the x-axis represent the number of methylations, and the y-axis is the
relative abundance of each compound relative to the sum of 0-4 alkylated isomers. Numbers at
the top of each plot represent the depth in Section 1262B-22H-4.
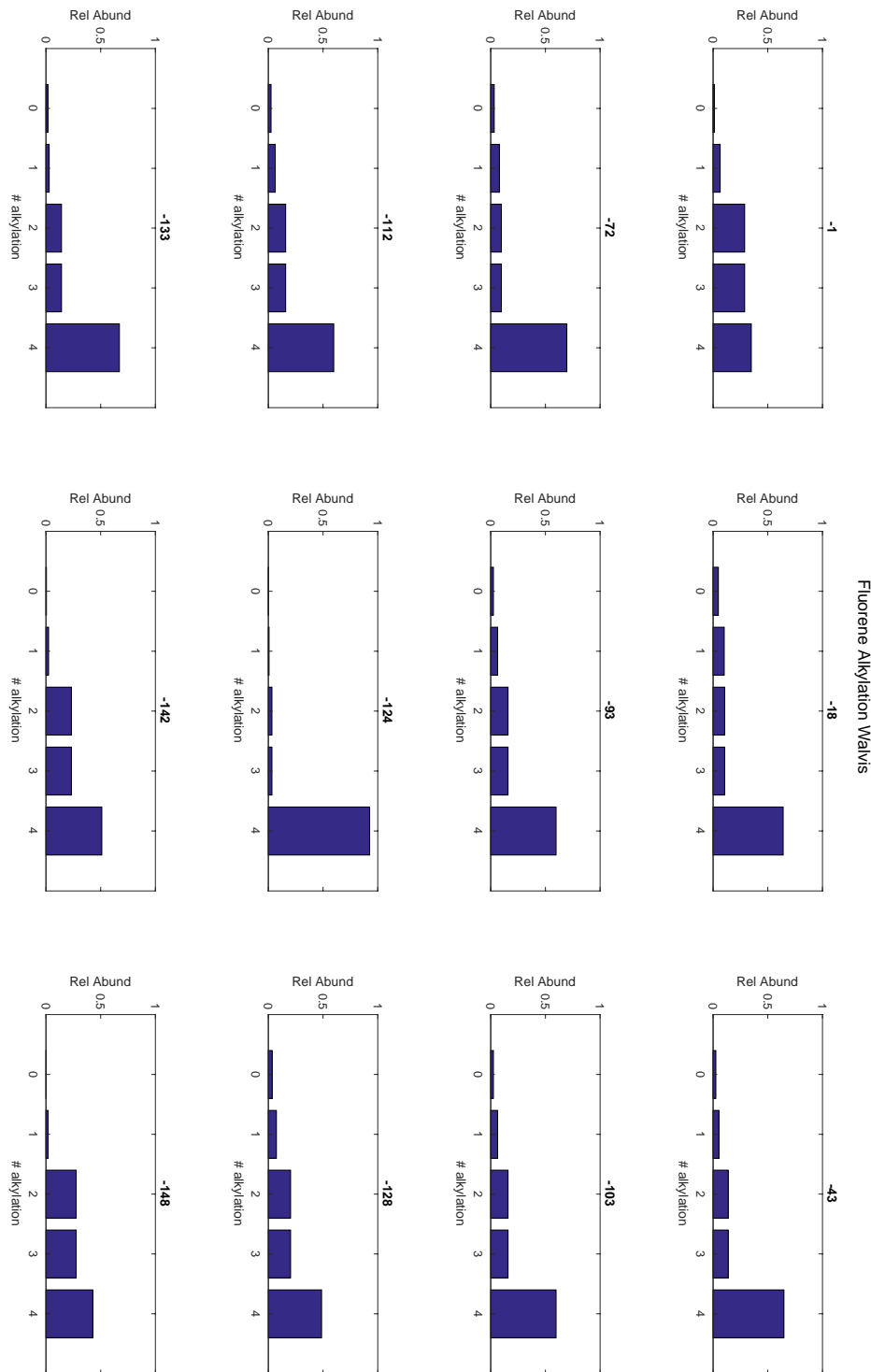
1026
Supplemental Figure S27. Relative abundances of alkylated fluorenes from Site 1262 at Walvis
Ridge demonstrate a heightened to equal abundances of alkylated fluorenes relative to the non-
alkylated parent form. Most signatures are consistent with a weathered source. Numbers on the
x-axis represent the number of methylations, and the y-axis is the relative abundance of each
compound relative to the sum of 0-4 alkylated isomers. Numbers at the top of each plot represent
the depth in Section 1262B-22H-4.
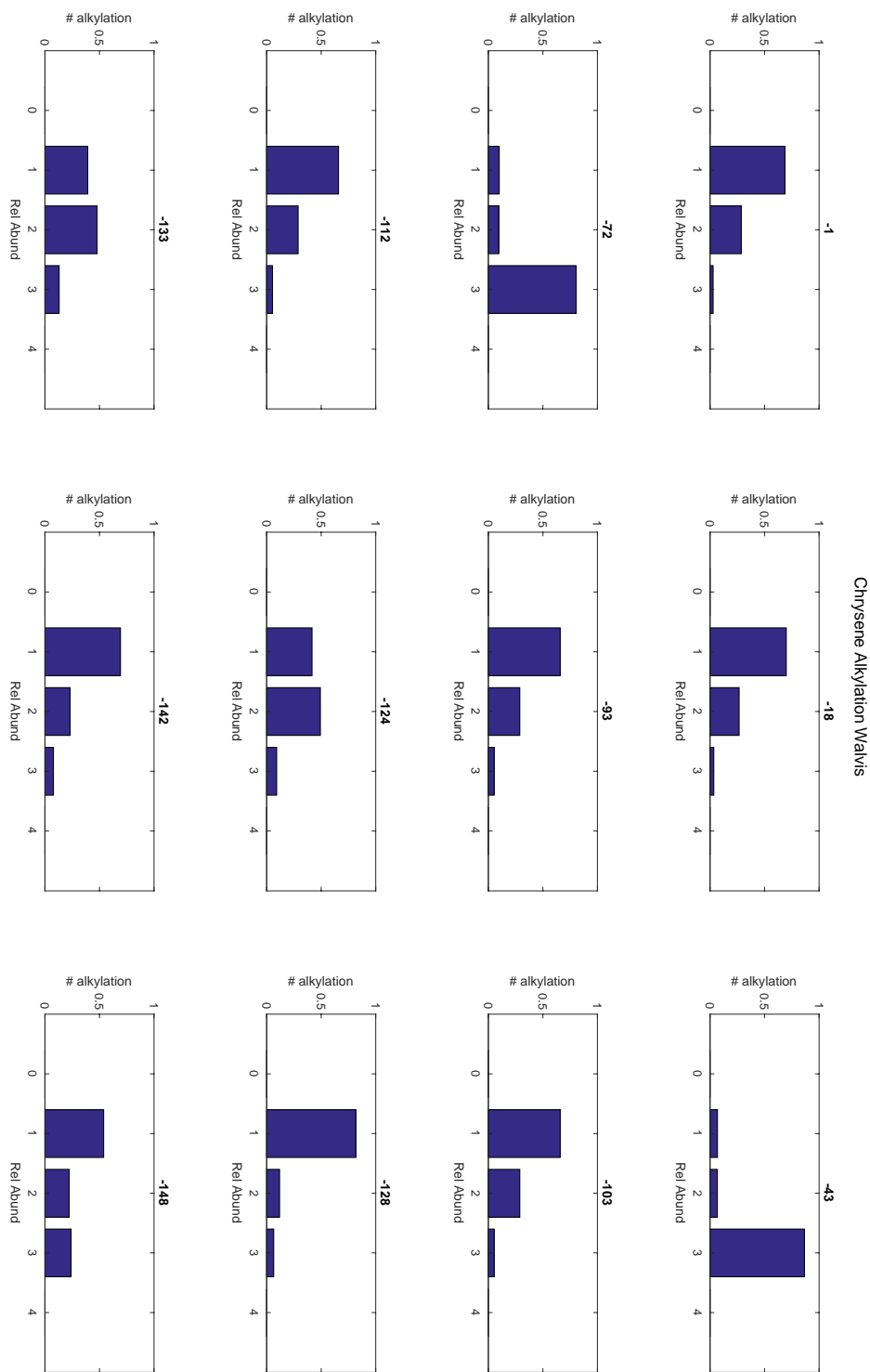
1033
**Supplemental Figure S28.** Relative abundances of alkylated chrysenes from Site 1262 at
Walvis Ridge demonstrate a heightened abundance of alkylated chrysenes relative to the non-
alkylated parent form. Most signatures are consistent with a petrogenic source. Numbers on the
x-axis represent the number of methylations, and the y-axis is the relative abundance of each
compound relative to the sum of 0-4 alkylated isomers. Numbers at the top of each plot represent
the depth in Section 1262B-22H-4.

46
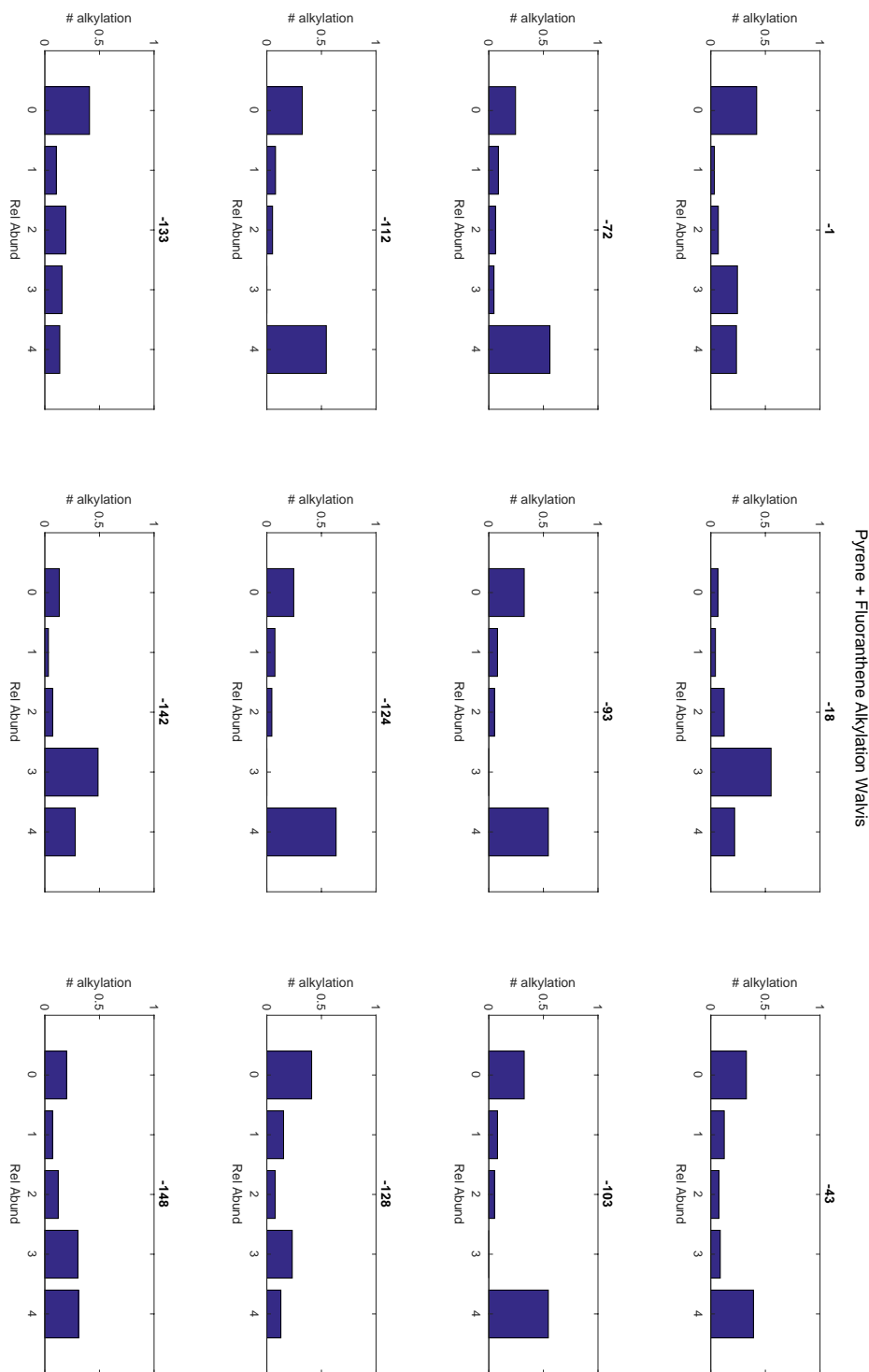
1040
Supplemental Figure S29. Relative abundances of alkylated pyrenes from Site 1262 at Walvis
Ridge demonstrate mixed abundances of alkylated phenanthrenes relative to the non-alkylated
parent form. Signatures range from petrogenic to pyrogenic; most appear weathered. Numbers on
the x-axis represent the number of methylations, and the y-axis is the relative abundance of each
compound relative to the sum of 0-4 alkylated isomers. Numbers at the top of each plot represent
the depth in Section 1262B-22H-4.
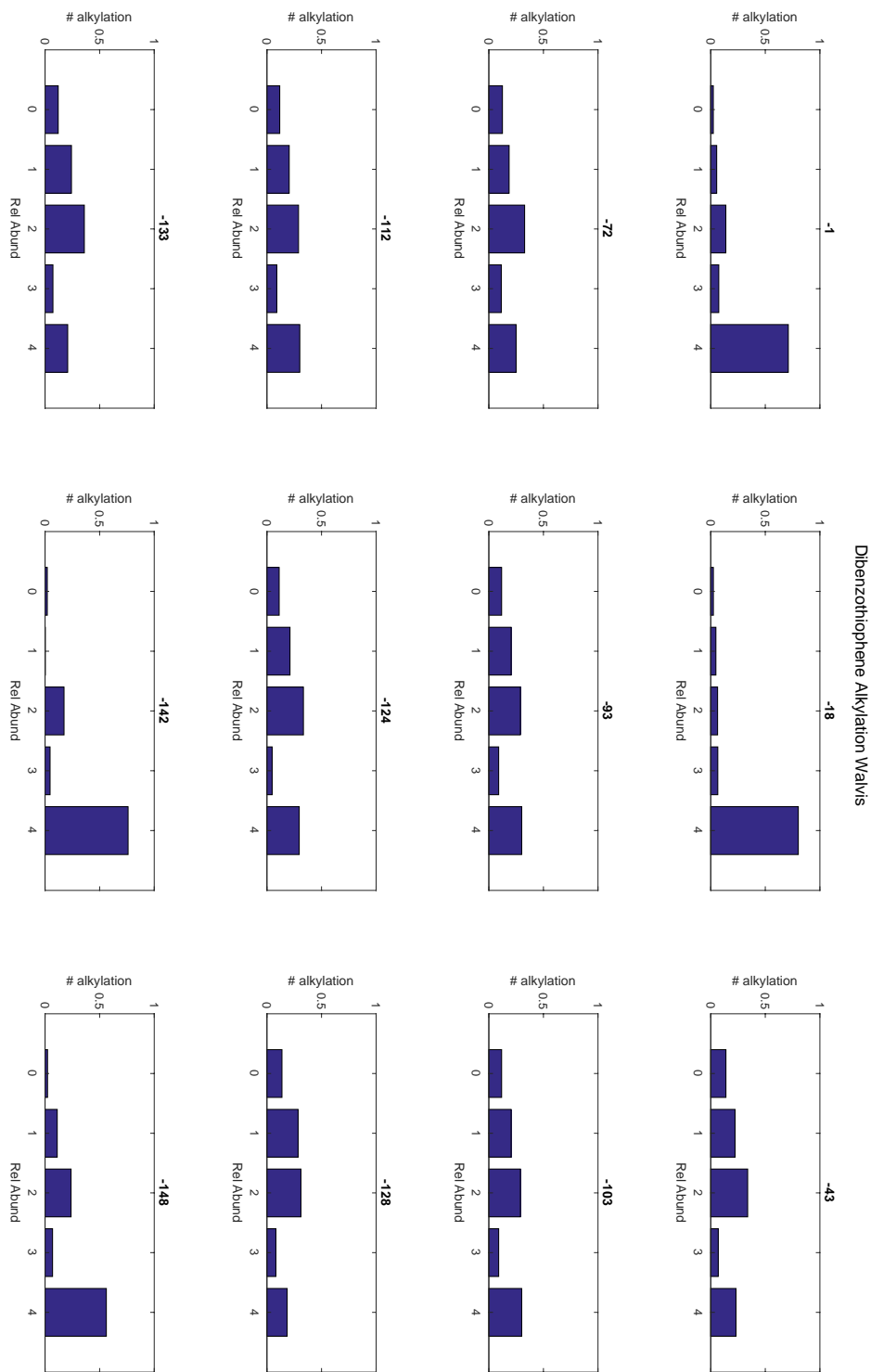
1047
Supplemental Figure S30. Relative abundances of alkylated dibenzothiophenes from Site 1262
at Walvis Ridge demonstrate a heightened abundance of alkylated dibenzothiophenes relative to
the non-alkylated parent form. Most signatures are consistent with a weathered or petrogenic
source. Numbers on the x-axis represent the number of methylations, and the y-axis is the
relative abundance of each compound relative to the sum of 0-4 alkylated isomers. Numbers at
the top of each plot represent the depth in Section 1262B-22H-4.

Site 1262 APDI Pyrene
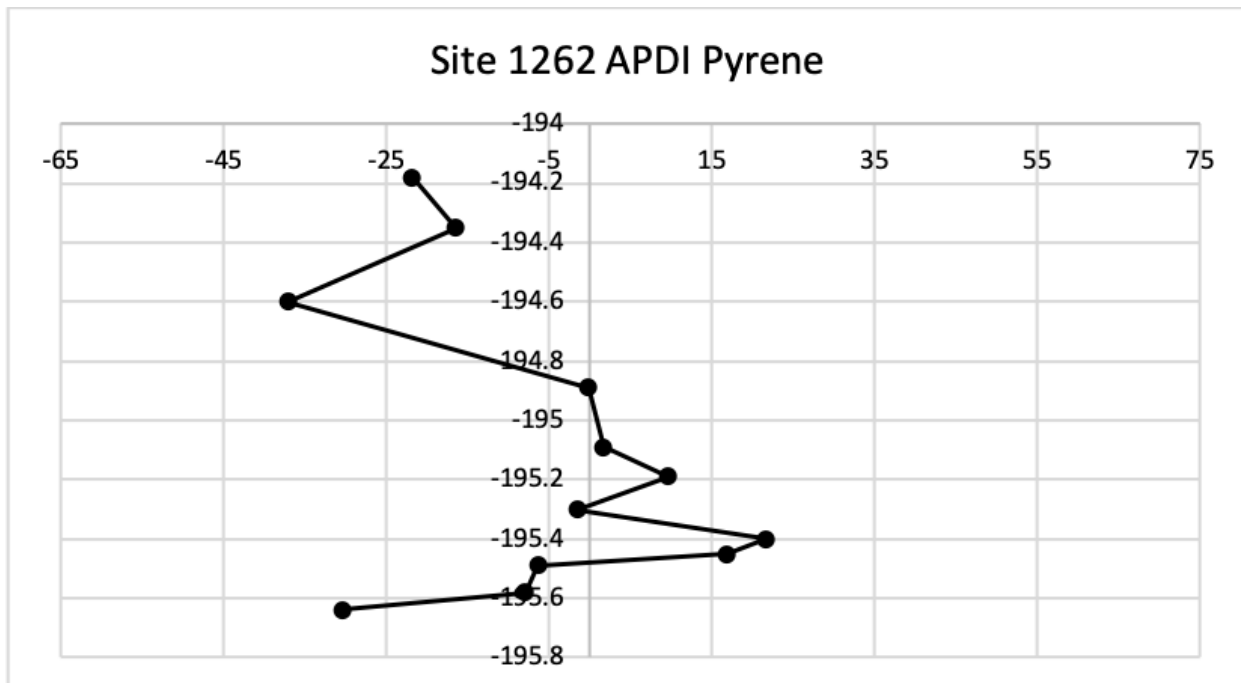
1054
1055
1056 **Supplemental Figure S31.** The Alkylated PAH Distribution Index (51) based on the
1057 homologous series of pyrenes presents negative, "petrogenic" source values in the K-Pg
1058 boundary layer at Site 1262, shifting to mixed or pyrogenic signatures, and back to mixed values.
1059 The y-axis represents depth (mbsf) at Site 1262, and the y-axis is the Pyrene APDI. Negative
1060 values indicate a petrogenic source, positive values indicate a pyrogenic source, and values near
1061 0 represent mixed or undiscernible sources.
1062
1063
1064

Site 1262 APDI Chrysene
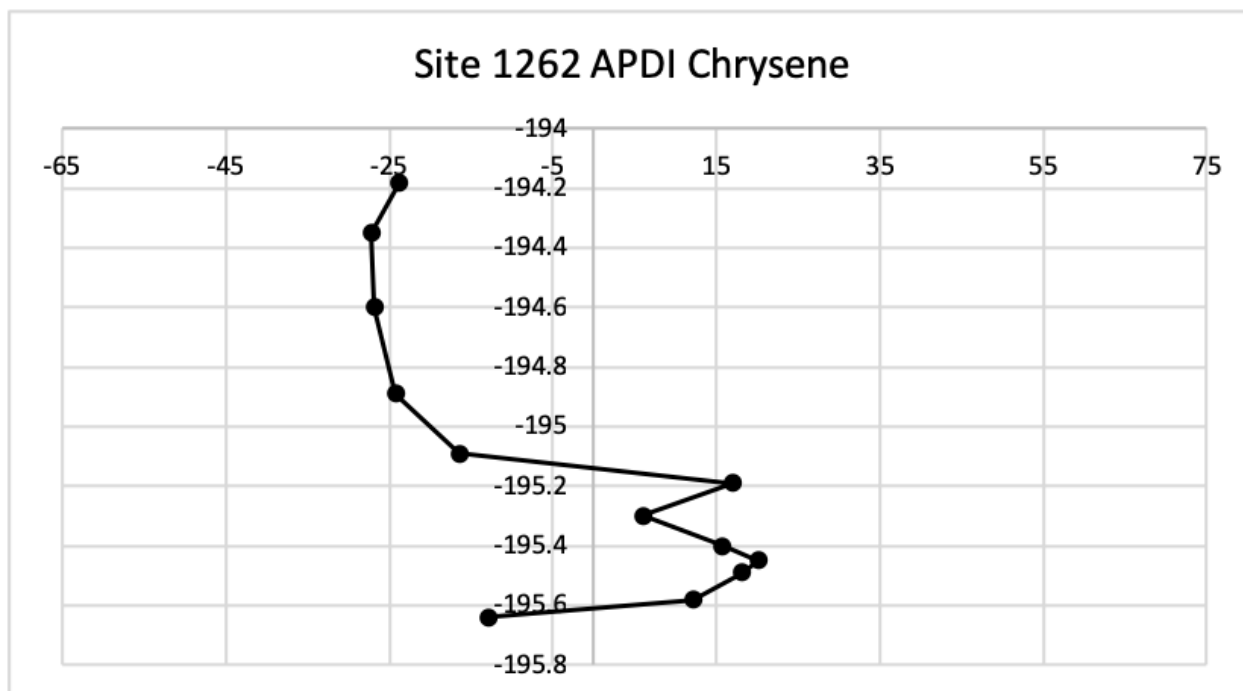
1065
1066
1067 **Supplemental Figure S32.** The Alkylated PAH Distribution Index (51) based on the
1068 homologous series of chrysenes presents negative, "petrogenic" source values in the K-Pg
1069 boundary layer at Site 1262, shifting to mixed or pyrogenic signatures, and back to petrogenic
1070 values. The y-axis represents depth (mbsf) at Site 1262, and the y-axis is the Chrysene APDI.
1071 Negative values indicate a petrogenic source, positive values indicate a pyrogenic source, and
1072 values near 0 represent mixed or undiscernible sources.
1073
1074
1075

Site 1262 APDI Phenanthrene
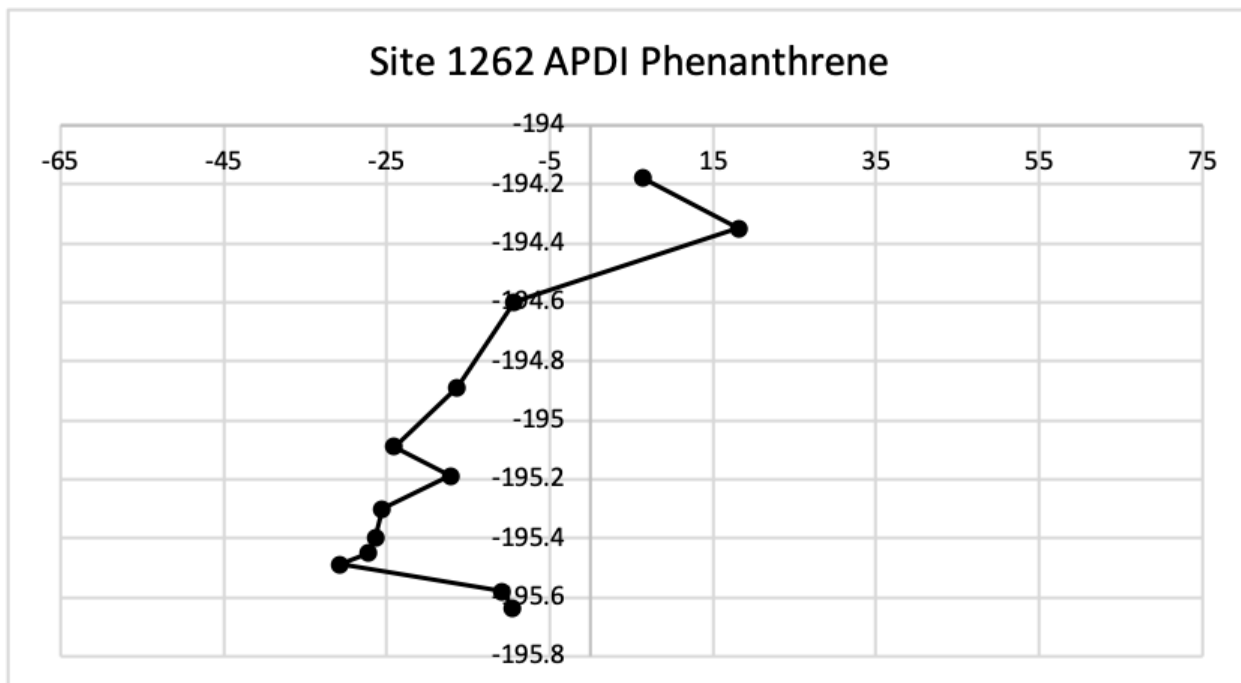
1076
1077
1078 **Supplemental Figure S33.** The Alkylated PAH Distribution Index (51) based on the
1079 homologous series of phenanthrene presents negative, "petrogenic" to positive "pyrogenic"
1080 sources. The y-axis represents depth (mbsf) at Site 1262, and the y-axis is the Phenanthrene
1081 APDI. Negative values indicate a petrogenic source, positive values indicate a pyrogenic source,
1082 and values near 0 represent mixed or undiscernible sources.
1083
1084
1085
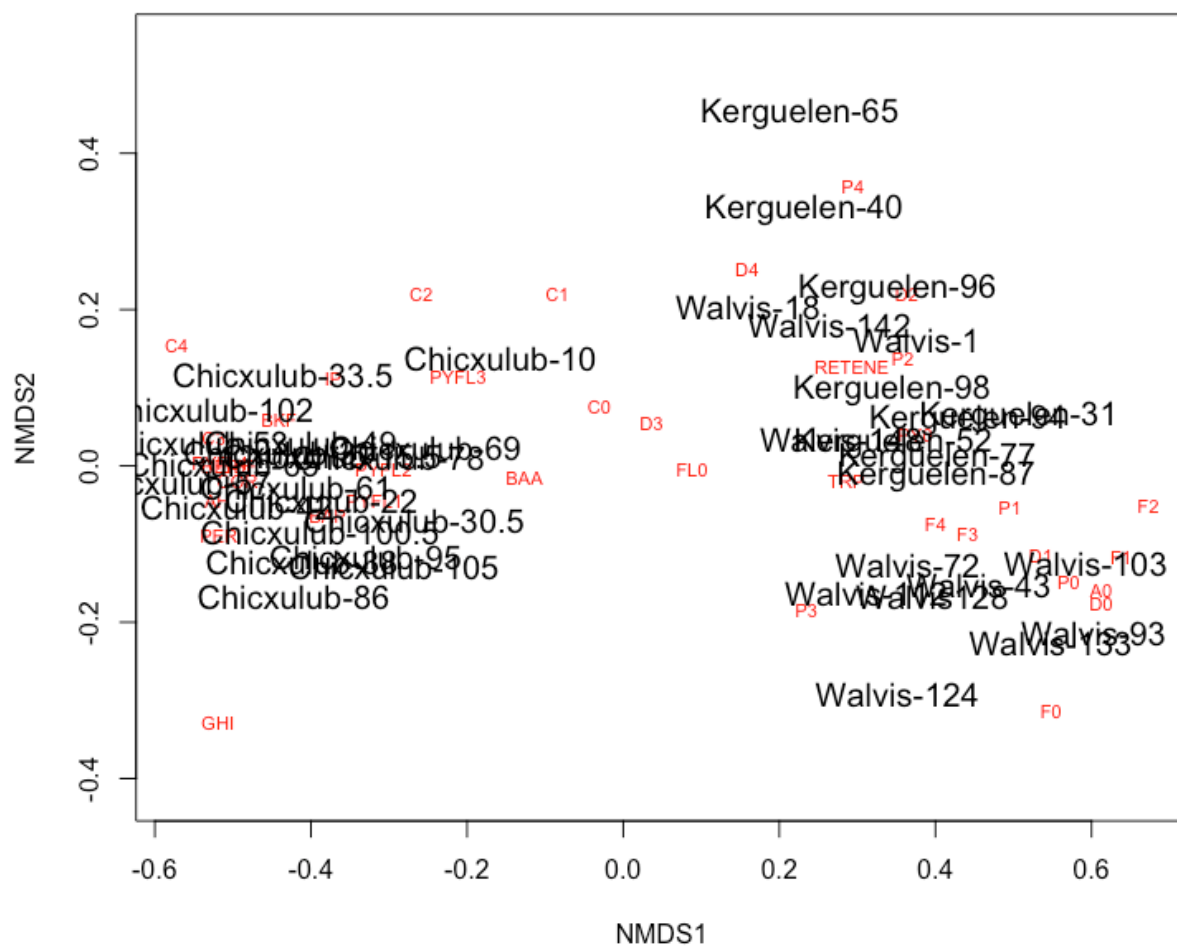
1086
1087 **Supplemental Figure S34.** Results from Q mode Nonmetric Multidimensional Scaling
1088 (NMDS). Samples are displayed in black, in the format of "Site Name – Depth," where the depth
1089 refers to the depth in each core section (0077-40R-1 for Chicxulub, 738C-20R-5 for Kerguelen
1090 Plateau, and 1262B-22H-4 for Walvis Ridge). Variables, PAHs in this case, are displayed in
1091 black. The number refers to the number of alkylations.
1092
1093
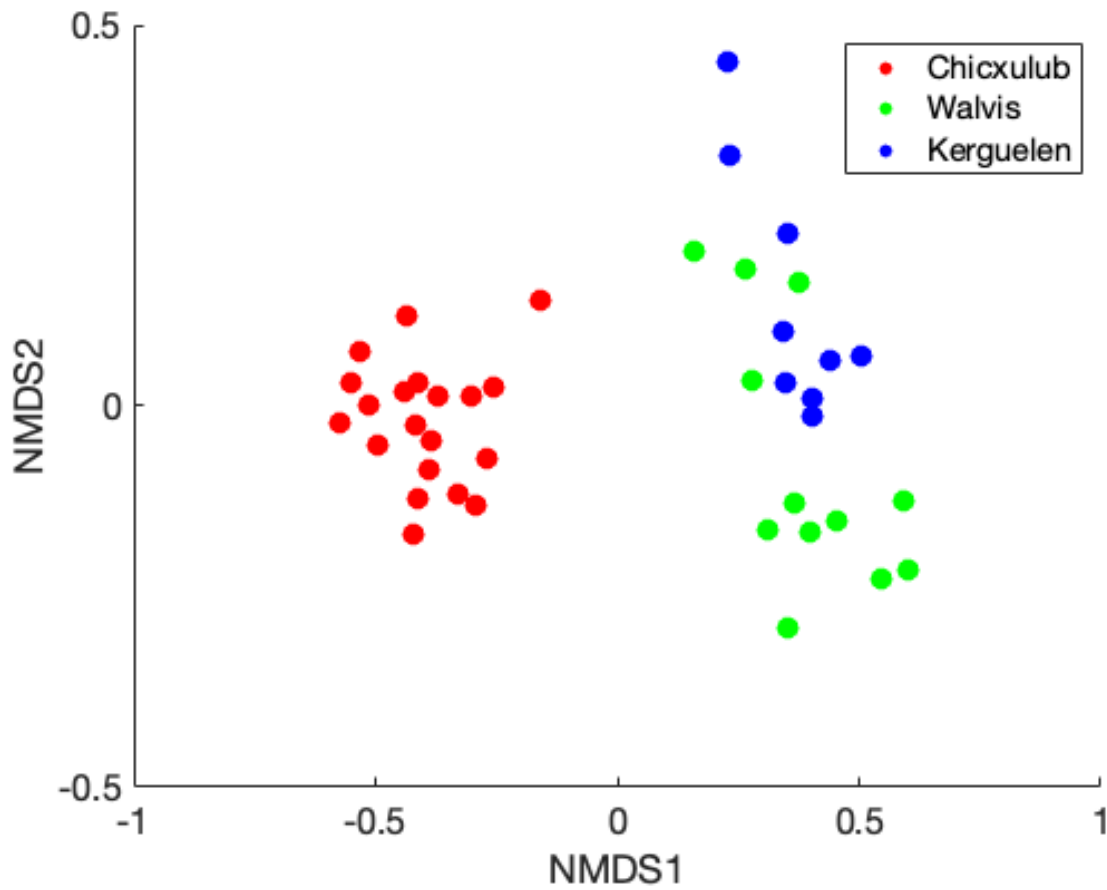
1094
1095 **Supplemental Figure S35**. Q mode NMDS results colored by location. Only samples are
1096 displayed, where Chicxulub (Site M0077) samples are colored in red, Walvis Ridge samples
1097 (Site 1262) are colored in green, and Kerguelen Plateau samples (Site 738) are colored in blue.
1098 Separation between Site M0077 and the two distal sites is observed on NMDS1, and separation
1099 between Site 738 and Site 1262 is observed on NMDS2.
1100
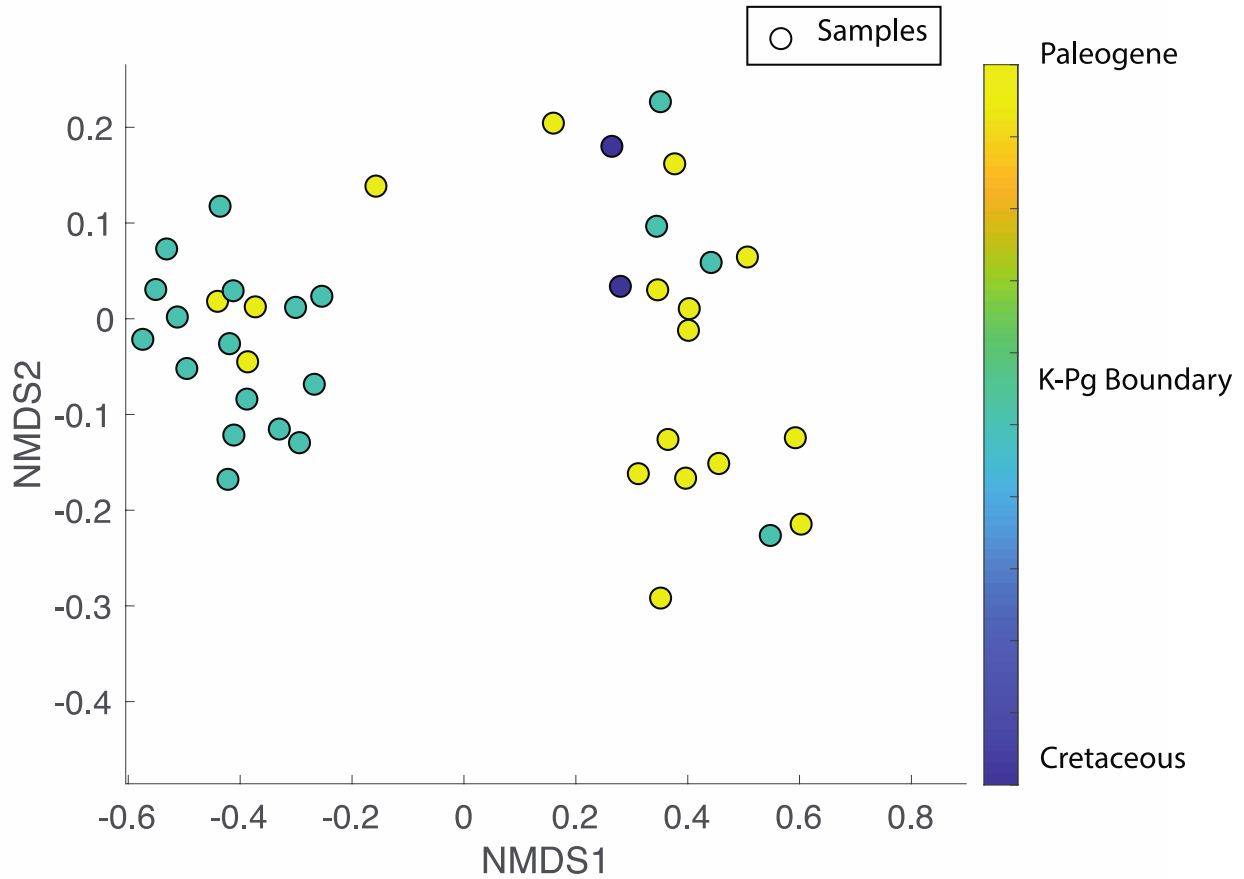
1101
1102
1103 **Supplemental Figure S36**. Q mode NMDS results colored by timing. Only samples are
1104 displayed, where K-Pg boundary samples ("1") are displayed in green, Cretaceous samples ("0")
1105 are displayed in blue, and Paleogene samples ("2") are displayed in yellow. We do not observe a
1106 major separation within the NMDS based on timing.
1107
1108
1109
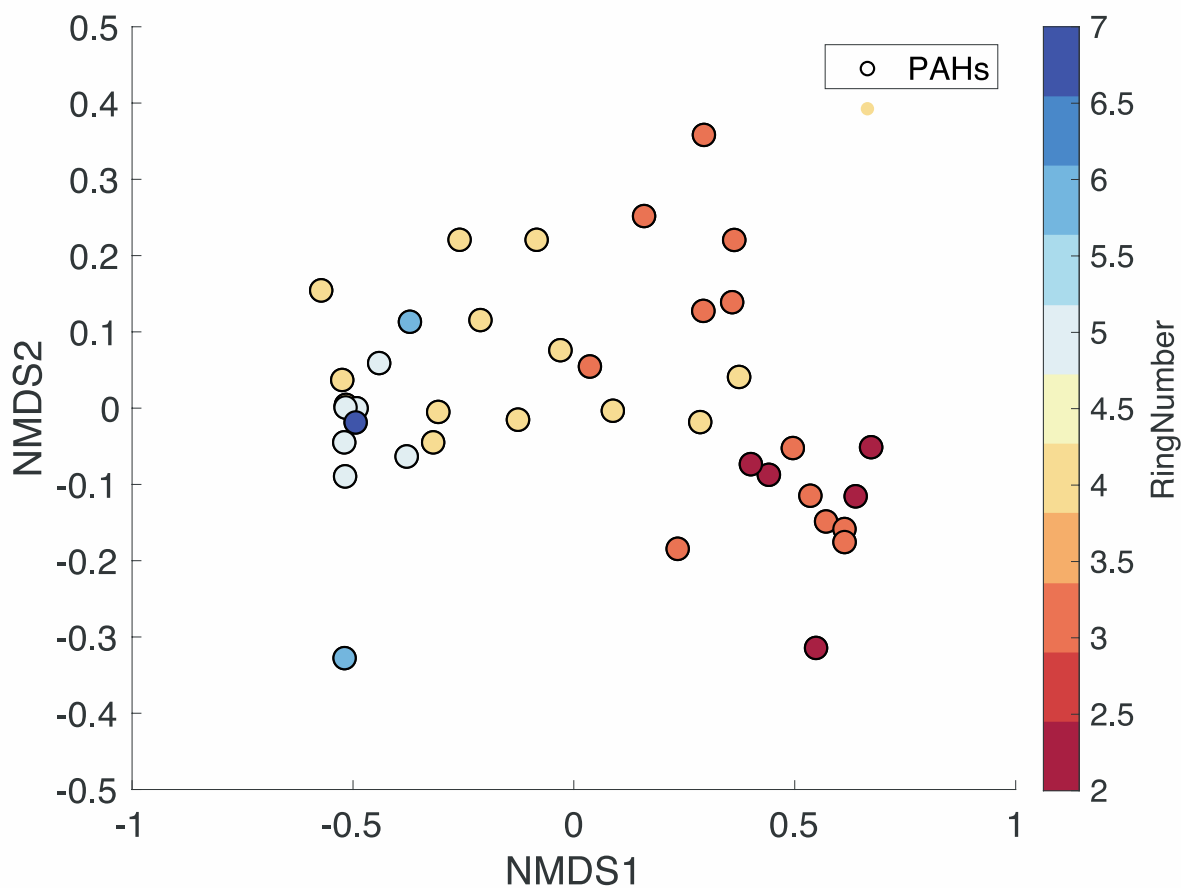
Supplemental Figure S37. Q mode NMDS results colored by ring number of PAHs. Only variables (PAHs) are displayed, where the color of each point corresponds to the number of rings of the compound. Warm colors represent small, lower ring number PAHs, where the smallest is fluorene, and cool colors represent larger PAHs, where the largest is coronene. A PAH size gradient is observed along NMDS1, where larger PAHs load negatively and smaller PAHs load positively on NMDS1. We suggest this is a function of transport propensity.
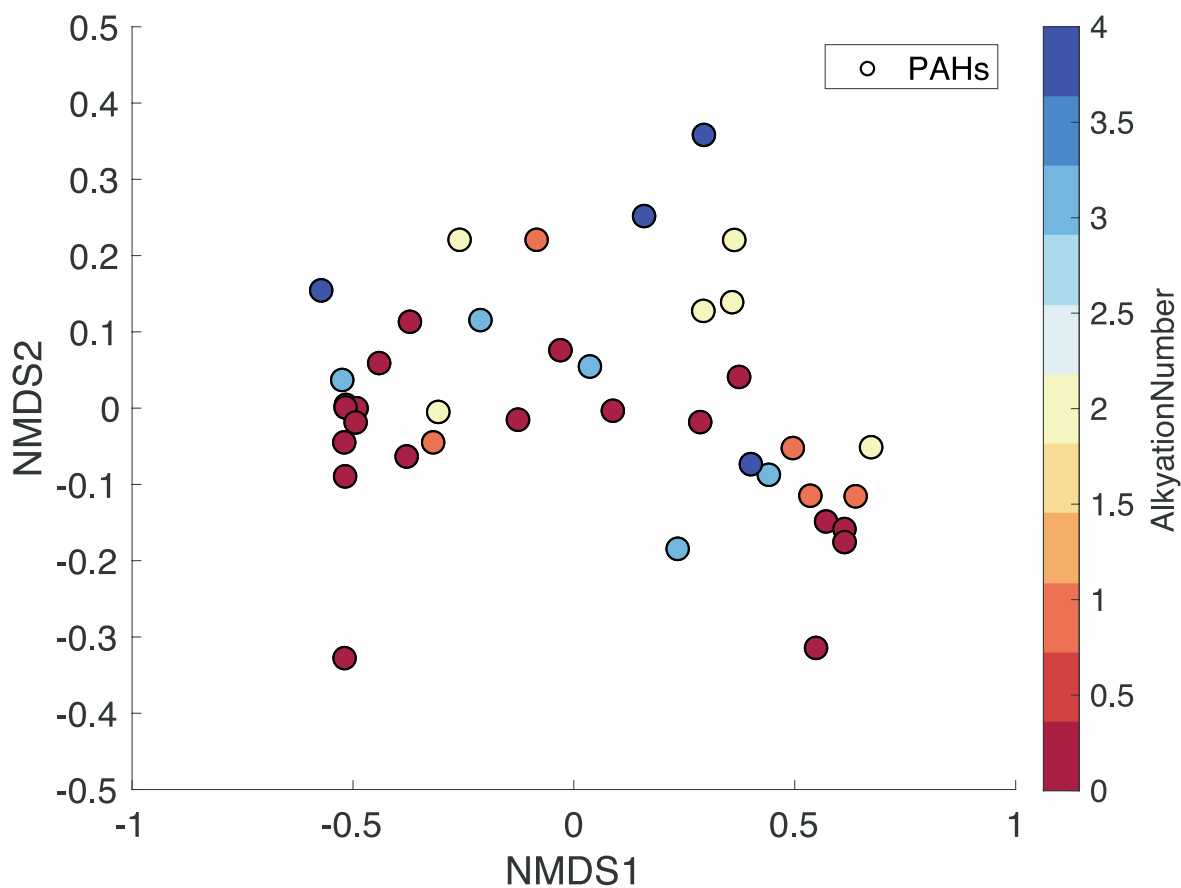
Supplemental Figure S38. Q mode NMDS results colored by the number of alkylations on each PAH species. Only variables (PAHs) are displayed, where warm colors represent parent, non-akylated species, and cool colors progressively represent more alkylated species. A slightly more negative loading on NMDS2 is observed for parent (non-alkylated) species, and a slightly more positive loading is observed for more alkylated species. There are no differences on NMDS1, and thus no differences controlling the distribution between sites.
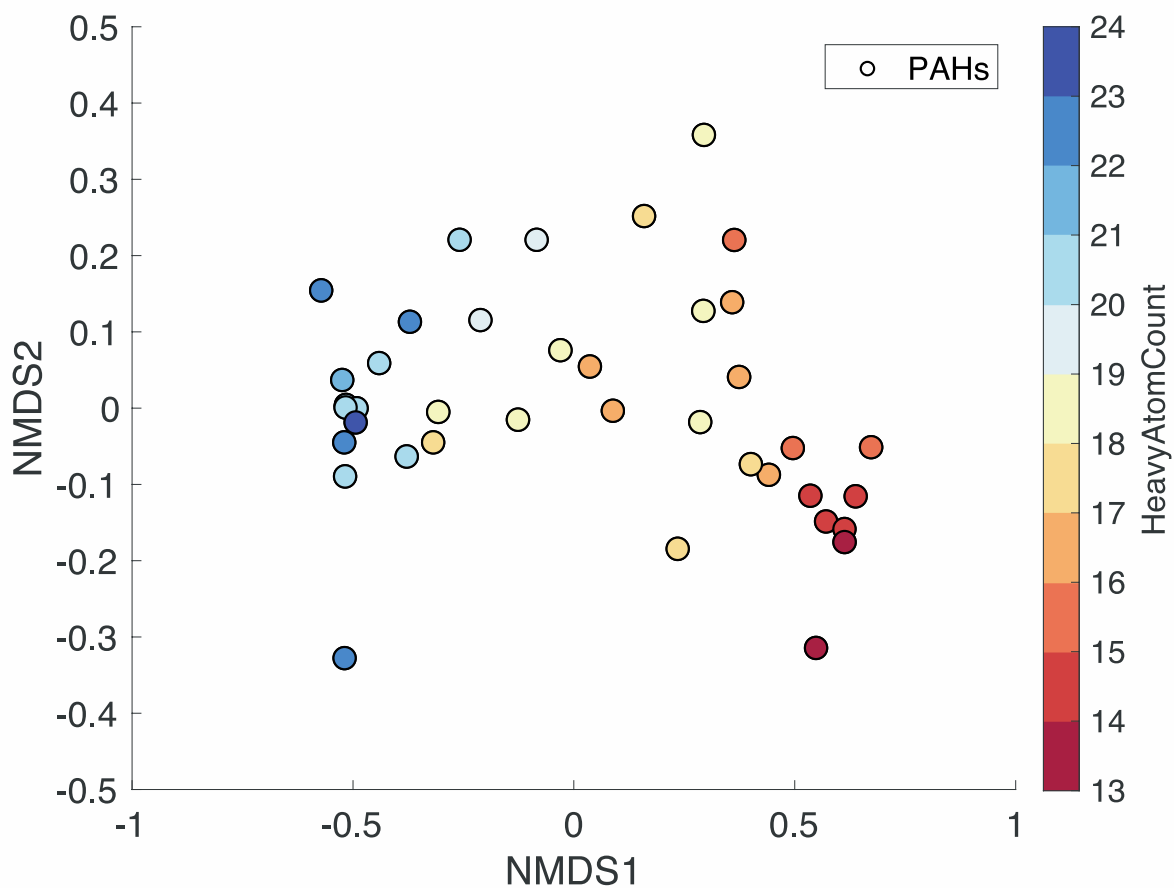
1130
1131
1132 **Supplemental Figure S39.** Q mode NMDS results colored by the number of heavy atoms on
1133 each PAH species. Heavy atom count is associated with molecular weight (more heavy atoms,
1134 heavier compound) and also transport (more heavy atoms, less susceptible to transport)- we can
1135 summarize the association with NMDS1 and heavy atom count to transport. Heavy atoms in this
1136 dataset include carbon and sulfur. Warm colors represent fewer heavy atoms, cool colors
1137 represent more heavy atoms.
1138
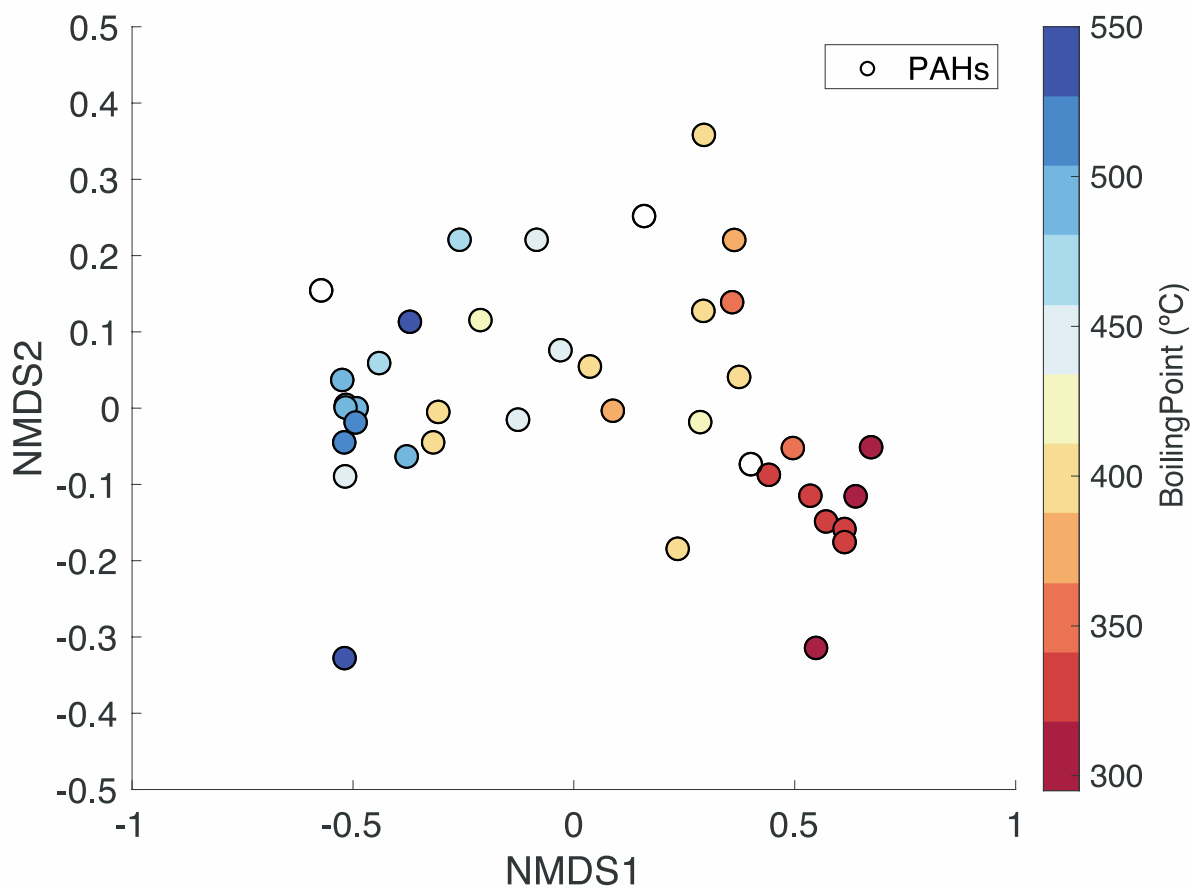
Supplemental Figure S40. Q mode NMDS results colored by the boiling point of each PAH species. Only variables (PAHs) are displayed. Positively loading on NMDS1 are low boiling point compounds (warm colors), which are also associated with the distal sites. Loading negatively on NMDS1 are the high boiling point compounds (less likely to be in the vapor)-associated with the Chicxulub samples (cool colors). Boiling point and transport dynamics are linked.
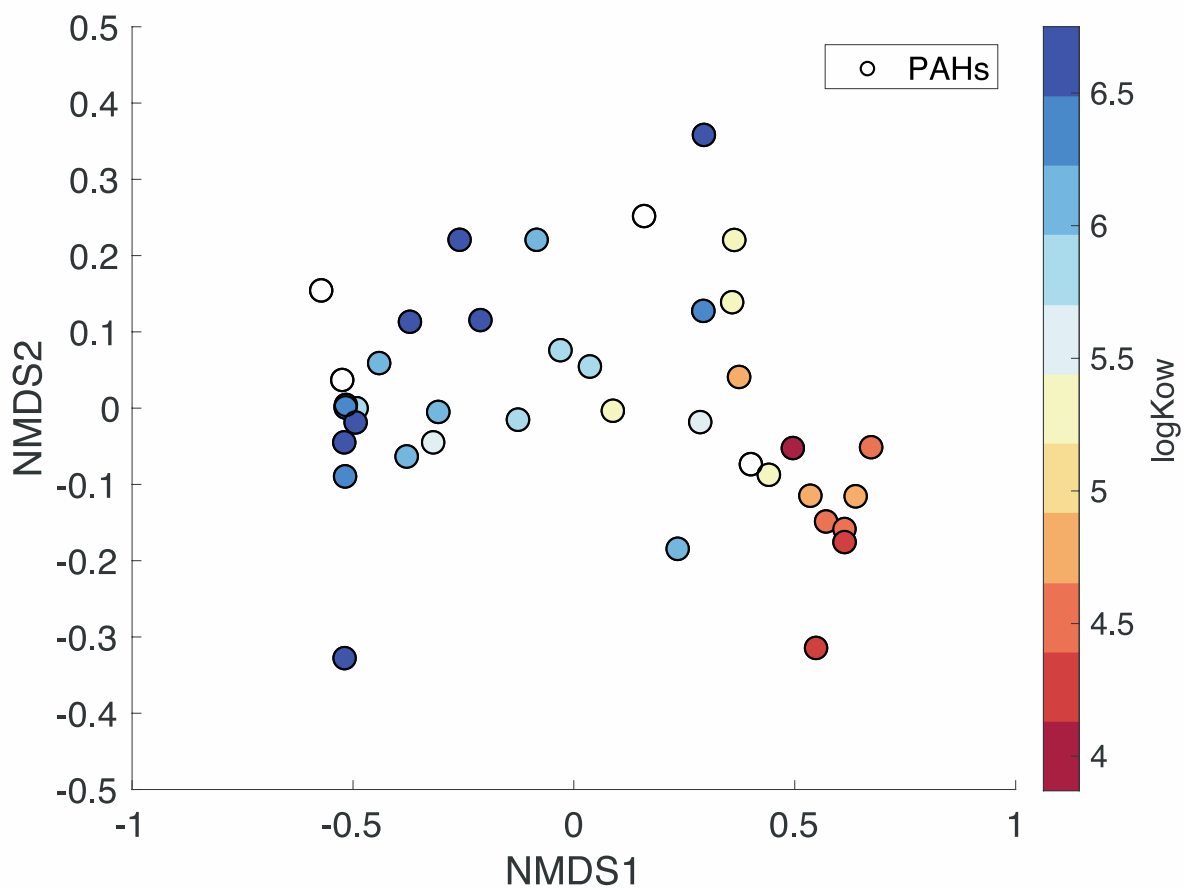
Supplemental Figure S41. Q mode NMDS results colored by the logK$_{ow}$ of each PAH species. Only variables (PAHs) are displayed. NMDS1 separates low logK$_{ow}$ (positive loadings / associated with distal sites / warm colors) and high logK$_{ow}$ (negative loadings / associated with Chicxulub samples / cool colors). Higher logK$_{ow}$ means that a sample is more likely to associate with an organic phase than a water, indicating less water-soluble compounds. Low logK$_{ow}$ values represent relatively more water-soluble compounds with increased susceptibility to transport.
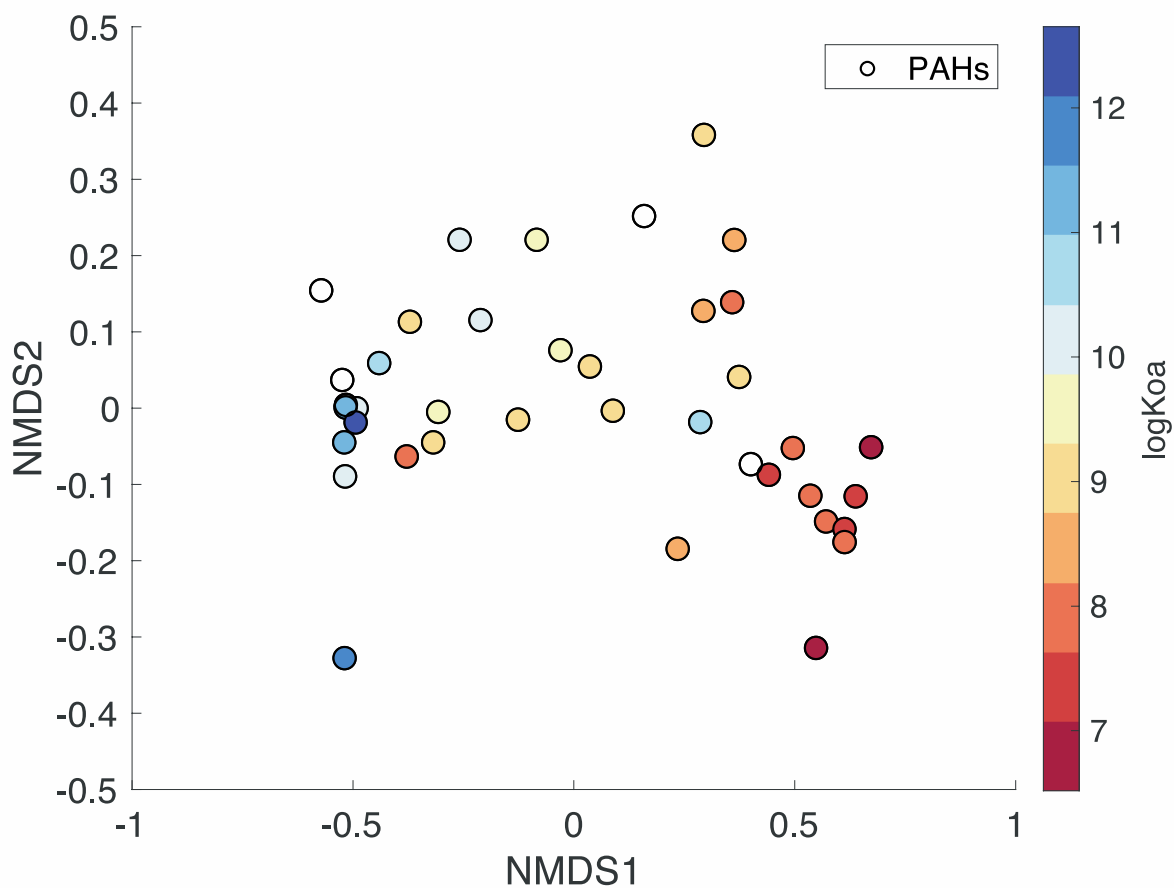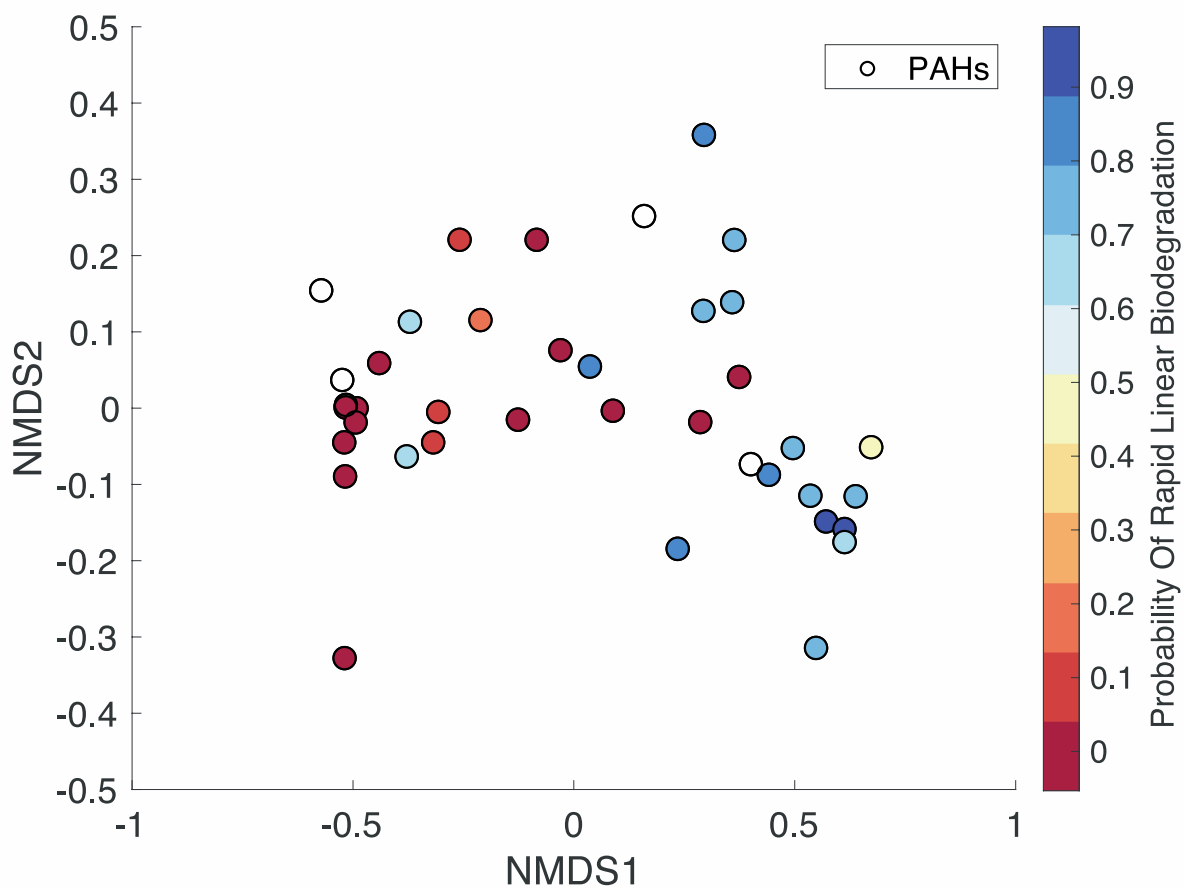
Supplemental Figure S42. Q mode NMDS results colored by the $\log K_{oa}$ of each PAH species. Only variables (PAHs) are displayed. NMDS1 separates low $\log K_{oa}$ (positive loadings / associated with distal sites / warm colors) and high $\log K_{oa}$ (negative loadings / associated with Chicxulub samples / cool colors). Higher $\log K_{oa}$ means that a sample is more likely to associate with an organic phanse than an air phase, indicating less volatile compounds. Low $\log K_{oa}$ values represent relatively more volatile compounds with increased susceptibility to transport.
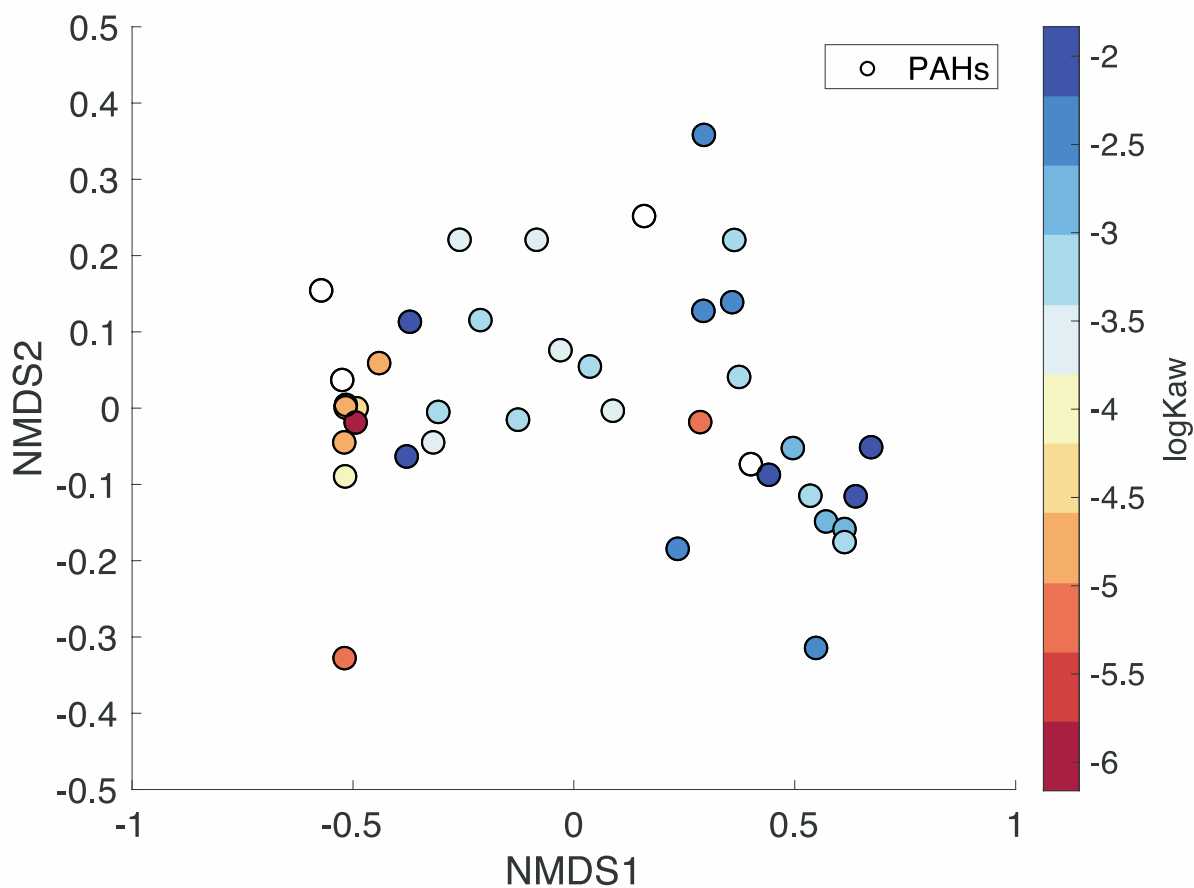
1163
1164
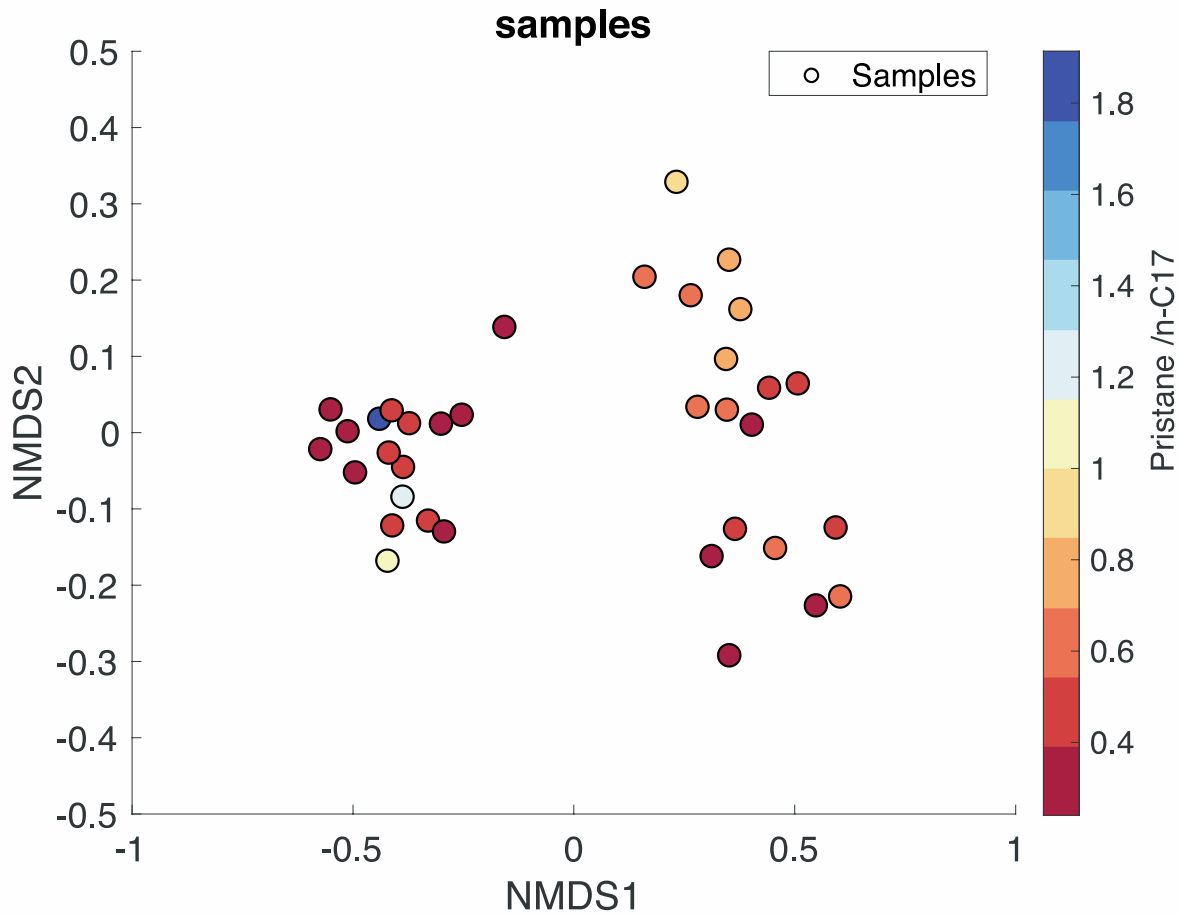1165   **Supplemental Figure S43.** Q mode NMDS results colored by the $\log K_{aw}$ each PAH species.
1166   Only variables (PAHs) are displayed. PAHs with high $\log K_{aw}$ values load positively on NMDS1,
1167   whereas PAHs with low $\log K_{aw}$ values load negatively on NMDS1. Warm colors represent lower
1168 $\log K_{aw}$ PAHs, and cool colors represent higher $\log K_{aw}$ PAHs. As $\log K_{aw}$ increases, the more
1169   likely a compound is to associate with air over water, and thus the more volatile the compound.
1170
1171

Supplemental Figure S44. Q mode NMDS results colored by the probability of linear biodegradation of each PAH species. Only variables (PAHs) are displayed. Smaller PAHs that load more positively on NMDS1 have higher probabilities of degradation (cool colors), whereas more recalcitrant PAHs load negatively on NMDS1, and are typically larger compounds (warm colors). NMDS1 may act as a degradation gradient, where samples loading positively on NMDS1 are less biodegraded and samples loading negatively on NMDS1 are more biodegraded.

**Supplemental Figure S45**. Q mode NMDS results colored by the Pristane/n-C$_{17}$ (Pr/17) value of each sample. Only samples are displayed. The Pr/17 ratio is higher in more biodegraded samples and lower in less biodegraded samples, as isoprenoids (such as pristane) are less biodegradable than alkanes. Warm colors represent lower Pr/17 ratios, cool colors represent higher Pr/17 ratios. We do not observe any association between the Pr/17 biodegradation index and NMDS1. Thus, we conclude that transport, and not biodegradation of samples, is what controls sample distribution along NMDS1.
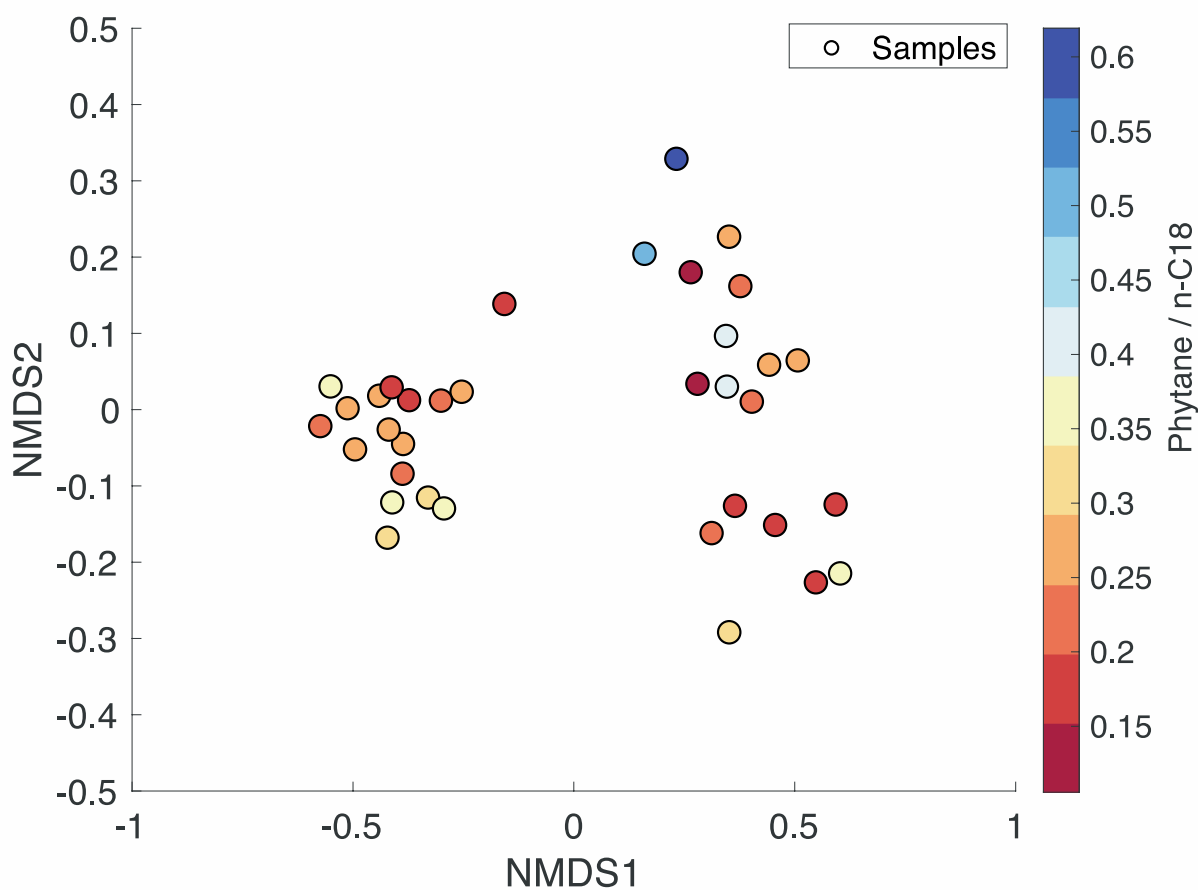
Supplemental Figure S46. Q mode NMDS results colored by the Phytane / n-C$_{18}$ (Ph/18) value of each sample. Only samples are displayed. The Ph/18 ratio is higher (cool colors) in more biodegraded samples and lower (warm colors) in less biodegraded samples, as isoprenoids (such as phytane) are less biodegradable than alkanes. We do not observe any association between the Ph/18 biodegradation index and NMDS1. Thus, we conclude that transport, and not biodegradation of samples, is what controls sample distribution along NMDS1.
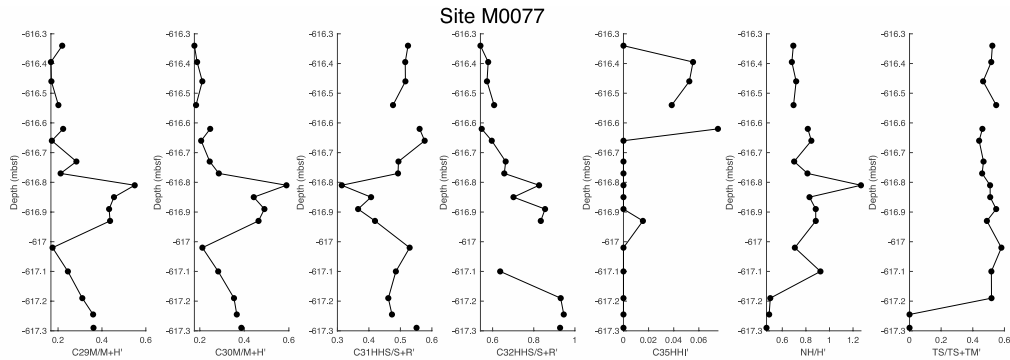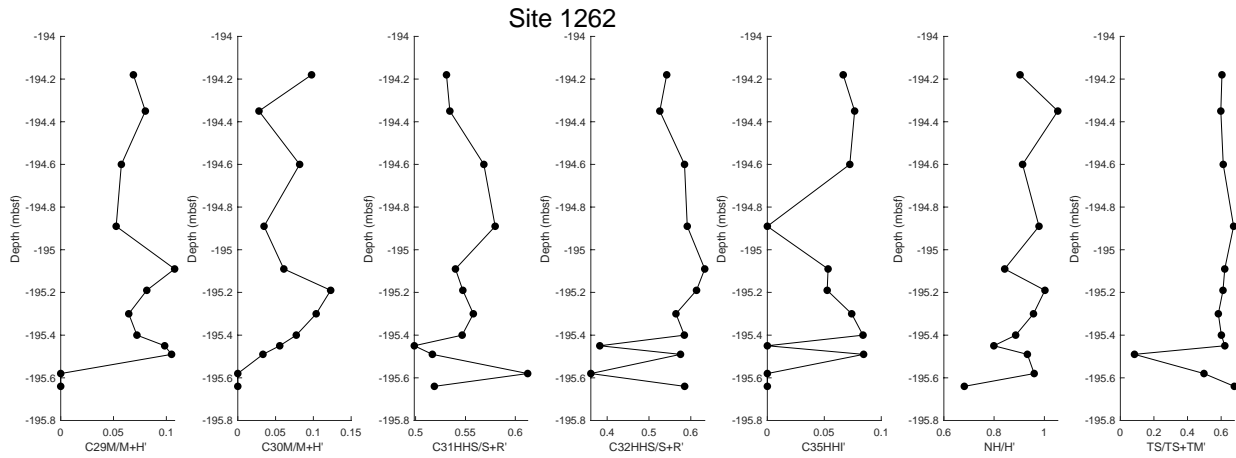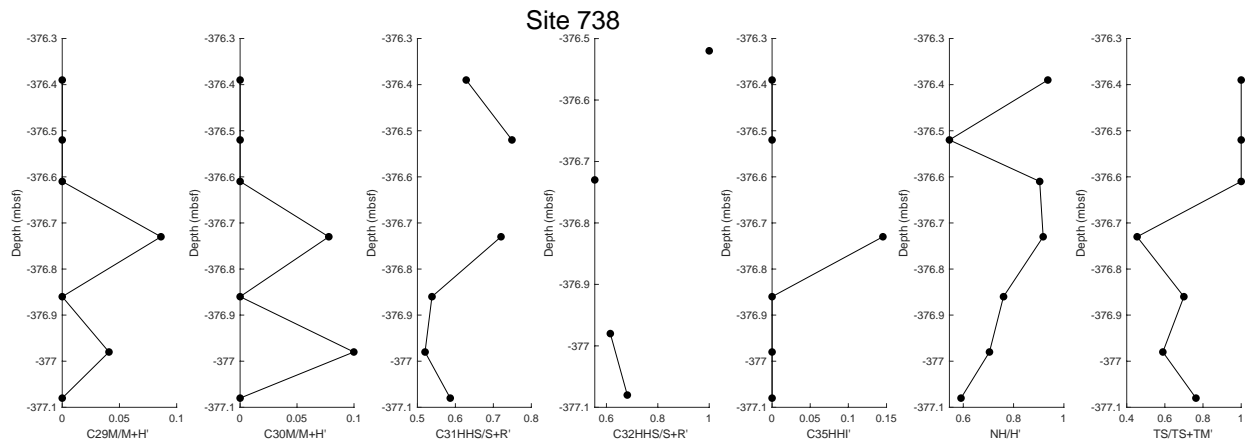
Site M0077

1204
1205 **Supplemental Figure S47**. Thermal maturity indices from Chicxulub Site M0077. C_{29} Moretane
1206 / Moretane + Hopane (C29M/M+H) and C_{30} Moretane / Moretane + Hopane (C30 M/M+H)
1207 decrease with increasing thermal maturity. C_{31} homohopane $S / S + R$ (C31HHS/S+R), C_{32}
1208 homohopane $S / S + R$ (C32HHS/S+R), C_{35} Homohopane Index (C35 HHI), Norhopane / Hopane
1209 (NH/H), and $T_s / T_s + T_m$ (TS/TS+TM) increase with increasing thermal maturity.
1210
1211

Site 1262

1212
1213 **Supplemental Figure S48.** Thermal maturity indices from Walvis Ridge Site 1262. C_{29}
1214 Moretane / Moretane + Hopane (C29M/M+H) and C_{30} Moretane / Moretane + Hopane (C30
1215 M/M+H) decrease with increasing thermal maturity. C_{31} homohopane $S / S + R$ (C31HHS/S+R),
1216 C_{32} homohopane $S / S + R$ (C32HHS/S+R), C_{35} Homohopane Index (C35 HHI), Norhopane /
1217 Hopane (NH/H), and $T_s / T_s + T_m$ (TS/TS+TM) increase with increasing thermal maturity.
1218

Supplemental Figure S49. Thermal maturity indices from Kerguelen Plateau Site 738. C_{29} Moretane / Moretane + Hopane (C29M/M+H) and C_{30} Moretane / Moretane + Hopane (C30 M/M+H) decrease with increasing thermal maturity. C_{31} homohopane $S / S + R$ (C31HHS/S+R), C_{32} homohopane $S / S + R$ (C32HHS/S+R), C_{35} Homohopane Index (C35 HHI), Norhopane / Hopane (NH/H), and $T_s / T_s + T_m$ (TS/TS+TM) increase with increasing thermal maturity.
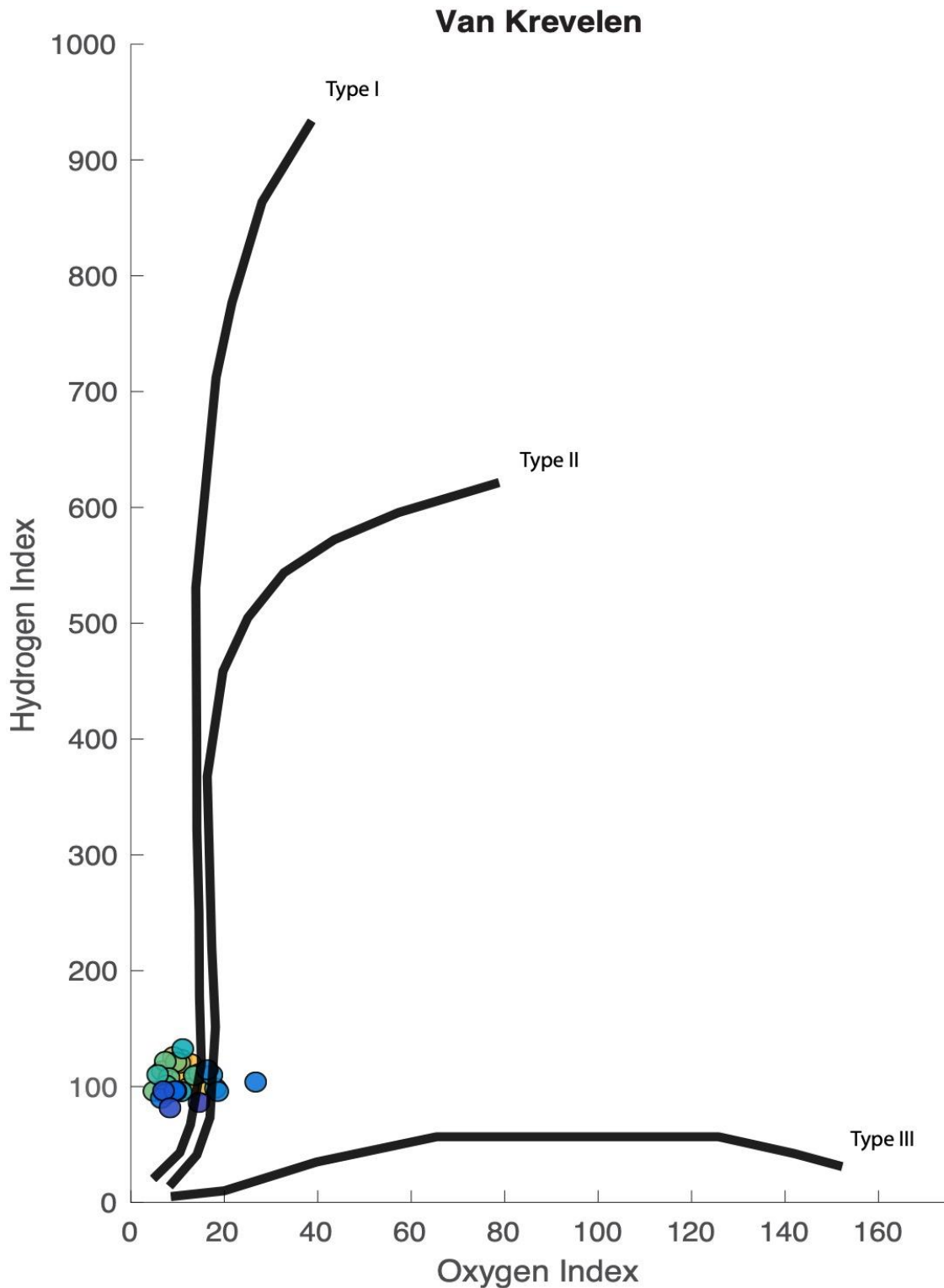
1226
Supplemental figure S50. Van Krevelen diagram of samples from Chicxulub Site M0077 with
contours of Type I, II, and III kerogen. The low Oxygen Index coupled with a low Hydrogen
Index may be a function of thermally altered (i.e. thermally matured) Type I/II kerogen.

1230
1231

Supplemental Dataset 1. Biomarker data from Sites M0077 (Chicxulub), 1262 (Walvis Ridge), and 738 (Kerguelen Plateau) collected in this study.

Supplemental Dataset 2. PAH integration data used for Q mode NMDS.

Supplemental Dataset 3. Q mode NMDS loadings of samples and variables (PAHs) based on PAH composition of samples from Sites M0077, 738, and 1262.

Supplemental Dataset 4. APDI calculations and values for samples from site M0077, 738, and 1262. APDI is calculated for the homologous series of phenanthrenes, pyrenes, and chrysenes. Values highlighted in yellow were deemed low quality and should not be interpreted.

Supplemental Dataset 5. Properties of PAHs measured within this study that were further analyzed alongside NDMS data.

References

1. S. Gulick, *et al.*, Expedition 364 Preliminary Report: Chicxulub: drilling the K-Pg impact crater. *Int. Ocean Discov. Progr.*, 38 (2017).

2. S. P. S. Gulick, *et al.*, The first day of the Cenozoic. *Proc. Natl. Acad. Sci.*, 201909479 (2019).

3. T. J. Bralower, *et al.*, Origin of a global micrite layer in the aftermath of the Cretaceous-Paleogene boundary impact. *Earth. Planet. Sci. Lett. In Press.*

4. S. Goderis, *et al.*, The final settling of meteoritic matter on the peak-ring of the Chicxulub impact structure in Core M0077A of IODP-ICDP Expedition 364 in *Large Meteorite Impacts and Planetary Evolution IV*, (2019), pp. 13–14.

5. C. M. Lowery, *et al.*, Rapid recovery of life at ground zero of the end- Cretaceous mass extinction The Cretaceous/Palaeogene mass extinction. *Nature* **558**, 288–291 (2018).

6. H. R. Thierstein, The Cretaceous/Tertiary boundary at Site 738, southern Kerguelen Plateau. *Proc., Sci. results, ODP, Leg 119, Kerguelen Plateau-Prydz Bay*, 849–867 (1991).

7. B. T. Huber, "Maestrichtian planktonic foraminifer biostratigraphy and the Cretaceous/Tertiary boundary at Hole 738C (Kerguelen Plateau, southern Indian Ocean)" in *Proc., Scientific Results, ODP, Leg 119, Kerguelen Plateau-Prydz Bay*, (1991), pp. 451–465.

8. J. J. Pospichal, B. T. Huber, The Cretaceous/Tertiary boundary in the southern Indian Ocean: results from the coring operations of the Ocean Drilling Program. *Am. Geophys. Union Geophys. Monogr. Ser.* **70**, 275–294 (1992).

9. H. R. Thierstein, *et al.*, The Cretaceous/Tertiary boundary at Site 738, southern Kerguelen Plateau. *Proc. Ocean Drill. Program, Sci. Results* **119**, 849–867 (1991).

10. B. T. Huber, Evidence for planktonic foraminifer reworking versus survivorship across the Cretaceous-Tertiary boundary at high latitudes. *Spec. Pap. Geol. Soc. Am.* **307**, 319–334 (1996).

11. J. C. Zachos, D. Kroon, P. Blum, "Site 1262" Proc. Ocean Drill. Program Initial. Rep. 208 (2004).

12. G. Ravizza, D. Vonderhaar, A geochemical clock in earliest Paleogene pelagic carbonates

1278   based on the impact-induced Os isotope excursion at the Cretaceous-Paleogene boundary.
1279   *Paleoceanography* **27**, 1–15 (2012).

1280 13.   T. J. Goldin, H. J. Melosh, Self-shielding of thermal radiation by Chicxulub impact ejecta:
1281   Firestorm or fizzle? *Geology* **37**, 1135–1138 (2009).

1282 14.   R. Tagle, *et al.*, Platinum group elements in impactites of the ICDP Chicxulub drill core
1283   Yaxcopoil-1: Are there traces of the projectile? *Meteorit. Planet. Sci.* **39**, 1009–1016
1284   (2004).

1285 15.   T. Kenkmann, A. Wittmann, D. Scherler, Structure and impact indicators of the
1286   Cretaceous sequence of the ICDP drill core Yaxcopoil-1, Chicxulub impact crater,
1287   Mexico. *Meteorit. Planet. Sci.* **39**, 1069–1088 (2004).

1288 16.   M. C. Harvey, S. C. Brassell, C. M. Belcher, A. Montanari, Combustion of fossil organic
1289   matter at the Cretaceous-Paleogene (K-P) boundary. *Geology* **36**, 355–358 (2008).

1290 17.   J. Morgan, N. Artemieva, T. Goldin, Revisiting wildfires at the K-Pg boundary. *J.*
1291   *Geophys. Res. Biogeosciences* **118**, 1508–1520 (2013).

1292 18.   C. M. Belcher, M. E. Collinson, A. C. Scott, Constraints on the thermal energy released
1293   from the Chicxulub impactor: new evidence from multi-method charcoal analysis. *J. Geol.*
1294   *Soc. London.* **162**, 591–602 (2005).

1295 19.   T. Arinobu, R. Ishiwatari, K. Kaiho, M. A. Lamolda, Spike of pyrosynthetic polycyclic
1296   aromatic hydrocarbons associated with an abrupt decrease in δ 13 C of a terrestrial
1297   biomarker at the Cretaceous-Tertiary boundary at Caravaca, Spain. *Geology* **27**, 723–726
1298   (1999).

1299 20.   M. I. Venkatesan, J. Dahl, Organic geochemical evidence for global fires at the
1300   cretaceous/tertiary boundary. *Nature* **338**, 57–60 (1989).

1301 21.   K. Kaiho, *et al.*, Global climate change driven by soot at the K-Pg boundary as the cause
1302   of the mass extinction. *Sci. Rep.* **6**, 1–13 (2016).

1303 22.   M. M. R. Mostert, G. A. Ayoko, S. Kokot, Application of chemometrics to analysis of soil
1304   pollutants. *Trends Anal. Chem.* **29**, 430–445 (2010).

1305 23.   T. D. Bucheli, F. Blum, A. Desaules, Ö. Gustafsson, Polycyclic aromatic hydrocarbons,
1306   black carbon, and molecular markers in soils of Switzerland. *Chemosphere* **56**, 1061–1076
1307   (2004).

1308 24.   A. I. Holman, K. Grice, C. M. B. Jaraula, A. Schimmelmann, Bitumen II from the
1309   Paleoproterozoic Here's Your Chance Pb/Zn/Ag deposit: Implications for the analysis of
1310   depositional environment and thermal maturity of hydrothermally-altered sediments.
1311   *Geochim. Cosmochim. Acta* **139**, 98–109 (2014).

1312 25.   K. H. Williford, K. Grice, G. A. Logan, J. Chen, D. Huston, The molecular and isotopic
1313   effects of hydrothermal alteration of organic matter in the Paleoproterozoic McArthur
1314   River Pb/Zn/Ag ore deposit. *Earth Planet. Sci. Lett.* **301**, 382–392 (2011).

1315 26.   B. R. T. Simoneit, P. F. Lonsdale, Hydrothermal petroleum in mineralized mounds at the
1316   seabed of Guaymas Basin. *Nature* **295**, 198–202 (1982).

1317 27.   I. Gilmour, W. S. Wolbach, E. Anders, "Major wildfires at the Cretaceous-Tertiary
1318   boundary" in *Catastrophes and Evolution: Astronomical Foundations*, S. V. M. Clube,
1319   Ed. (Cambridge University Press, 1990), pp. 195–213.

1320 28.   S. D. Killops, V. J. Killops, *Introduction to organic geochemistry* (John Wiley & Sons,
1321   Ltd, 2013).

1322 29.   S. Pal, J. P. Shrivastava, S. K. Mukhopadhyay, Polycyclic aromatic hydrocarbon
1323   compound excursions and K/Pg transition in the late Cretaceous-early Palaeogene

1324 succession of the Um Sohryngkew river section, Meghalaya. *Curr. Sci.* **109**, 1140–1150
1325 (2015).
1326 30. W. S. Wolbach, R. S. Lewis, E. Anders, Cretaceous extinctions: evidence for wildfires
1327 and search for meteoric material. *Science (80-.).* **230**, 167–170 (1985).
1328 31. W. S. Wolbach, I. Gilmour, E. Anders, C. J. Orth, R. R. Brooks, Global fire at the
1329 Cretaceous-Tertiary boundary. *Nature* **334**, 665–669 (1988).
1330 32. E. Stogiannidis, R. Laane, Source characterization of polycyclic aromatic hydrcarbons by
1331 using their molecular indices: An overview of possibilities. *Rev. Environ. Contam.*
1332 *Toxicol.* **234**, 49–133 (2015).
1333 33. D. Heymann, L. P. F. Chibante, R. R. Brooks, W. S. Wolbach, R. E. Smalley, Fullerenes
1334 in the Cretaceous-Tertiary boundary layer. *Science (80-.).* **265**, 645–647 (1994).
1335 34. V. V Shuvalov, N. A. Artemieva, Numerical modeling of Tunguska-like impacts. *Planet.*
1336 *Space Sci.* **50**, 181–192 (2002).
1337 35. T. Salge, H. Stosnach, G. Rosatelli, L. Hecht, W. U. Reimold, Evidence for shock-induced
1338 anhydrite recrystallization and decomposition at the UNAM-7 drill core from the
1339 Chicxulub impact structure. *Meteorit. Planet. Sci.* **2356**, 2334–2356 (2019).
1340 36. H. Mita, A. Shimoyama, Distribution of polycyclic aromatic hydrocarbons in the K/T
1341 boundary sediments at Kawaruppu, Hokkaido, Japan. *Geochem. J.* **33**, 305–315 (1999).
1342 37. M. A. Kruge, B. A. Stankiewicz, J. C. Crelling, A. Montanari, D. F. Bensley, Fossil
1343 charcoal in Cretaceous-Tertiary boundary strata: Evidence for catastrophic firestorm and
1344 megawave. *Geochim. Cosmochim. Acta* **58**, 1393–1397 (1994).
1345 38. C. M. Belcher, Reigniting the Cretaceous-Palaeogene firestorm debate. *Geology* **37**,
1346 1147–1148 (2009).
1347 39. K. Kaiho, *et al.*, Global climate change driven by soot at the K-Pg boundary as the cause
1348 of the mass extinction. *Sci. Rep.* **6**, 28427 (2016).
1349 40. D. Heymann, *et al.*, Geochemical markers of the Cretaceous-Tertiary boundary event at
1350 Brazos River, Texas, USA. *Geochim. Cosmochim. Acta* **62**, 173–181 (1998).
1351 41. W. S. Wolbach, "Carbon across the Cretaceous-Tertiary boundary." Dissertation.
1352 University of Chicago, Department of Chemistry (1990).
1353 42. W. S. Wolbach, I. Gilmour, E. Anders, "Major wildfires at the Cretaceous/Tertiary
1354 boundary" in *Global Catastrophes in Earth History; An Interdisciplinary Conference on*
1355 *Impacts, Volcanism, and Mass Mortality*, V. L. Sharpton, P. D. Ward, Eds. (Geological
1356 Society of America, 1990).
1357 43. J. P. Baltrus, A. W. Wells, D. J. Fauth, J. R. Diehl, C. M. White, Characterization of
1358 carbon concentrates from coal-combustion fly ash. *Energy and Fuels* **15**, 455–462 (2001).
1359 44. N. L. Rose, E. Change, B. Way, L. Uk, W. Oap, Fly-Ash Spheres As Pollution. **91** (1996).
1360 45. D. S. Robertson, W. M. Lewis, P. M. Sheehan, O. B. Toon, K-Pg extinction :
1361 Reevaluation of the heat- fi re hypothesis. **118**, 329–336 (2013).
1362 46. W. Seiler, P. J. Crutzen, Estimates of Gross and Net Fluxes of Carbon Between. *Clim.*
1363 *Change* **2**, 207–247 (1980).
1364 47. L. C. Ivany, R. J. Salawitch, Carbon isotopic evidence for biomass burning at the K-T
1365 boundary. *Geology* **21**, 487–490 (1993).
1366 48. M. A. Sephton, Organic compounds in carbonaceous meteorites. *Nat. Prod. Rep.* **19**, 292–
1367 311 (2002).
1368 49.   K. L. Pering, C. Ponnamperuma. Aromatic Hydrocarbons in the Murchison Meteorite
1369 *Science* **173**, 237–239 (2014).

1370 50. Z. Wang, *et al.*, Quantitative Characterization of PAHs in Burn Residue and Soot Samples
1371 and Differentiation of Pyrogenic PAHs from Petrogenic PAHs - The 1994 Mobile Burn
1372 Study. *Environ. Sci. Technol.* **33**, 3100–3109 (1999).
1373 51. A. T. Karp, A. I. Holman, P. Hopper, K. Grice, K. H. Freeman, Fire Distinguishers:
1374 Refined interpretations of paleofire from polycyclic aromatic hydrocarbons. Geochim.
1375 Cosmochim. Acta. *In Press.*
1376 52. B. McCune, J. B. Grace, *Analysis of Ecological Communities* (2005)
1377 https:/doi.org/10.1016/S0022-0981(03)00091-1.
1378 53. K. E. Peters, C. C. Walters, J. M. Moldowan, *The Biomarker Guide vol. 1 and vol. 2*
1379 (Cambridge University Press, 2005).
1380 54. M. L. Fogel, L. A. Cifuentes, "Isotope Fractionation during Primary Production" in
1381 *Organic Geochemistry*, M. H. Engel, S. A. Macko, Eds. (Plenum Press, 1993), pp. 73–98.
1382 55. A. S. Mackenzie, R. L. Patience, J. R. Maxwell, Molecular parameters of maturation in
1383 the Toarcian shales , Paris Basin , France-I . Changes in the configurations of acyclic
1384 isoprenoid alkanes , steranes and triterpanes. *Geochim. Cosmochim. Acta* **44**, 1709–1721
1385 (1980).
1386 56. A. C. Rocha, C. Palma, Source identification of polycyclic aromatic hydrocarbons in soil
1387 sediments: Application of different methods. *Sci. Total Environ.* **652**, 1077–1089 (2019).
1388